

**Czech Technical University in Prague**  
**Faculty of Nuclear Sciences and Physical Engineering**



DOCTORAL THESIS

**Characterisation of Martensitic Phases in Ni-Mn-Ga-**  
**based Heusler Alloys**

Prague 2022

Petr Veřtát



# Bibliografický záznam

Autor	Ing. Petr Veřtát České vysoké učení technické v Praze Fakulta jaderná a fyzikálně inženýrská Katedra inženýrství pevných látek
Název práce	Characterisation of Martensitic Phases in Ni-Mn-Ga-based Heusler Alloys (Charakterizace martensitických fází v Heuslerových slitinách na bázi Ni-Mn-Ga)
Studijní program	D4CS – Aplikace přírodních věd
Studijní obor	3901V012 – Fyzikální inženýrství
Školitel	Mgr. et Ing. Oleg Heczko, Dr. FZÚ – Fyzikální ústav AV ČR, v. v. i. Oddělení magnetických měření a materiálů
Školitel specialista	Ing. Jan Drahokoupil, Ph.D. České vysoké učení technické v Praze Fakulta jaderná a fyzikálně inženýrská Katedra inženýrství pevných látek
Akademický rok	2022/2023
Počet stran	106
Klíčová slova	Magnetická tvarová paměť, Ni-Mn-Ga, martensit, rentgenová difrakce, neutronová difrakce, mikrostruktura martensitu, zdvojitelná mikrostruktura.



## Bibliographic Entry

Author	Ing. Petr Veřtát Czech Technical University in Prague Faculty of Nuclear Sciences and Physical Engineering Department of Solid State Engineering
Title of Dissertation	Characterisation of Martensitic Phases in Ni-Mn-Ga-based Heusler Alloys
Degree Programme	D4CS – Applications of Natural Sciences
Field of Study	3901V012 – Physical Engineering
Supervisor	Mgr. et Ing. Oleg Heczko, Dr. FZU – Institute of Physics of the Czech Academy of Sciences Department of Magnetic Measurements and Materials
Supervisor specialist	Ing. Jan Drahokoupil, Ph.D. Czech Technical University in Prague Faculty of Nuclear Sciences and Physical Engineering Department of Solid State Engineering
Academic Year	2022/2023
Number of Pages	106
Keywords	Magnetic shape memory, Ni-Mn-Ga, Martensite, X-ray diffraction, Neutron diffraction, Martensite microstructure, Twinned microstructure.



# Abstrakt

Předložená práce se zabývá studiem nízkosymetrických fází (martensitů) Heuslerových slitin na bázi Ni-Mn-Ga, zejména pomocí metod rentgenové a neutronové difraktometrie. Důraz je kladen na základní výzkum v několika klíčových a dosud nevysvětlených tématech oboru. Kromě toho se zaměřuje na standardizaci několika pokročilých difrakčních metod vhodných pro charakterizaci zdvojitěné martensitické struktury a mikrostruktury.

V první části práce objasňuje teoretické základy – vysvětluje jev magnetické tvarové paměti v kontextu struktury a mikrostruktury martensitických fází. Dále se již zabývá možnostmi charakterizace rozličných forem vzorků těchto slitin zejména pomocí konvenčně dostupných rentgenových difraktometrů a pomocí neutronové difrakce. Charakterizace je značně ztížena všudypřítomnou hierarchicky zdvojitěnou mikrostrukturou a rovněž modulovaným charakterem některých zkoumaných fází. Ve výsledkové části jsou shrnuty dosažené vědecké výsledky úspěšně charakterizovaných nových materiálů ve formě monokrystalů, oligokrystalů a polykrystalů. Dále jsou popsány vědecké výstupy týkající se nemodulovaného a 14M modulovaného martensitu. Poté jsou již adresována dvě stěžejní témata práce: vazba mezi mikrostrukturním nanodvojitěním a difrakčním obrazem a fundamentální otázka souměřitelné či nesouměřitelné modulace 10M martensitu a její možné vazby na velmi specifické a unikátní vlastnosti našich materiálů.

---

# Abstract

Presented doctoral dissertation deals with the studies of the low-symmetry phases (martensites) of Ni-Mn-Ga-based Heusler alloys, especially by the means of the X-ray and neutron diffraction. Focus is given on the fundamental research in several pivotal topics of the field. Besides, the emphasis is put on the standardisation of several advanced diffraction methods suitable for the characterisation of twinned martensite structure and microstructure.


The first part summarises theoretical background, focusing on the magnetic shape memory effect in the context of the martensite structure and microstructure. It also addresses possibilities of characterisation of samples of the Ni-Mn-Ga-based alloys employing the conventional multipurpose X-ray diffractometers and neutron diffractometers. The characterisation is complicated by the inevitable hierarchically twinned microstructure and by the modulated character of the particular martensite phases. The results chapter summarises the achieved scientific results of the successful characterisation of new materials in form of single crystals, oligocrystals and polycrystals. Further it describes the results concerning the non-modulated and 14M modulated martensites. Finally, it addresses the most pivotal topics of thesis: the link between the nanotwinned microstructure and the diffraction pattern and the fundamental question of commensurate vs. incommensurate modulation of the 10M martensite and its possible connection with the specific and unique properties of our materials.





## Acknowledgements

I would like to express my deepest gratitude to my supervisor Dr. Oleg Heczko for his valuable guidance and feedback through my whole scientific carrier. Additionally, my journey would not be undertaken without Dr. Jan Drahokoupil, who introduced me to the world of diffraction analysis and always provided me with valuable comments and recommendations. Furthermore, my work would not have been possible without the help of many colleagues from the *FZU*, *FJFI*, *IT CAS*, *CUNI* and *LUT*.

From the depth of my heart, I thank Eliška Volfová for her love and emotional support. Finally, I would be remiss not to mention my family, especially my parents. Their belief in me has kept my spirits high during my studies. I would also like to thank *I.V.*  for all the entertainment and support.

This work was supported by the Grant Agency of the Czech Technical University in Prague, grant No. SGS22/183/OHK4/3T/14.



# Table of contents

Table of contents .....	6
List of abbreviations .....	8
Introduction .....	9
Goals .....	10
1 Martensites of Ni-Mn-Ga magnetic shape memory Heusler alloy .....	11
1.1 Heusler alloys .....	11
1.2 Martensitic transformation as the origin of martensite in Heusler alloys .....	14
1.3 Martensite variants and twinned microstructure .....	17
1.4 Magnetically induced reorientation of martensite (MIR) .....	20
1.5 Martensite phases of Ni-Mn-Ga and the current state of art .....	22
1.6 Suitable diffraction methods for the characterisation of the martensites of Ni-Mn-Ga-based alloys .....	27
1.7 Fundamental question of Ni-Mn-Ga polycrystals .....	29
2 Experimental .....	30
2.1 Materials .....	30
2.2 Diffraction studies .....	31
2.3 Complementary experimental techniques .....	38
3 Methodology of diffraction characterisation of martensites of Ni-Mn-Ga-based single-, poly- and oligocrystalline samples .....	39
3.1 Single-crystal Laue diffraction and sample orientation .....	39
3.2 XRD characterisation of Ni-Mn-Ga-based single crystals employing the multipurpose X-ray diffractometer .....	42
3.3. ND studies of the modulation and processing of q-scans .....	50
3.4 XRD characterisation of the Ni-Mn-Ga bulk polycrystals and powders .....	53
3.5 XRD characterisation of Ni-Mn-Ga oligocrystals and heavily textured polycrystals .....	55
4 Results and discussion .....	62
4.1 Characterisation of the newly casted Ni-Mn-Ga-based single-, poly- and oligocrystalline samples .....	62
4.2 Evaluation of the crystal quality of Ni-Mn-Ga single crystals .....	69
4.3 Characterisation of the NM martensite – the extrapolation of zero-Kelvin lattice parameters for ab-initio study .....	70
4.4 Characterisation of the 14M modulated martensite .....	72
4.5 Analysis of nanotwinned form of 10M martensite .....	75
4.6 Studies of the structural modulation within the 10M modulated martensite of Ni-Mn-Ga(-Fe) single crystals .....	79
5 Conclusions and outlook .....	88
Appendix I: General introduction into structural modulation .....	90
Appendix II: Complete list of analysed samples .....	92
References .....	96
List of author's works relating to the doctoral thesis .....	104
List of other author's works .....	105

## List of abbreviations

10M	Five-layered monoclinic/modulated (martensite)
14M	Seven-layered monoclinic/modulated (martensite)
A	Austenite
CW	Constant wavelength
FZU	FZU – Institute of Physics of the Czech Academy of Sciences
MFIS	Magnetic field induced strain
MIR	Magnetically induced reorientation (of martensite)
MSM	Magnetic shape memory
ND	Neutron diffraction
NM	Non-modulated (martensite)
PND	Powder Neutron diffraction
PXRD	Powder X-ray diffraction
RSM	Reciprocal space map/mapping
RT	Room temperature
RUS	Resonant ultrasound spectroscopy
SEM	Scanning electron microscopy
SMA	Shape memory alloys
SXRD	Synchrotron X-ray diffraction
$T_{10M-A}$	Temperature of the 10M→A transition
$T_C$	Currie temperature
TEM	Transmission electron microscopy
XRD	X-ray diffraction

# Introduction

The discovery of giant magnetically induced strain, also called magnetic shape memory (MSM) effect, in Ni<sub>2</sub>MnGa Heusler alloy by Kari Ullakko [1] stimulated a tremendous scientific interest in the Ni-Mn-Ga-based materials, due to their applications as sensors [2], actuators [3,4], micropumps [5] and energy-conversion devices [6].

The essential precursor of the effect is the martensitic transformation from cubic austenite to low-symmetry phase called martensite. This diffusionless thermoelastic solid-to-solid phase transition leads to creation of various martensite phases with specific structural, mechanical, magnetic and transport properties. Resulting phases are rich in complex structures and microstructures – combining the structural modulation and hierarchical twinning. The modulation and twinning can be responsible for the main fundamental effect: the magnetic-field induced reorientation (MIR) of twinned martensite variants allowing the aforementioned applications.

Even though the Ni-Mn-Ga-based alloys were already studied for the long time, some of the basics are still an open question that brings the necessity of advanced fundamental analysis. Among is the still unresolved topic of the nature of the five-layer modulated martensite or its connection to the extremely high twin boundary mobility as an essential precursor for MIR.

Apart from the fundamental questions, the current development of the new Ni-Mn-Ga-based Heusler compounds is aiming to possibly their unique properties and/or bring these to the desired temperature region. The research is pointed towards alloying of the Ni-Mn-Ga by Cu-, Co-, Fe- and other metals. The new alloys of different stoichiometries bring the obvious necessity of their characterisation. Relatively easily preparable bulk polycrystals produced, e.g., by arc-melting often result in the complicated highly textured polycrystalline or oligocrystalline nature of the samples that requires advanced characterisation methods.

In my thesis, I present the outcome of my work in the FZU – Institute of Physics of the Czech Academy of Sciences, where I have been responsible for the characterisation of the various Ni-Mn-Ga-based alloys. Here I will focus mainly on the structural studies of modulated and twinned martensites as this represents the very base of the understanding the material. During my doctoral studies, I have gained extensive experience with the diffraction analysis of Ni-Mn-Ga-based alloys that employed mainly the conventional multipurpose in-lab X-ray diffractometers. Therefore, after the necessary introduction into the world of the magnetic shape memory alloys, I will try to describe my to-date accumulated knowledge of the XRD characterisation of these materials. Not only will I list the tasks that became my everyday routine in studies of the newly created samples of various forms, but I will also try to contribute to the fundamental research – especially the ongoing discussion regarding the modulation of the five-layered modulated martensite, the most promising one from the application point of view.

This thesis is structured as follows:

The first chapter introduces the class of Heusler alloys with their specific structure. This quickly takes us to the Ni-Mn-Ga system and its martensite phases. I describe their specifics, including the omnipresent twinning on various scales and structural modulation, together with the notes on the current state of art. The complicated structure and microstructure of our martensites brings the need of suitable diffraction methods described in the end of the chapter.

In the second chapter, typical forms of our samples are described together with the experimental equipment used for our analyses. Focus is given on the diffraction methods, data processing and advantages of the beam divergence in our case.

The third chapter deals with the used methodology of our diffraction characterisation of the martensites of Ni-Mn-Ga-based alloys. I describe developed specific procedures suitable to obtain fundamental results hoping that this will serve as a transparent compilation of the proven methods.

The fourth chapter describes obtained results in several directions of the field. At the beginning, I present the results of the characterisation of complicated forms of newly created samples Ni<sub>2</sub>MnGa-based alloys alloyed by Cu, Cr and Fe. Then, the different quality of the crystals from various producers is shortly addressed. This is followed by the summary of the results of the characterisation of 14M and NM martensites. Finally, some of the most pivotal topics of thesis will be addressed. This begins with the link between the diffraction pattern and the nanotwinned martensite microstructure. Finally, our answers to the fundamental question of commensurate vs. incommensurate modulation of the five-layered modulated martensite and its possible connection with the specific and unique properties of our materials is given at the end.

Final chapter summarises our conclusions, their importance for the field and shortly discusses the outlook and experiments planned in the near future.

## Goals

The main goals of the dissertation can be summarised in the following points:

- To characterise the newly created samples of Ni-Mn-Ga-based alloys using the diffraction methods and, moreover, to establish the procedures that employ the multipurpose X-ray diffractometer in our field of study. The goal is to provide brief practical guidelines for successful martensite phase identification and basic characterisation.
- To employ these procedures and methods in the studies of the twinned Ni-Mn-Ga-based single crystals and new Ni-Mn-Ga-based alloys that often result in complicated oligocrystalline sample nature.
- To focus on the most discussed fundamental topics of the field, particularly to the ongoing question of the nature of the structural modulation of the five-layered modulated martensite and the effect of twinning.

# 1 Martensites of Ni-Mn-Ga magnetic shape memory Heusler alloy

In this chapter, class of Heusler alloys is introduced together with their structure and some of the main applications. After that, we focus on Ni-Mn-Ga-based alloys and their specifics. We describe the martensitic transformation as the precursor for the (magnetic) shape memory effect and introduce the resulting martensite phases.

## 1.1 Heusler alloys

In 1901, Fr. Heusler (1866 – 1947) in his letter announced a new class of ferromagnetic alloys constituting entirely of non-ferromagnetic elements: Cu-Mn bronze alloyed with *sp* elements Sn, Al, As, Sb, Bi or B. [7] Two years later, he reported details on their synthesis and, together with W. Starck and E. Haupt, on their magnetic properties. [8] The discovery of Heusler alloys excited considerable interest resulting in the discovery of vast amount of new ferromagnetic alloys and compounds, many of which exhibit peculiar magnetic and structural effects. [9]

### 1.1.1 The structure of Heusler alloys

Nowadays, we define Heusler alloys as ternary intermetallic compounds (rather than alloys) at the stoichiometric composition  $X_2YZ$ , where  $X$  and  $Y$  are usually transition metals and  $Z$  is a main group element. In some cases,  $Y$  is replaced by a rare-earth element or an alkaline earth metal.

The structure of Heusler alloys can be described in terms of four interpenetrating f.c.c. sublattices A, B, C and D (Fig. 1). Here, the A and C sites are occupied by  $X$  atoms, the B sites by  $Y$  atoms and the D sites by  $Z$  atoms. This corresponds to the Strukturbericht type  $L2_1$  and the cubic space group  $Fm\bar{3}m$  (no. 225). [9]

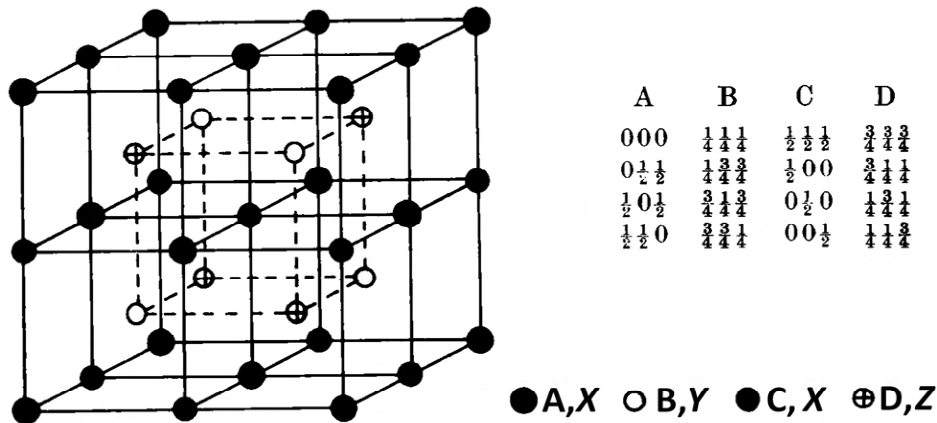


Fig. 1: Structure  $L2_1$  of the ternary  $X_2YZ$  Heusler alloy together with the coordinates of the sites. Adapted from [9]

Furthermore, there is also a group of  $XYZ$  ternary compounds known as “half-Heusler” or “semi-Heusler”, where one of the four f.c.c. sublattices of the “full-Heusler” alloy remains unoccupied. This leads to non-centrosymmetric cubic structure, space group  $F\bar{4}3m$  (no. 216), Strukturbericht type  $C1_b$ . [10]

Even though the Heusler alloys are in fact chemical compounds and as such exhibit the chemical order characteristics of compounds, they retain the metallic lustre and high conductivity of metals. Their magnetic properties are similarly intermediate: while the majority of Heusler alloys is

ferromagnetic, there also exists the large group of antiferromagnetic Heusler alloys. [9] Some claim, that properties of many Heusler materials can be predicted by the valence electron count [11] or first principles calculations. [12–14] This allows tuning of their properties through varying the compositions and alloying. However, many exceptions can be found, emphasizing the needs for extensive experimental research.

### 1.1.2 Disorder in Heusler alloys and the diffraction studies

The partial interchange of atoms in different sublattices of the highly ordered L2<sub>1</sub> structure occurs in many full-Heusler alloys. The most prominent is the interchange of *Y* and *Z* atoms, leading to the L2<sub>1</sub>-B2 type disorder. The random distribution of *X* and *Y* or *X* and *Z* atoms leads to the D0<sub>3</sub> structure. The less frequent disorders include the B32a disorder (*X* atoms from one of the f.c.c. sublattices mixed with *Y* atoms, *X* of the second sublattice mixed with *Z* atoms) or the A2 disorder (where all the positions become equivalent). Disorders can highly influence the properties of Heusler materials – even a small amount of disorder cause distinct changes in the electronic structure and thus also the transport and magnetic properties. [11]

Order is best analysed by the diffraction methods. It can be derived, that for the highly ordered L2<sub>1</sub> structure, there are 3 distinct reflection types allowed [15,16]:

$$\begin{aligned}
 F_1 &= 2f_A + f_B + f_D & h, k, l \text{ all even, } h + k + l &= 4n \\
 F_2 &= 2f_A - f_B - f_D & h, k, l \text{ all even, } h + k + l &= 4n + 2 \\
 F_3 &= f_B - f_D & h, k, l \text{ all odd,} &
 \end{aligned}$$

where  $F_{1..3}$  are the structure factors and  $f_{A..D}$  are the atomic scattering factors corresponding to the sites from **Fig. 1**. [15] Scattering intensity is proportional to  $|F_i|^2$ . First type are the principal (also called fundamental) reflections unaffected by the state of chemical order. These are present in the X-ray diffraction patterns with high intensity: e.g., the strong reflections usually are: (400), (220), (440), (620), (422) etc. Reflections of other two types are the superlattice reflections, e.g., (200), (600), (420), (311) are weak. In our case of Ni<sub>2</sub>MnGa, X-ray atomic scattering factors of Ni, Mn and Ga elements are quite close to each other:  $f_A = f_{Ni} \sim 28$ ,  $f_B = f_{Mn} \sim 25$ ,  $f_D = f_{Ga} \sim 31$  for zero scattering vector. In the fully ordered state, this should make  $F_2 \sim 0$ , since  $f_{Mn} + f_{Ga} \approx 56 \approx 2f_{Ni}$ .

For illustration, the B2 order (CsCl structure, B and D positions are equivalent, **Fig. 2(a)**) gives two types of allowed reflections:

$$\begin{aligned}
 F_{\text{fundamental}} &= f_A + f_B & h + k + l &= \text{even} \\
 F_{\text{superlattice}} &= f_A - f_B & h + k + l &= \text{odd.}
 \end{aligned}$$

The A2 structure (simple b.c.c. structure, all the positions are equivalent, **Fig. 2(b)**) only allows one type of reflections:

$$F = 2f_A \quad h + k + l = \text{even.}$$



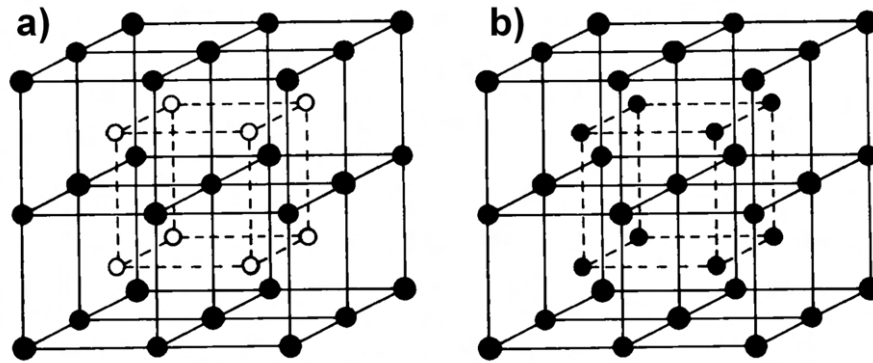


**Fig. 2:** Illustration of B2 order (a) and A2 order (b). Adapted from [9]

### 1.1.3 Magnetism of Heusler alloys

The  $X_2YZ$  Heusler alloy contains two magnetic sublattices – one containing  $Y$  atoms in octahedral coordination and one containing  $X$  atoms in tetrahedral coordination, if the constituting atoms have the magnetic moment, **Fig. 3**. Due to the two different magnetic sublattices that can couple ferromagnetically or antiferromagnetically, Heusler alloys can show various kinds of magnetic phenomena. Ferromagnetism, ferrimagnetism and half-metallic ferromagnetism have been reported. [11] However, usually only the magnetic moments of the  $Y$  atoms are significant despite  $X$  being transitional metal.

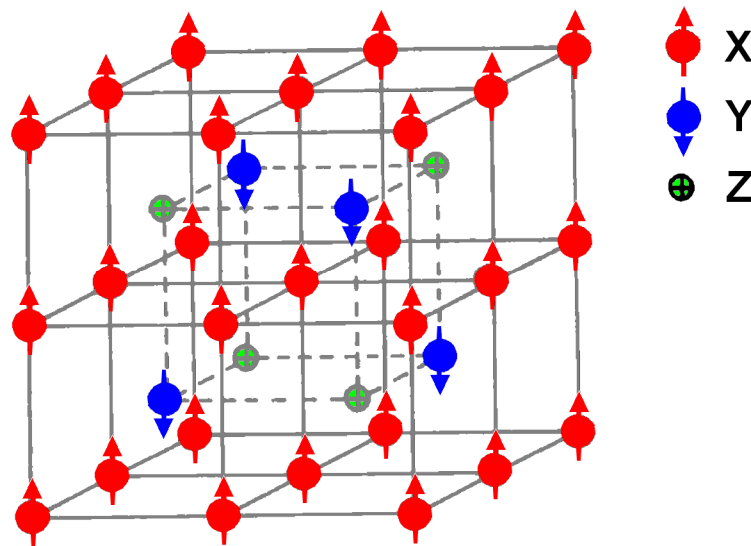


**Fig. 3:** Two magnetic sublattices of  $X_2YZ$  Heusler alloys showing the antiferromagnetic coupling. Adapted from [9].

On the contrary, the  $XYZ$  “half-Heusler” alloys can exhibit only one magnetic sublattice. They might be ferromagnetic only when  $X = \text{Mn}$  or rare-earth metal, but usually belong to the group of non-magnetic semiconducting materials with only a few ferromagnetic half-Heusler compounds described in literature. [11]

The Curie temperature of the Heusler alloys can noticeably vary from low, e.g., 105 K for  $\text{Co}_2\text{VSn}$  [17], to high ( $> 1100$  K) for  $\text{Co}_2\text{FeSi}$  [18]. [19]

### 1.1.4 Current main applications of Heusler alloys

There are more than 1000 different Heusler alloys that possess physical properties favourable for many applications. Later, we will focus purely on the group of Ni-Mn-Ga-based Heusler alloys where the main applications employ the magnetic shape memory (MSM) effect. Apart from those, probably the most important application of Heusler alloys is in the field of *spintronics*. [11] The family of full-Heusler alloys also includes a group (at least 28) of *superconducting materials*. Their critical temperature, however, is quite low; the highest reported value is 5.5 K. [20,21] Recently, applications of half-Heusler alloys in the fields of *topological insulators* [22] or *semiconductors* [23] are examined.

Comprehensive summary of possible applications of Heusler alloys is provided e.g. by Graf et al. [11] Following our motivation, in the remaining text, we will focus purely on the aforementioned *magnetic shape memory* phenomena which will be introduced from the very basics.

## 1.2 Martensitic transformation as the origin of martensite in Heusler alloys

The martensitic transformation (i.e., the transformation from the cubic austenite to martensite of lower symmetry) is one of the necessary precursors for the (magnetic) shape memory effect. It is the first-order displacive (but diffusionless) phase transition in the solid state. It can be induced by the changes in temperature [24], and, if there is a multiferroic coupling, it can be induced by the mechanical stress [25], magnetic field and electric field [26,27]. As in other first-order phase transitions, both phases, austenite and martensite, can coexist at an intermediate temperature or under stress due to the hysteresis.

The formation of martensite involves coordinated movement of atoms, albeit on small distances. Austenite and martensite lattices are intimately related, the martensitic transformations therefore lead to a reproducible orientation between them. One of the keys to understanding the transformation is the characterisation of these orientation relationships. [28,29] In 1924, Bain demonstrated the simple way to transform from f.c.c. austenite structure to b.c.t. martensite in steels. [30] The transformation is achieved by contracting the unit cell along one of its axes while expanding the cell along the other two. This deformation results in the following orientation relations of crystal planes and directions:

$$(010)_A \parallel (010)_M$$

$$[001]_A \parallel [101]_M$$

This Bain deformation involves the absolute minimum of atomic movements in generating the b.c.t. from the f.c.c. lattice. [24] The specific mechanism is in fact different from one alloy to another. In many materials, especially in complex steels, the orientation relations are more complicated. Overall, it is always possible to create a martensite from austenite by the combination of lattice elongation, contraction, shear along certain directions and lattice rotation. [31]

In many materials, the martensitic transformation is volume-conserving (or nearly volume-conserving). This secures better compatibility of austenite and martensite, very favourable in the applications of shape memory alloys (SMA) and magnetic shape memory (MSM) alloys.

During the transformation, the habit plane (the plane common to both austenite and martensite) macroscopically appears to be undistorted and not rotated. This is possible only due to an additional distortions – the dislocation slip (especially in steels) or twinning in martensite (usually in shape memory Heusler alloys), reducing the strain of the surrounding austenite, **Fig. 4**. [24] Only in case of the twinning, the martensitic transformation can be thermoelastic (thermally reversible), creating the crucial prerequisite for existence of the (magnetic) shape memory effect in general.

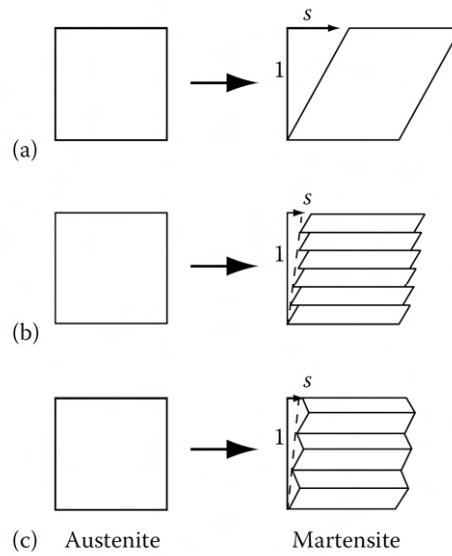


**Fig. 4:** Mechanisms of strain reduction on the austenite-martensite boundary.  $s$  denotes the transformation shear. (a) Shape change upon pure lattice deformation (e.g. Bain deformation). (b) Dislocation slip. (c) Martensite twinning. [24]

The nucleation of martensite is heterogeneous, i.e. the nucleation starts at the lattice defects of austenite, sample edges or other sharp discontinuities, and is followed by the continuous movement of the phase interface. [24] This interface, especially in the gradual stage, can move very fast, with velocities approaching the speed of sound. [11] Because of this, it might be difficult to study the martensitic transformation experimentally *in situ*.

Usual precursor phenomenon of the martensitic transformation is the structural softening of the b.c.c. lattice which, in case of magnetic alloy, can be enhanced by the softening due to magneto-elastic coupling. [32]

In some materials, especially in  $\text{Ni}_2\text{MnGa}$ , in a narrow range of compositions, the martensitic transformation is preceded by a transition to the premartensite phase. This can usually be detected by the diffraction or elastic constants softening. [24,33]

### 1.2.1 Insight into the martensitic transformation via the changes of physical properties

Later in the text, we will mainly focus on the structural studies. Apart from the observation of the structural changes indicated by the changes in the diffraction patterns, valuable insight can be obtained via measurements of various physical properties. Many of these can be examined continuously which brings the insight on the transformation kinetics.

The martensitic transformation (and later discussed intermartensitic transformations), being the first-order phase transition, causes the release or absorption of the latent heat that can be detected using the DSC, **Fig. 5**. The martensitic transformation is usually sharp and measurements clearly indicate thermal hysteresis with the hysteresis interval from several units to several tens of Kelvin, strongly depending on the chemical composition of specific alloys. For many applications, it is favourable to find compositions in which the martensitic transformation occurs around the room temperature.

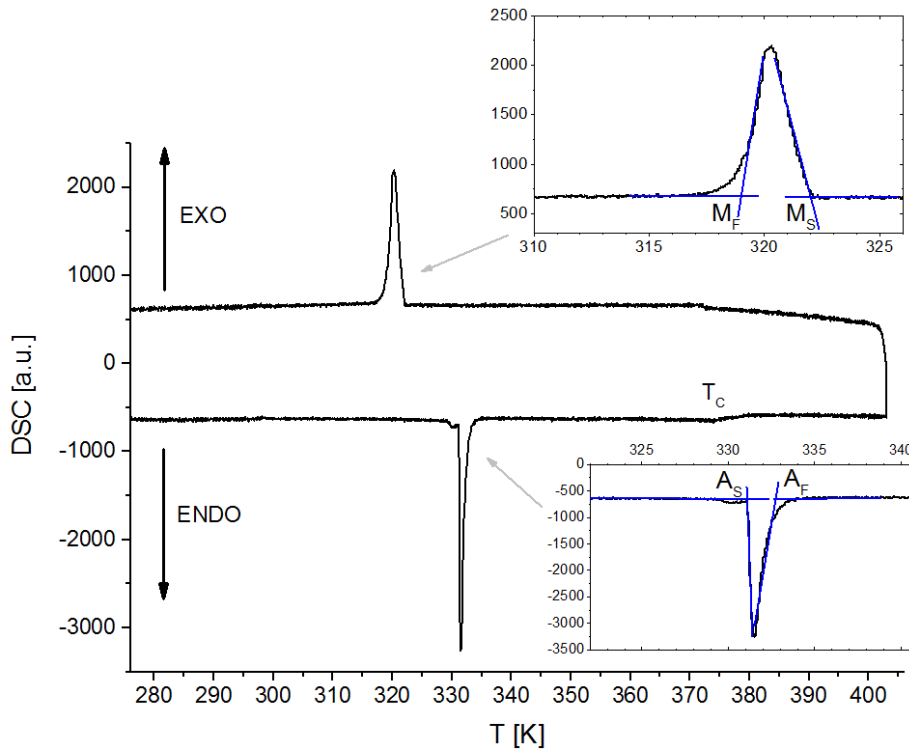


**Fig. 5:** Typical DSC curve for the martensitic transformation in Ni<sub>50</sub>Mn<sub>28.5</sub>Ga<sub>21.5</sub> MSM alloy. Schematically depicted are the characteristic temperatures of the transformation: martensite  $M_S$  start, martensite finish  $M_F$ , austenite start  $A_S$  and austenite finish  $A_F$ . Additionally, the Curie point  $T_C$  can also be seen as a minor change of slope in the heating and cooling curves.

Martensitic transformation leads to a jump change in electric resistivity, **Fig. 6**, due to the interaction of carriers with the twin microstructure and changes in electronic structure including Fermi surface nesting [34].

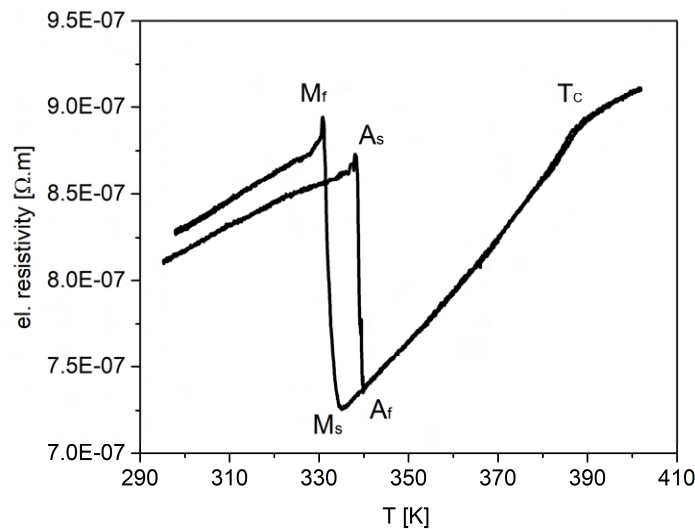


**Fig. 6:** Typical thermal dependence of electric resistivity of Ni-Mn-Ga single crystal. During the martensitic transformation, steep jump occurs due to the interaction of carriers with the martensite microstructure and changes in the electronic structure. Schematically depicted are the characteristic temperatures of the transformation: martensite  $M_S$  start, martensite finish  $M_F$ , austenite start  $A_S$  and austenite finish  $A_F$ . The Curie temperature  $T_C$  is also detectable due to changes in magnetic scattering.

Regarding magnetism, the AC magnetic susceptibility reveals a change in form of a jump or peak during the martensitic transformation caused by the change of magnetocrystalline anisotropy, **Fig. 7**. In the cubic austenite, the magnetocrystalline anisotropy is usually almost negligible in the contrary to the strong anisotropy in martensite, which results in a weaker magnetic response in martensite.

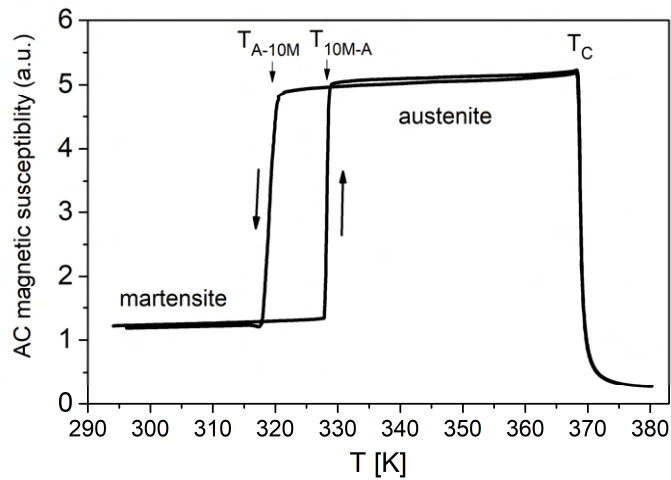


**Fig. 7:** Thermal dependence of the AC magnetic susceptibility of the  $\text{Ni}_{50}\text{Mn}_{28.5}\text{Ga}_{21.5}$  single crystal. Steep change caused by change of the large uniaxial magnetocrystalline anisotropy of martensite to almost negligible anisotropy of cubic austenite.

Experimental investigations of the evolution of the elastic coefficients of individual phases with changing temperature and/or magnetic field can bring other important data concerning the martensitic transformation.[12,35] When approaching the temperature of martensitic transformation from above, the austenite usually exhibits an increasing shear instability. The structural softening can also be strongly affected by magneto-elastic coupling. [32,33]

### 1.3 Martensite variants and twinned microstructure

The compensation of the transformation strains in martensite by twinning leads to the formation of differently oriented crystallographic domains, so called martensite twin variants. The complex martensite microstructure is therefore a result of energy minimisation and kinematic compatibility. [36]

The simplest case of deformation from cubic austenite to tetragonal martensite results in formation of three martensitic twin variants with different  $c$ -axis orientation (schematically in 2D shown in **Fig. 8**). These can then form a complex  $a/c$ -twinned (schematically demonstrated in **Fig. 9**).

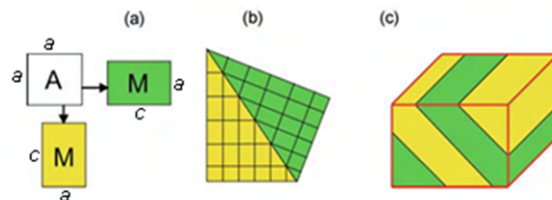


**Fig. 8:** 2D schematic depiction of the martensitic transformation from cubic austenite to tetragonal martensite. (a) Distortion of austenite (A) cell creates two different tetragonal twin martensite (M) variants. (b) These form a twinned microstructure connected by the twin boundary. (c) 3D sample containing two martensite variants. In 3D, usually all three variants of tetragonal martensite are formed and the twin microstructure is more complex. [37]

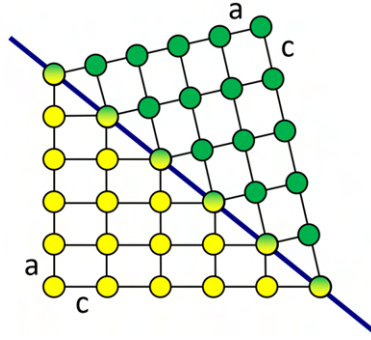


**Fig. 9:** Schematic depiction of the  $a/c$  twinning as a base for the twinned microstructure, adapted from [37].

For the martensites of lower symmetry, the amount of different martensite variants increases. From the group theory (following Hane [36]) the number of variants of martensite  $\mu$  can be calculated as follows: Let  $P^A$  be the point group of austenite and  $P^M$  the point group of martensite. Following the definition of martensitic transformation, one can immediately see that  $P^M \subset P^A$ . The number of martensite variants then is

$$\mu = \frac{\text{number of elements in } P^A}{\text{number of elements in } P^M}. \quad (1)$$

For tetragonal martensite we therefore obtain 3 aforementioned martensite variants (48 elements in point group  $m\bar{3}m$  of the cubic austenite divided by 16 elements in point group  $4/mmm$  of tetragonal martensite). Using similar calculations, we obtain 6 variants for orthorhombic martensite, 12 for monoclinic and 24 for triclinic martensite. When the modulation is employed, situation might become more complicated (see further).

Generally, in Ni-Mn-Ga-based alloys, complex twinned microstructure consists of up to five types of twins (depending on the martensite phase):

- **Type I twins** between variants with different orientations of the  $c$ -axis with rational twinning plane oriented along the  $\{101\}$  plane and irrational shear direction. [38–40]
- **Type II twins** between variants with different orientation of  $c$ -axis with irrational twinning plane (inclined several degrees from the  $\{101\}$  lattice plane. [38–40]
- **Modulation twins** – i.e.  $\{100\}$  compound twins, **Fig. 10 a)** [39,41]
- **“ $a/b$  twins”** – i.e.  $\{110\}$  compound twins, **Fig. 10 b)** [39,42,43]
- **Non-conventional twins** with a general orientation of the twin plane, **Fig. 10 c).** [39,44]

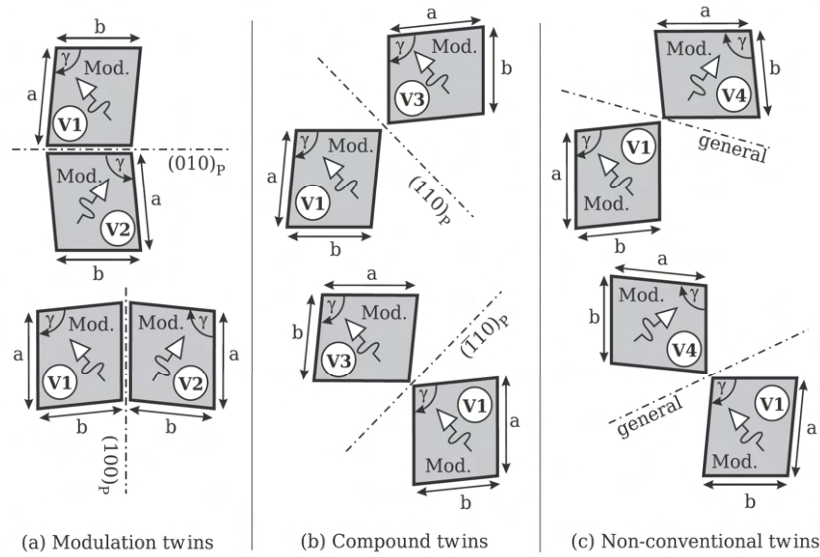


**Fig. 10:** Visualisation of the three in-plane twinning systems. The dash-dot lines outline the twinning planes. The view is perpendicular to the  $c$ -axis direction in all the variants. Modulation direction is marked by empty-head arrows. [39]

Continuum-based microstructural model for the most studied 10M martensite is provided by Seiner et al. in [45]. There they illustrated the possible hierarchy of the twin systems, **Fig. 11**.

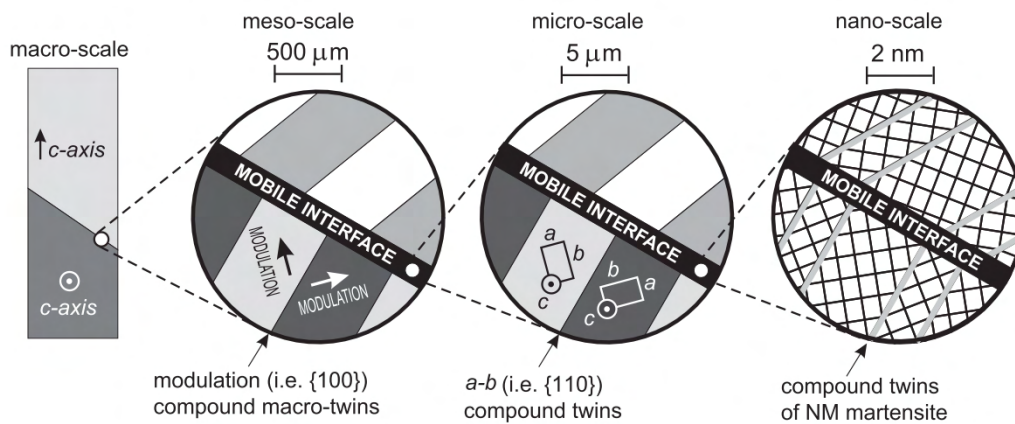


**Fig. 11:** Possible hierarchy of laminations in the vicinity of the mobile interface suggested by Seiner et al. [45]

Some cases of  $a/b$  twins are very close to the *merohedral twins*. Here, the twinned variants form a microstructure that overall appears (at least by some means of investigation) to be more symmetric than the originating components are. This can be demonstrated on two hypothetical martensite variants: the original one + the same one rotated  $90^\circ$ , and the resulting diffraction pattern from the twinned microstructure consisting of both, **Fig. 12**. Therefore, especially when it comes to diffraction studies, careful analysis needs to be employed to avoid possible misinterpretation caused by twinning.

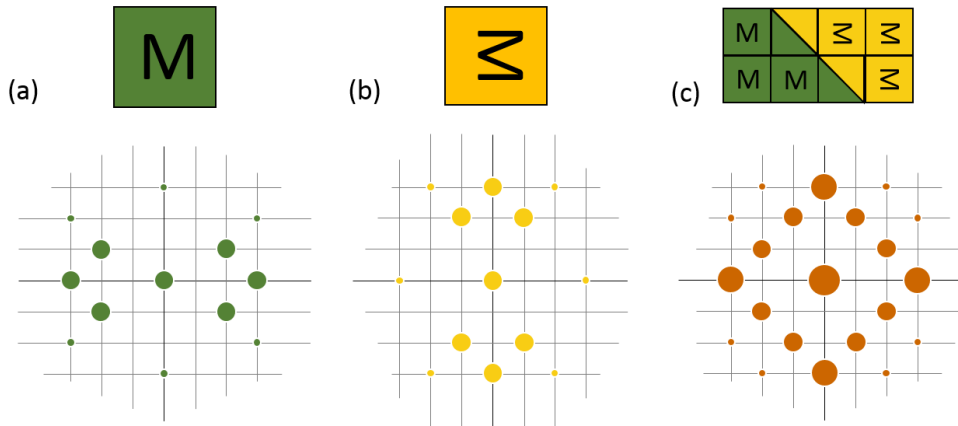


**Fig. 12:** Schematic depiction of an apparently higher symmetry suggested by the diffraction pattern. (a) Originating martensite variant and the corresponding hypothetical diffraction pattern. (b) Second martensite variant (= the originating one rotated by 90°) and the corresponding diffraction pattern. (c) In case of twinned microstructure consisting of both martensite variants, the corresponding diffraction pattern represents the superposition of both original patterns indicating a higher symmetry than the real one.

#### 1.4 Magnetically induced reorientation of martensite (MIR)

Spontaneously created martensite microstructure after the martensitic transformation can be reoriented in the magnetic field via the motion of the Type I and Type II twin boundaries. In the magnetic field, variants with easy magnetization axis along the field direction are energetically favoured and “grow” by the motion of twin boundaries at the expense of unfavourably oriented variants. [39] This magnetic field induced reorientation (MIR, schematically depicted in **Fig. 13** and **Fig. 14**) of martensite represents the main application potential of the Ni-Mn-Ga-based alloys. Analogous reorientation can be achieved by mechanical stress or strain, similarly as in shape memory alloys such as Ni-Ti [31].

For the martensite variant reorientation, high twin boundary mobility is essential. It has been shown that Type I twins require at least 0.2 T switching field or 1 MPa stress to move, while Type II twins can move through the crystal under a very low magnetic field of ~ 0.01 T or at much smaller stress levels of ~ 0.1 MPa, **Fig. 15**. [38–40,46] Both Type I and type II boundary motions result in the same martensite variants reorientation. They can exist in a sample simultaneously or can be formed independently.

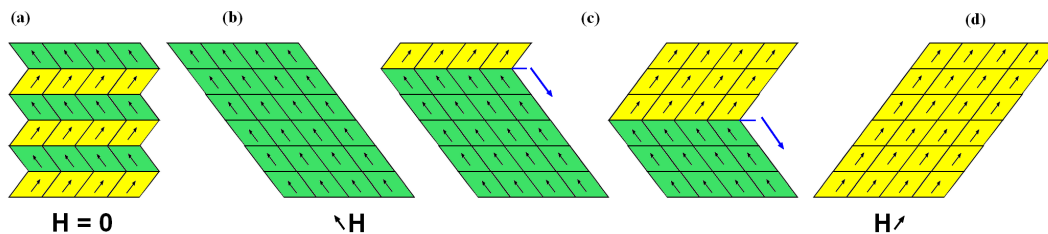


**Fig. 13:** Schematic depiction of the reorientation of the twinned microstructure by magnetic field  $\mathbf{H}$ . (a) Spontaneously twinned microstructure consisting of two martensite variants after the martensitic transformation. (b) Microstructure consisting of a single martensite variant induced by the magnetic field  $\mathbf{H}$ . (c) Reorientation of the twinned microstructure carried by the twin boundary motion upon the changes of the magnetic field. (d) Fully reoriented single variant state consisting purely of the second martensite variant.



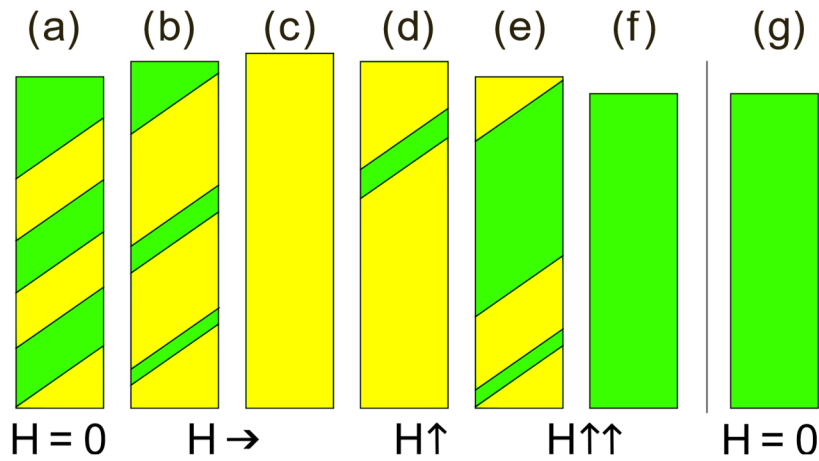


**Fig. 14:** Schematic depiction of the MIR effect on sample length. (a) Spontaneously twinned microstructure consisting of two martensite variants. (b) When the magnetic field  $H$  is applied, twin variants reorient via twin boundary motions. (c) Fully reoriented state. (d) When the field is applied in perpendicular direction, suitably oriented variant nucleates. (e) Microstructure reorients via twin boundary motion. (f) Fully reoriented state. (g) Sample remains reoriented when the field is switched off.

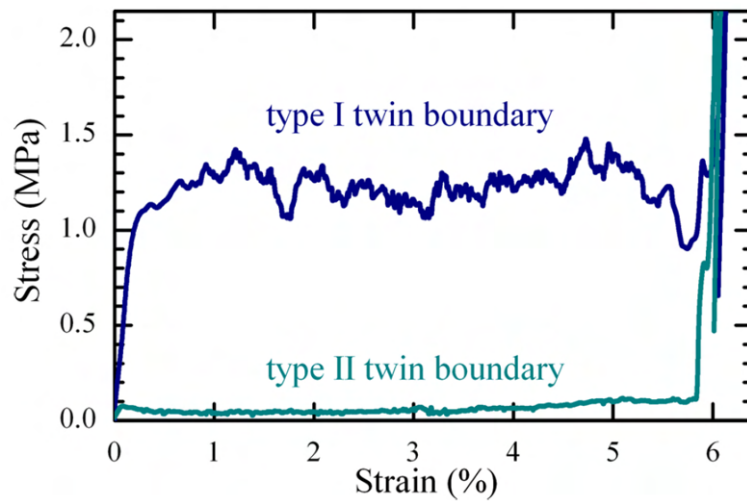


**Fig. 15:** Typical stress-strain curves for the type I and type II twin boundaries [38]

## 1.5 Martensite phases of Ni-Mn-Ga and the current state of art

Since we are now familiar with the basics of the MSM effect, let us now focus on the material - the Ni-Mn-Ga-based alloys, their particular martensite phases and their specifics. Since modulated phases are going to be discussed in this chapter, if uncertain, reader is kindly advised to consult Appendix I: General introduction into structural modulation.

### 1.5.1 Introduction to the Ni-Mn-Ga-based alloys and their martensites

The Ni-Mn-Ga system represents the archetype of magnetic shape memory alloy. It is exactly this alloy, on which the magnetic shape memory effect was discovered by Kari Ullakko in 1996 [1]. Martensites of Ni-Mn-Ga exhibit giant magnetic field-induced strain (MFIS) (up to 12%) in a moderate magnetic field (<1 T). [47]

The stoichiometric  $\text{Ni}_2\text{MnGa}$  has a cubic austenite with  $a = 5.82 \text{ \AA}$ . It transforms to modulated martensite phase with ( $a \sim b \sim 5.92 \text{ \AA}$ ,  $c \sim 5.56 \text{ \AA}$ ) around  $T \sim 200 \text{ K}$ . [25,37,48,49]. The transformation is associated with very small volume changes of the unit cell. For compositions close to stoichiometric  $\text{Ni}_2\text{MnGa}$ , the transformation to martensite can be preceded by the premartensitic transition to 3M modulated structure around  $T \sim 250 \text{ K}$ . [12,37,50] Nevertheless in our range of stoichiometries this phase was not observed during our later presented experiments and therefore it will not be discussed further.

In general, the Ni-Mn-Ga-based alloys (often off-stoichiometric), are rich in martensite phases: It is commonly accepted that three (in some cases approximate) types of particular martensitic phases can be distinguished in our system: five-layered modulated (named 5M or 10M), seven-layered (named 7M or 14M) and non-modulated (abbreviated NM) martensite. [37] This nomenclature is based on the closest rational approximant of the modulated phases. Nevertheless, it will be later shown that different modulation vectors have been reported within the modulated martensite types. This creates a great deal of confusion that can be found in the literature: Some groups use the term “7M modulated martensite” for the structure with  $q \sim 3/7$  (defined following  $\mathbf{q} = q \mathbf{g}_{110}$ , where  $\mathbf{g}_{110}$  is the  $[110]^*$  reciprocal vector, see Appendix I for definition of the modulation vector) while concluding, that the labels such as 5M-, 7M-type modulated structure of the martensite phase are fraught with ambiguities. [54] Indeed, other MSM groups use “7M” label for structure with  $q \sim 2/7$  and consider  $q \sim 3/7$  a variation of “5M” phase [52,53]. Further confusion originates from the fact, that the symbols like 10M, 14M etc., are often used for two different things: while number always represents the number of layers, M sometimes represents the monoclinic symmetry [54] and sometimes modulation.

From the practical point of view, these three types of martensite can be clearly distinguished based on the magnetic, electrical, elastic, and other properties.

Depending on the composition, martensite phases can be connected by intermartensitic transformations. The usual full sequence of transformations in Mn-rich Ni-Mn-Ga during cooling is: paramagnetic cubic austenite, ferromagnetic cubic austenite, ferromagnetic modulated 10M martensite, ferromagnetic 14M martensite and finally ferromagnetic non-modulated (NM) martensite, schematically depicted in **Fig. 16**. [25] In some cases, some of the phases of this sequence do not appear, since the transformation path is strongly dependent on chemical composition, atomic order and possibly also on the thermo-mechanical history of the specimens. [26,49] The dependence on composition is often drawn (although not fully satisfactorily) based on the electron concentration  $e/a$ , or a number of non-bonding electrons  $N_e/a$  [37,55–57]. Simple schematic phase diagram for  $\text{Ni}_{50}\text{Mn}_{25+x}\text{Ga}_{25-x}$  alloys with increasing Mn content is shown in **Fig. 17**.

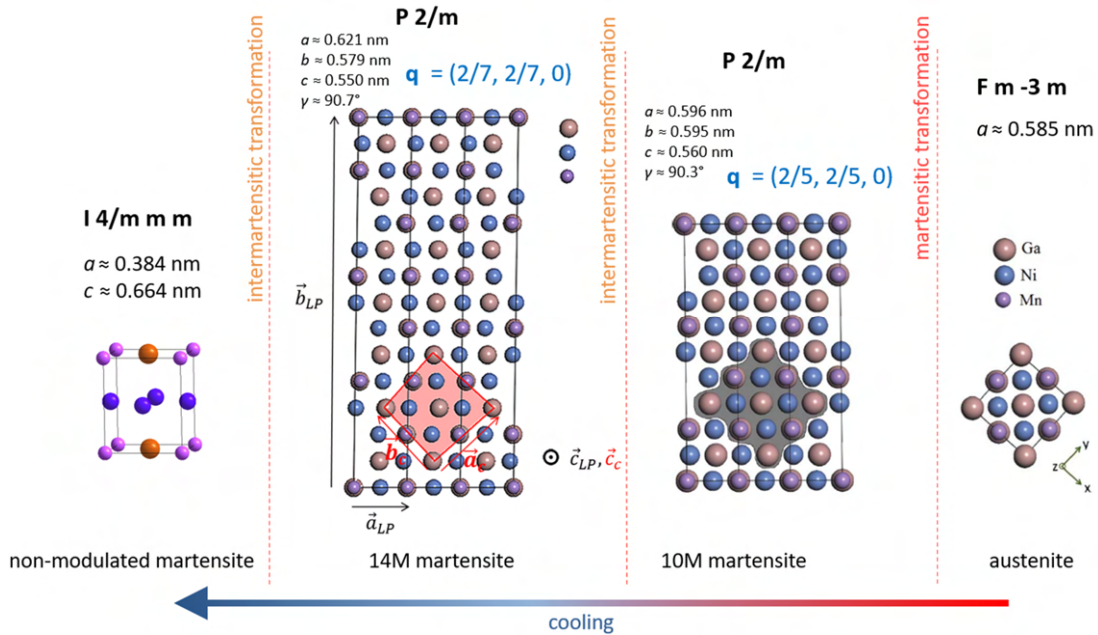


**Fig. 16:** Schematic depiction of the typical transformation sequence for the Mn-rich Ni-Mn-Ga alloy during cooling. In case of the modulated 10M and 14M martensites, two kinds of coordinates are demonstrated: the long-periodic (LP) unit cells containing the full modulation wave and the pseudo-austenitic/pseudo-cubic unit cells in which the modulation propagates in the  $[110]^*$  direction. See also **Fig. 18**.

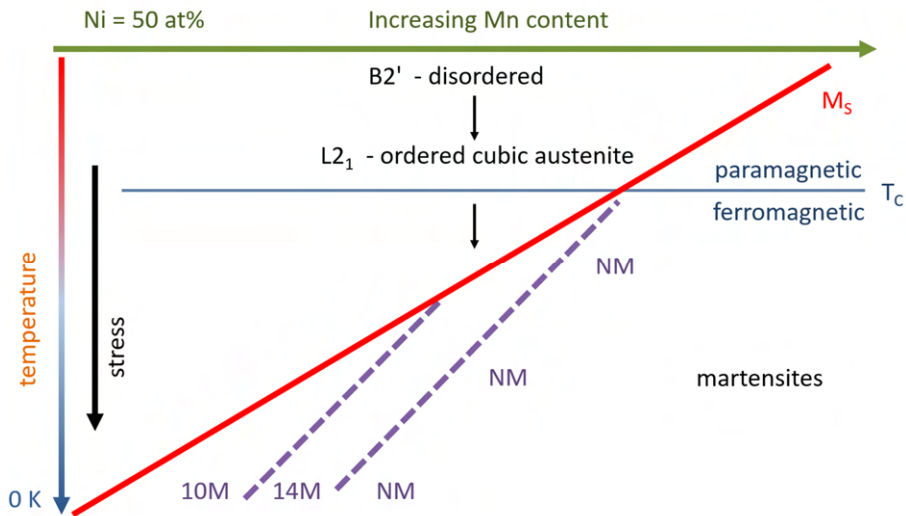


**Fig. 17:** Schematic phase diagram for typical  $\text{Ni}_{50}\text{Mn}_{25+x}\text{Ga}_{25-x}$  material with increasing Mn content. The red line represents the martensitic transformation; the blue line represents paramagnetic-ferromagnetic transformation at the Curie temperature. Dashed lines represent the intermartensitic transformations. Adapted from [26].

As indicated in the figure and in literature, e.g. [49], the transformation temperatures vary strongly with changes in composition. Some additional general tendencies might be found: the martensitic transformation temperature increases with increasing the Ni content, in high-temperature region it merges with the ferromagnetic-paramagnetic transition and further increase shifts the martensitic transformation above the  $T_C$ . The dependence concerning other elements is complex and not yet fully described. [37] It has been demonstrated (either by experiment or first-principles calculations), that martensitic transformation properties may change drastically by alloying of a fourth element, such as Fe, Co and Cu or other transition elements, or even by multiple elements together. [40,58–61]

### 1.5.2 Five-layered modulated martensite (named 5M or 10M)

From the application point of view, the compositions with the martensite stable at the room temperature and above are desired, together with as high  $T_C$  as possible, since the MIR effect operates only at temperatures below  $T_C$  and below the martensitic transformation temperature. [49] Here, the 10M modulated martensite phase seems to be the most promising one, thanks to its extremely high twin boundary mobility (twinning stress lower than 0.1 MPa has been reported [62]) and to 7 % magnetic field induced strain in a moderate field of the order of 0.1 T [63] at room temperature [64] and down to 2 K [65].

For the basic description of this phase, rational approximant with the modulation over 10 (220) atomic planes is usually used, **Fig. 16**. Originally, the unit cell was reported to be tetragonal. [25,66]. Thanks to the better instrumental resolution and careful experiments, the structure is nowadays mostly described using monoclinic unit cell with lattice parameters  $a_{\text{pCub}} \sim 5.97 \text{ \AA}$ ,  $b_{\text{pCub}} \sim 5.94 \text{ \AA}$ ,  $c_{\text{pCub}} \sim 5.58 \text{ \AA}$ ,  $\gamma \sim 90.3^\circ$ , where we used the subscript “pCub” for clarity. Here, so called "pseudo-austenitic" or “(pseudo-)cubic” coordinates are used. These keep the orientation of the axes similar to the austenite lattice. Such description is practical since it allows direct comparison of physical properties between individual phases. We will stick to these coordinates and indexing in our work as this is widely used in the field. [37,44,49,66–68]

Nevertheless, from the purely crystallographic point of view, several advanced structure studies indicate more appropriate choice of smaller  $45^\circ$  rotated unit cell with orthorhombic symmetry and lattice parameters  $a_{\text{diag}} \sim 4.22 \text{ \AA}$ ,  $b_{\text{diag}} \sim 5.58 \text{ \AA}$ ,  $c_{\text{diag}} \sim 4.20 \text{ \AA}$ . These coordinates are sometimes called “diagonal coordinates” in the field. Here, the structural modulation goes in the  $\mathbf{c}^*$  direction and the relations of the lattice parameters to those of the monoclinic unit cell are:  $a_{\text{pCub}} = \sqrt{2} a_{\text{diag}}$ ,  $b_{\text{pCub}} = \sqrt{2} c_{\text{diag}}$ ,  $c_{\text{pCub}} = b_{\text{diag}}$ . For clarity, illustration of both cells is shown in **Fig. 18**.

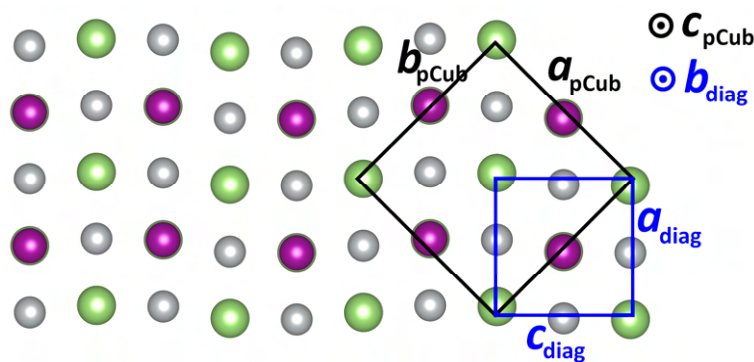


**Fig. 18:** Illustration of the relation between the pseudo-cubic unit cell (black, marked “pCub”) and the smaller orthorhombic unit cell (blue, marked “diag”) indicated by some current structure studies.

More insight is necessary here to deal with the lack of monoclinicity in such a structure, especially when the monoclinic distortion is clearly observable, e.g., by optical microscopy with Nomarski contrast. Currently (end of 2022), additional experiments employing dedicated single crystal X-ray diffractometer are performed in this direction of research, see chapter 5.

This shows that the structure of the 10M modulated martensite is still under discussion and many questions emerge. Regardless on the chosen unit cell, in X-ray and neutron diffraction experiments, one can limit him/herself to the studies of the modulation satellites between principal reflections (regardless on the indexing) in detail. The outcomes of such approach are immediately applicable to both used conventions. Nevertheless, the character of the modulation is still an open question.

Different scientific groups reported different modulation vectors (especially their magnitude) for various compositions. Although different coordinate systems are chosen for the description in the original articles, we will now provide the summary transferred to pseudo-austenitic lattice for all the cases. We will use the modulation vector  $\mathbf{q} = q \mathbf{g}_{110}$ , where  $\mathbf{g}_{110}$  is the  $[110]^*$  reciprocal vector.

#### *10M modulated martensite in stoichiometric Ni<sub>2</sub>MnGa*

The structure of the stoichiometric Ni<sub>2</sub>MnGa has been first examined by Webster et al. [69] based on the analysis of this Weissenberg photographs using instrument D12 at ILL Grenoble. In their work, they describe complex tetragonal structure that appears on cooling below 202 K with lattice parameters  $a = 5.920 \text{ \AA}$ ,  $c = 5.566 \text{ \AA}$  and many satellite reflections denoting long-periodic order. [69] Later on, many attempts have been made in refining the structure:

Currently accepted structure model of “10M” modulated martensite of stoichiometric Ni<sub>2</sub>MnGa is widely based on powder diffraction studies of Righi et al. [70,71] In the contrary to previously believed tetragonal lattice, they report an orthorhombic phase with incommensurate modulation ( $q = 0.4248(2)$  at 100 K), superspace group  $\text{Immm}(00\gamma)s00$ . Interestingly, in the same study they also report commensurate case with  $q = 2/5$  for non-stoichiometric Mn-rich composition (see below). [71]

Based on single crystal ND and synchrotron PXRD, Kushida et al. [72] reports incommensurate modulation for the stoichiometric Ni<sub>2</sub>MnGa alloy below approx. 220 K with slight shift of the modulation satellites on cooling. For 4.2 K temperature,  $q \sim 0.428$  ( $\sim 3/7$ ) is reported. They used harmonic modulation function in their work. [72]

Fukuda et al. continues the studies with electron diffraction. They report  $q = 0.427(5)$  at 21 K. [73]. Interestingly, they also report satellites of minor intensity in the unusual  $[100]^*$  direction (using the pseudo-austenitic or “cubic” coordinates). They explain these as either double diffraction or an existence of transition state. [73]

Mariager et al. studied stoichiometric Ni<sub>2</sub>MnGa single crystal with SXR. They report  $q = 0.428(3)$  at 200 K. Possible higher ( $>5$ ) order satellites are apparent from their  $q$ -scans plotted in logarithmic scale. Nevertheless, they are not sufficiently addressed (if they are not ignored at all).

Altogether, the situation appears to be quite clear for the stoichiometric Ni<sub>2</sub>MnGa and the reports are in a good agreement. Nevertheless, although this alloy seems interesting from the fundamental point of view, its applications are not very promising given its stability only below 220-210 K. Surprisingly, in all these studies, values of  $q \sim 0.428$ , equal to  $q = 3/7$  within experimental error are interpreted as incommensurate.

#### *10M modulated martensite in non-stoichiometric Ni-Mn-Ga alloys*

Based on powder X-ray and neutron diffraction measurements, Righi et al. [71] in 2007 reported commensurate ( $q \sim 2/5$ ) modulated monoclinic martensite for the Ni<sub>50</sub>Mn<sub>28.75</sub>Ga<sub>21.25</sub> alloy. Later on, they report both commensurate ( $q \sim 2/5$  at room temperature) and incommensurate ( $q = 0.412$  at 83 K) modulation for the Ni<sub>48.75</sub>Mn<sub>29.75</sub>Ga<sub>21.5</sub> alloy [52]. Recently, Righi reported incommensurate modulation of the Ni<sub>51.75</sub>Mn<sub>23.25</sub>Ga<sub>25</sub> alloy ( $q = 0.410$  at 250 K,  $q = 0.422$  at 220 K) [74].

Çakir et al. [75] carried out a thorough PXRD and neutron spectroscopy study for various Ni-Mn-Ga compositions. During these they observed evolution of the modulation vector upon cooling, where  $q$  increases with decreasing temperature, ranging from  $q \sim 2/5$  to  $q \sim 3/7$ . This interval is spread among different compositions, where only one alloy started at  $q \sim 2/5$  (above room temperature) and only one (different) alloy attained  $q \sim 3/7$  (at 10 K) [75].

A unifying theory connecting these intermittent reports is still missing. Furthermore, since the twin boundary mobility was reported to be highest in the 10M martensite, possible connection of the modulation effect on twinning creates an interesting direction for research and needs clarification.

### 1.5.3 Seven-layered modulated martensite (named 7M or 14M)

The 14M modulated phase was first reported to be orthorhombic [25]. Similarly to the 10M martensite, the monoclinic unit cell is currently believed to be fitting one with lattice parameters  $a \sim 6.19 \text{ \AA}$ ,  $b \sim 5.78 \text{ \AA}$ ,  $c \sim 5.50 \text{ \AA}$ ,  $\gamma \sim 90.6^\circ$  in pseudo-austenitic coordinates [25,53,76]. In contrast to the 10M modulated phase, commensurate modulation with modulation vector  $q = 2/7 [110]^*$  stable in the whole temperature interval is commonly accepted with the modulation over 14 (220) atomic planes, **Fig. 16**.

When it comes to material functionality, twinning stress of 0.64 MPa has been reported in Ni-Mn-Ga single crystal with MFIS of 11.2%. [76] Recently, low twinning stress of 0.2 MPa for type I and 0.1 MPa for type II twin boundaries has been reported by Sozinov et al. in 5%Fe alloyed Ni-Mn-Ga with MFIS of 12 % [53]. These values are attaining the theoretical maximum given by the lattice parameters.

### 1.5.4 Non-modulated (NM) martensite

The non-modulated (NM) martensite represents the basic stable structure, usually occurring at the lowest temperatures. The unit cell is tetragonal with lattice parameters  $a = b \sim 5.52 \text{ \AA}$ ,  $c \sim 6.44 \text{ \AA}$  in pseudo-austenitic coordinates [66] or  $a = b \sim 3.84 \text{ \AA}$ ,  $c \sim 6.44$  when using the crystallographically appropriate  $45^\circ$  rotated primitive cell, space group  $I4/mmm$ , **Fig. 16**. Twin boundary mobility is negligible and twin variants are hard to reorient (if possible). High twinning stress of 6.7 MPa has been reported [77] and giant MFIS was never observed for this phase in pure Ni-Mn-Ga. However, later Sozinov et al. reported the high MFIS of 12% at 1.05 T for the non-modulated martensite of 4%Co-4%Cu-alloyed Ni-Mn-Ga [47,78]. Nevertheless, given the relatively large magnetic field, the application potential of the non-modulated martensite is low.

### 1.5.5 Intermartensitic transformations

As the different types of martensites usually pose different physical properties, it is from the application point of view important to study also the intermartensitic transformations between individual martensites of Heusler alloys. These can be in fact understood as the phase transformations on their own, although, following some approaches, these can also be understood as the rearrangement of the structural nanodomains. [79–81] As well as the martensitic transformation, the intermartensitic transformations are highly dependent on the composition.

## 1.6 Suitable diffraction methods for the characterisation of the martensites of Ni-Mn-Ga-based alloys

Here we focus on the diffraction methods convenient for practical analyses Ni-Mn-Ga samples, considering difficult combination of structural modulation, hierarchical twinning, crystal mosaicity and difficult nature of our samples. Given by the necessity to deal with twinning on various scales, usually X-ray diffraction and neutron diffraction are used and these will be addressed in detail.

### 1.6.1 X-ray diffraction methods

When it comes to X-ray diffraction, usually two groups of conventional diffractometers are recognized: the dedicated single-crystal diffractometers and the multipurpose (often referred to as powder) diffractometers. When it comes to our specific material, both of the methods have advantages and disadvantages which will shortly be introduced together with the application possibilities. At the end of the chapter, specifics of synchrotron X-ray diffraction are briefly addressed.

#### 1.6.1.1 Dedicated single-crystal diffractometers

Generally, the single-crystal XRD represents the very base of structure solution based on the automated collection of the diffraction pattern from the whole instrumentally achievable reciprocal space. Nowadays, most of the XRD single-crystals studies are carried out in dedicated laboratory four- or six-circle single-crystal diffractometers (usually in kappa-geometry) or their analogues in synchrotron facilities.

Conventional in-lab single-crystal diffractometers usually need samples of small sizes ( $< 1 \text{ mm}^3$ ), as the whole sample should be emerged in the relatively small but highly focused and intense X-ray beam.

The inevitable twinning of martensite leads to the simultaneous collection of the diffraction patterns from differently oriented twin domains. Together with structural modulation (bringing even more diffraction spots) and the higher crystal mosaicity usually observed for Ni-Mn-Ga crystals, this attains the limits the instrumental resolution and represents a real challenge. The resolution of dedicated single-crystal X-ray diffractometers is usually relatively lower, but this apparent disadvantage is counterbalanced by the collection of the large number of reflections. Unfortunately, this could easily lead to misinterpretations caused by the overlapped peaks, especially in the cases close to merohedral twinning.

For these reasons, only the structures of austenite and non-modulated martensite have been solved reliably so far with dedicated in-lab single-crystal XRD and many contrasting reports exist for the modulated phases.

To the category of single-crystal diffractometers belong also the Laue diffractometers. These do not usually represent a tool for more complex structural analyses, but are typically used for the orientation of the larger single-crystals. Application of the Laue diffraction on Ni-Mn-Ga-based single crystals will be discussed later in 3.1.

#### 1.6.1.2 Multipurpose / powder diffractometer

Multipurpose diffractometers are mainly designed for the analyses of larger bulk polycrystalline samples, powders, and thin layers. They are common in the modern material physics laboratories as they offer broad field of practical application, i.e., analyses of phase composition, texture and residual stress of polycrystals. Importantly, they can be employed for the complete structure solution from powder samples. Furthermore, they also excel in various in-situ experiments, including not only

measurements during heating or cooling (usually possible also for dedicated single-crystal diffractometers) but also measurements under stress or strain, or theoretically even measurements in the magnetic field.

The multipurpose diffractometers can be also used for the analyses of the single crystals. Even though do not usually represent a tool for a complete structure solution in this case, they are capable of applied research regarding the practical applications of the MSM alloys. This includes determination of the phase, lattice parameters, presence of twinned domains, studies of structural modulation etc. The great advantage is the ability to study the large bulk samples in which the MIR was confirmed previously and that are directly suitable for various other forms of analyses (such as mechanical testing, magnetic measurements, measurements of transport properties etc.).

The notable advantage of the multipurpose diffractometers in our case is the choice of the optics: especially the choice between the divergent or parallel optics and optional high-resolution setups. In case of twinned and mosaic crystals, beam divergence plays a crucial role for fast analyses (later discussed in 2.2.3). Furthermore, selectable length and width of the irradiated area allows to measure the large surface at once or to focus on smaller areas (down to tens of  $\mu\text{m}$ ) in case of large crystals.

#### 1.6.1.3 Synchrotron X-ray diffraction

Presented thesis would not be complete without a brief mention of the synchrotron X-ray diffraction (SXRD). Nowadays, SXRD is performed in both single crystal and powder dedicated setups. Tuneable wavelength allows fitting of the instrument to specific experimental needs, e.g., to avoid fluorescence. High energy photons allow higher effective penetration depth and studies of bulk effects. Higher brilliance allows better counting statistics and nearly parallel beam ensures the high resolution. Nevertheless, the parallel beam setup might be slightly problematic in case of non-ideal twinned single crystals (see chapter 2.2.3 for more).

#### 1.6.2 Neutron diffraction

Similarly to the XRD, the neutron diffraction can also be used in various dedicated setups (further including also the time-of-flight method). Although both XRD and ND share the vast amount of the diffraction-related theory, there exist major differences between these two methods, majority of which originates from the differences between the properties of photons and neutrons. Let us now note those, that are directly related to our research. The complete overview is provided, e.g., in [82].

- Absorption: the effective penetration depth of the neutrons is several orders higher than that of the X-rays. I.e., the effective penetration depth  $D_{99\%}$  (the thickness of the sample, where 99 % of the information recorded in a diffractogram originates from) of X-ray in stoichiometric  $\text{Ni}_2\text{MnGa}$  is  $\sim 15 \mu\text{m}$  (calculated for the Cu radiation), while for neutrons it is  $\sim 10 \text{ mm}$ . This makes the ND capable of studying the real bulk effects [83,84], while the XRD information originates only from the relatively thin surface layer. Irradiation of the larger volume also helps while dealing with polycrystals or larger grains. ND is usually not suitable for samples of small volumes.
- Magnetic structure: unlike X-ray photons, neutrons carry magnetic moment ( $\mu = 1.913 \mu_B$ , where  $\mu_B$  is the Bohr magneton) and spin ( $I = 1/2$ ). Because of this, they interact with the magnetic moments inside of material and the magnetic contribution is superimposed to the structural one. The ND is therefore widely used for the studies of the magnetic structure of solids.
- Sensitivity to different elements and isotopes: the scattering amplitude of X-ray is a monotonous function increasing with increasing atomic number  $Z$ . In contrast, the neutron scattering amplitude is a complex value originating from the potential and resonant scattering.



Thanks to the second, the scattering amplitude changes noticeably (or even change sign) for neighbouring elements and even isotopes. This in theory allows the precise studies of atomic occupancies with ND.

- **Intensity:** The flux of the monochromatized neutrons hitting the sample is generally several order lower than the flux of X-ray photons. Because of this, the intensity of the diffracted beam is usually lower for the ND, even when using the most brilliant sources available (such as in Institut Laue-Langevin, Grenoble). To collect sufficient data allowing to study the modulation satellites with the intensity several orders lower than the strong principal peaks, one usually needs longer measuring time. This is slightly counterbalanced by usually better signal-to-noise ratio of the ND compared to the XRD.
- **Resolution:** The diffraction peak width in ND is usually up to 100 times larger than that of the high-resolution XRD [82]. Because of this, the peak overlapping caused by twinned martensite represents even bigger problem for the ND.

To sum up, the ND represents a valuable tool for the characterisation of the Ni-Mn-Ga-based alloys. Not only it allows the studies of the magnetic structure and atomic occupancies, but it also excels in some other practical aspects, such as ability to analyse the real bulk volume of the crystals.

## 1.7 Fundamental question of Ni-Mn-Ga polycrystals

Although many structure (and other) studies have been performed with polycrystals and powders of Ni-Mn-Ga-based alloys, major limitation of these needs to be noted. It has been shown that the grain boundaries restrict twin boundary motion and the MIR functionality extensively [37,85]. Random polycrystals are not expected to show large deformation in magnetic field due to blocking by adjacent grains. Textured polycrystals might exhibit MIR in some directions, nevertheless, the MIR effect is not as strong as in single crystals and material is often prone to cracking. [37] Only recently, Wójcik et al. reported MFIS of 1.15% in melt-spun ribbons of strong fibre texture and homogenous microstructure with no crack formation [86].

As the polycrystalline nature influences the very nature of the MSM alloys, the validity of the fundamental results obtained from bulk polycrystals and powders can be speculated about. Therefore, we strongly believe that the fundamental structural studies should be performed on single crystals that were previously proved to show the MIR and highly mobile twin boundaries. The most pivotal parts of the presented work will therefore be done on such samples.

Nevertheless, we fully agree that the growth of single crystals is often difficult and time-consuming and, especially in the case of our alloys, it often ends with failures. Therefore, the possibility of fast production of highly textured polycrystals and oligocrystals with large enough grains that clearly exhibit the MIR functionality represents a stepping stone in the experimental research of the new Ni-Mn-Ga-based alloys. Thus, part of the presented work will follow this direction.

## 2 Experimental

### 2.1 Materials

I have studied pure Ni-Mn-Ga samples of different stoichiometries as well as the Ni-Mn-Ga-based samples with alloying elements, such as Co, Fe, Cr and Cu. Given the various sample forms (bulk polycrystals, single crystals etc., see **Fig. 19** for illustration), two typical sample groups are described in detail in the sub-chapters below. Full list of analysed samples is provided in the table included as Appendix II.

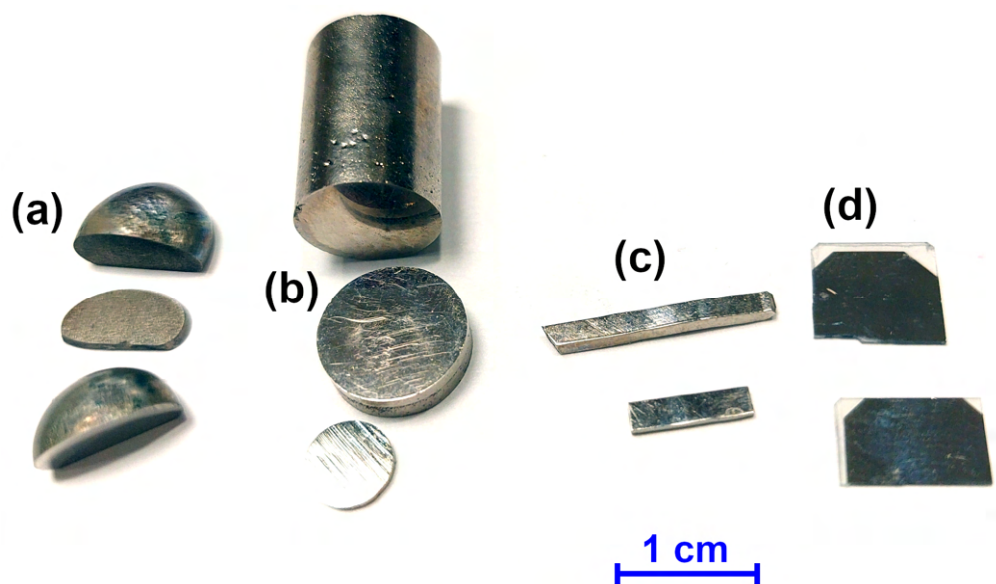


**Fig. 19:** Typical Ni-Mn-Ga samples. (a) Bulk polycrystals created by arc-melting. (b) Large single crystals and oligocrystals created by optical floating zone furnace. (c) Oriented and cut single crystal samples with visibly twinned microstructure. (d) Epitaxial thin layers grown on MgO substrate.

#### 2.1.1 Single crystals

Single crystals of the Ni-Mn-Ga and Ni-Mn-Ga-based alloys with 1-5% of Fe, Cu or Co content in broader range of nominal compositions have been studied. Single crystals were grown by modified Bridgeman-Stockbarger method in *Adaptamat Ltd.* and *GoodFellows*, and by floating-zone melting method at the *Charles University* and at the *FZU*. In some cases, crystal growth resulted in formation of oligocrystals containing multiple larger grains within one rod.

In case of true single crystals, resulting crystals were usually annealed, oriented by XRD and cut into samples of parallelepiped shape, **Fig. 19** (c). Resulting samples were polished by the grinding paper and electropolished if needed.

#### 2.1.2 Polycrystalline and oligocrystalline bulk samples

Analysed polycrystalline bulk samples of Ni-Mn-Ga and Ni-Mn-Ga-based alloys with 1-5% of Fe, Cu, Cr or Co content were prepared at the *FZU* by arc-melting. Resulting pellets, **Fig. 19** a), were annealed, cut into samples by spark erosion machine and polished by SiC grinding paper up to the grid of 2400. The later analyses showed that these samples are usually of oligocrystalline or highly textured polycrystalline nature.

## 2.2 Diffraction studies

The structure of materials was characterised by the X-ray and neutron diffraction. Experimental details are listed below together with the description of the data processing or other important information.

### 2.2.1 X-ray diffraction

The X-ray diffraction studies were carried out employing the following diffractometers:

- PANalytical X'Pert PRO diffractometer at the *FZU* with Co and Cu X-ray tubes in following geometries:
  - Bragg-Brentano semi-focusing geometry used with line focus and divergent slits selected based on the sample dimensions. For smaller samples and pole figure measurements, point focus was used. In both cases, we used fast PANalytical X'Celerator detector.
  - Parallel beam geometry with the Co tube ( $\lambda_{K_{\alpha 1}} = 1.78901 \text{ \AA}$ ), parabolic mirror and PW3011/20 point detector equipped with parallel plate collimator (maximum acceptance of  $0.09^\circ$ ).

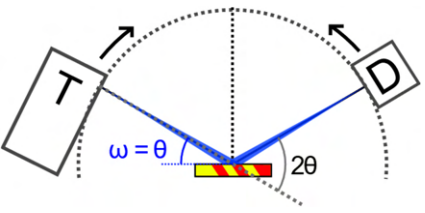
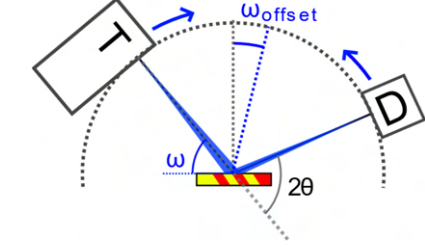
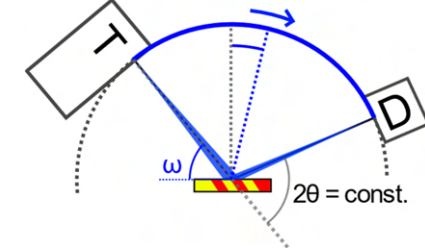
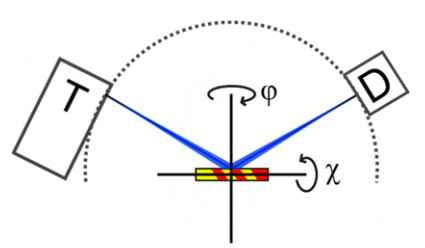
Diffractometer was equipped with flat sample holder for bulk polycrystalline and powder samples, and ATC-3 texture cradle for pole figure measurements and single-crystal studies. For in-situ experiments, simple Peltier element for sample heating or custom build heating/cooling stage with temperature range of 250 – 400 K was used. This diffractometer was used for most of our measurements of single crystals and bulk oligo- and polycrystals.

- Rigaku SmartLab diffractometer at the *FZU* with Cu tube ( $\lambda_{K_{\alpha 1}} = 1.54060 \text{ \AA}$ ) in Bragg-Brentano and parallel beam geometry with line focus, employing 2D detector HyPix 3000 and optional Anton Paar DCS500 heating/cooling stage for in-situ heating/cooling (temperature range 80 – 770 K). This diffractometer was used mainly for the standard symmetric and asymmetric  $2\theta$ - $\omega$  scans at different temperatures and later for the fast reciprocal space mapping.
- Bruker D8 Discover diffractometer at the *FZU* with rotating Cu anode equipped with Anton Paar DCS350 heating/cooling stage for in-situ heating/cooling (temperature range: 80 – 620 K) and point detector. Device was used primarily for the reciprocal space mapping and the q-scans.
- PANalytical Empyrean diffractometer at the LUT University, Mikkeli, Finland employing the high-resolution optics with parallel beam (Ge hybrid monochromator combining the monochromator + the parabolic mirror) and the PIXcel<sup>3D</sup>–Medipix3 1x1 detector. Measurements were done mainly at the room temperature. Custom-built heating element was used for measurements with temperature from RT to 350 K. This diffractometer was mainly used for fast high-resolution reciprocal space mapping and high-resolution symmetric and asymmetric  $2\theta$ - $\omega$  scans.
- Laue diffraction analysis was performed at the *FZU* with Seifert ISO-Debyeflex 3003 X-ray generator with W tube. Diffracted pattern was collected using a laser stimulated fluorescence image plate.

## 2.2.2 X-ray diffractometer angles and scan types

For clarity, the diffractometer axes and measurement types are illustrated and described in **Table 1**. Description follows PANalytical definition of the axes and scans.

**Table 1:** Description of diffractometer angles and measurement types used in the thesis

<p><b>Gonio</b> Standard 1D symmetrical Bragg-Brentano scan, i.e., the X-ray tube (T) and the detector (D) move symmetrically with respect to the vertical line. Here, <math>2\theta</math> is the diffraction angle and <math>\omega</math> is the beam incidence angle.</p>	
<p><b>2θ-ω</b> Standard 1D asymmetrical Bragg-Brentano scan, i.e., tube and detector move symmetrically with respect to the new line defined by <math>\omega_{\text{offset}}</math> angle. This scan is identical to Gonio for <math>\omega_{\text{offset}} = 0^\circ</math>.</p>	
<p><b>ω scan</b> = Rocking curve measurement = <math>\omega_{\text{offset}}</math> scan in our experimental setup. Intensity as a function of <math>\omega_{\text{offset}}</math> while keeping the <math>2\theta</math> constant.</p>	
<p><b>χ (chi) scan (= ψ (psi) scan in older software)</b> Intensity as a function of χ angle (= sample tilt).</p> <p><b>φ (phi) scan</b> Intensity as a function of φ angle (= sample rotation). φ axis is connected to χ axis, i.e., when <math>\chi \neq 0^\circ</math>, axis of rotation is inclined.</p>	
<p><b>2D 2θ_ω</b> 2D map consisting of a set of continuous <math>2\theta</math> scans collected for different <math>\omega</math> angles (in steps).</p>	
<p><b>2D 2θ-ω_ω_offset</b> 2D map consisting of a set of continuous <math>2\theta</math>-ω scans collected for different <math>\omega_{\text{offset}}</math> angles (in steps).</p>	
<p><b>2D 2θ-ω_χ</b> 2D maps consisting of a set of continuous <math>2\theta</math>-ω scans collected for different χ angle (in steps).</p>	
<p><b>Pole figure</b> Texture scan, 2D scan: intensity as a function of <math>(\chi, \phi)</math>, consists of a set of continuous φ scans (0-360°) collected for selected range of χ tilts (in steps).</p>	

Pole figures in the dissertation follow the XRD standard choice of coordinates, shown in **Fig. 20** for clarity. In all the presented pole figures,  $\chi$  axis covers the whole interval of  $0 - 90^\circ$  while the interval that was not measured is kept empty.

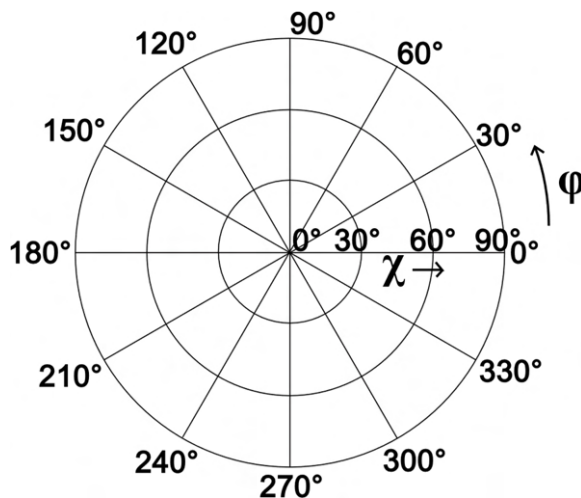


**Fig. 20:** Illustration of the pole figures coordinates used in the thesis

In case of divergent optics with the X'Celerator detector, the detector was used in Receiving slit mode, i.e. the intensity was added together in the selected  $2\theta$  acceptance range (selectable from  $0.5^\circ$  to  $2.1^\circ$ , **Fig. 21**), during measurements of the  $\varphi$ ,  $\chi$ , and  $\omega$  scans and pole figures. Unless stated differently, the full acceptance range was used for the pole figures presented in this thesis.

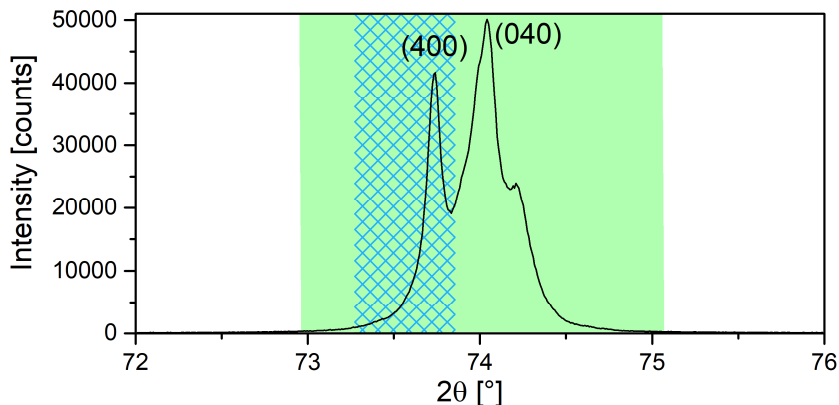


**Fig. 21:** Schematic illustration of the possible choices of the detector acceptance range. The  $2\theta$  scan reveals the overlapped (400) and (040) reflections, both consisting of  $K_\alpha$  doublets. The pole figure measurement at the  $2\theta = 74^\circ$  with the full  $2.1^\circ$  detector acceptance angle (green) would bring the summed information on the orientation of both  $a$ - and  $b$ -oriented variants. When more detailed information on particular variant orientation is needed, smaller detector acceptance angle of min.  $0.5^\circ$  can be chosen (blue pattern). The pole figure will then contain mostly the information on the orientation of the  $a$ -oriented variant, with some residue from the  $b$ -oriented variant given the broad peaks with overlap.

Similar settings are available for other listed constant-wavelength diffractometers as well. In case of Rigaku SmartLab and PANalytical Empyrean, additional modes were available due to the presence of the 2D detector that brings the ability to collect the full 2D image for each step. This in practice allows collection of the complete data within the full range of the detector and then selecting the appropriate range for the intensity integration (analogous to the one presented in **Fig. 21**) later during the data processing.

### 2.2.3 Advantage of beam divergence in the studies of MSM single crystals

Our measurements benefit from the combination of divergent beam geometry and 1D detectors featuring Real Time Multiple Strip (RMTS) technology or 2D detectors bring the availability of scanning line mode measurements. During these, both arms of the diffractometer move in a standard way of Gonio or  $2\theta$ - $\omega$  scans, while the intensity is collected over an array of parallel solid-state detectors (in case of RMTS) or lines of the 2D detector. I.e., the intensity at particular  $2\theta$  position (data point) during Gonio or  $2\theta$ - $\omega$  scan is measured and then summed, until the data point is no longer in range. When X'Ceerator detector is used, the total active length is  $\sim 8.9$  mm, which for our detector arm length of 240 mm corresponds to the acceptance angle slightly larger than  $2^\circ$ , **Fig. 22**.

Thanks to this, contributions from the crystallites, mosaic blocks or crystallographic twin domains misoriented up to  $\sim 1^\circ$  (in case of X'Ceerator detector) from normal direction can be observed simultaneously, depending on the divergence of the incident beam and selected active length of the detector. The beam divergence in vertical direction is usually controlled by the appropriate choice of divergence slits. Divergence in the horizontal direction can be controlled by introduction of the Soller slits.

In case of twinned martensites of Ni-Mn-Ga-based alloys, the beam divergence brings valuable advantage. Since the difference in the orientation of some of the reflections from the individual twinned martensite variants is relatively small, contributions multiple variants can often be detected in one single 1D scan. Furthermore, as our crystals usually have larger mosaicity [87], the contributions from all the mosaic blocks are summed in the divergent beam setup.

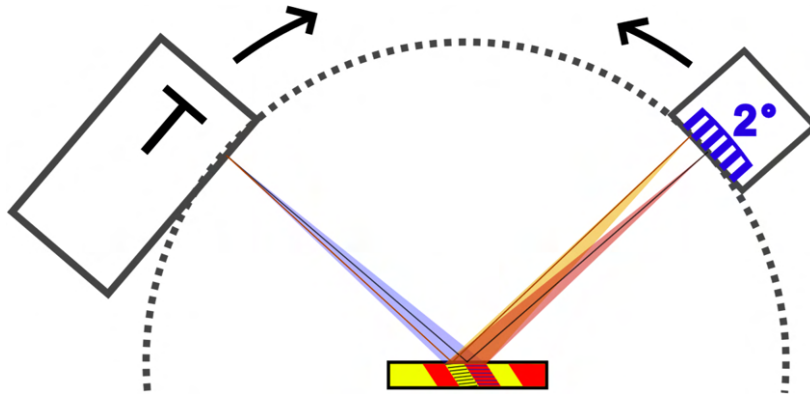


**Fig. 22:** Demonstration of advantage of divergent beam geometry with RTMS detector in case of twinned martensite. If the angular difference in orientation of “red” and “yellow” twinned martensite variants is within the beam divergence limit, both can be detected in 1D scan with this setup thanks to the 1D detector that scans the intensity over its full active range of approximately  $2^\circ$ .

Illustration is presented in **Fig. 23**. There, part (a) represents  $2D$   $2\theta$ - $\omega$  map of the twinned (400) and (040) reflections of 10M martensite of Ni-Mn-Ga measured in high-resolution parallel beam geometry employing a hybrid monochromator. The measurement took  $\sim 40$  minutes. In the map, the slight difference in orientation of both twinned variants is noticeable in the  $\omega$  direction, as well as the crystal mosaicity (the reflection spread into individual spots in the  $\omega$  direction). For thoroughness we need to clarify, that this can either be the true mosaicity, but also the effect of complex twinned microstructure. After alignment to the maximum of (040) peak, fast 1D scans were measured in both high-resolution parallel beam geometry and divergent beam geometry, **Fig. 23** (b) black and blue curve, respectively. Each scan took  $\sim 2$  minutes. Thanks to the beam divergence, both (400) and (040) reflections were reasonably well detected in case of divergent geometry as a sum of contributions from all the crystallographic domains.

In contrast, with higher-resolution setup employing hybrid monochromator, only the (040) reflection of the one selected domain is clearly dominant. This means that even though the detailed information on the particular crystallographic domain was gained, the overall information was lost in case of fast 1D scan.

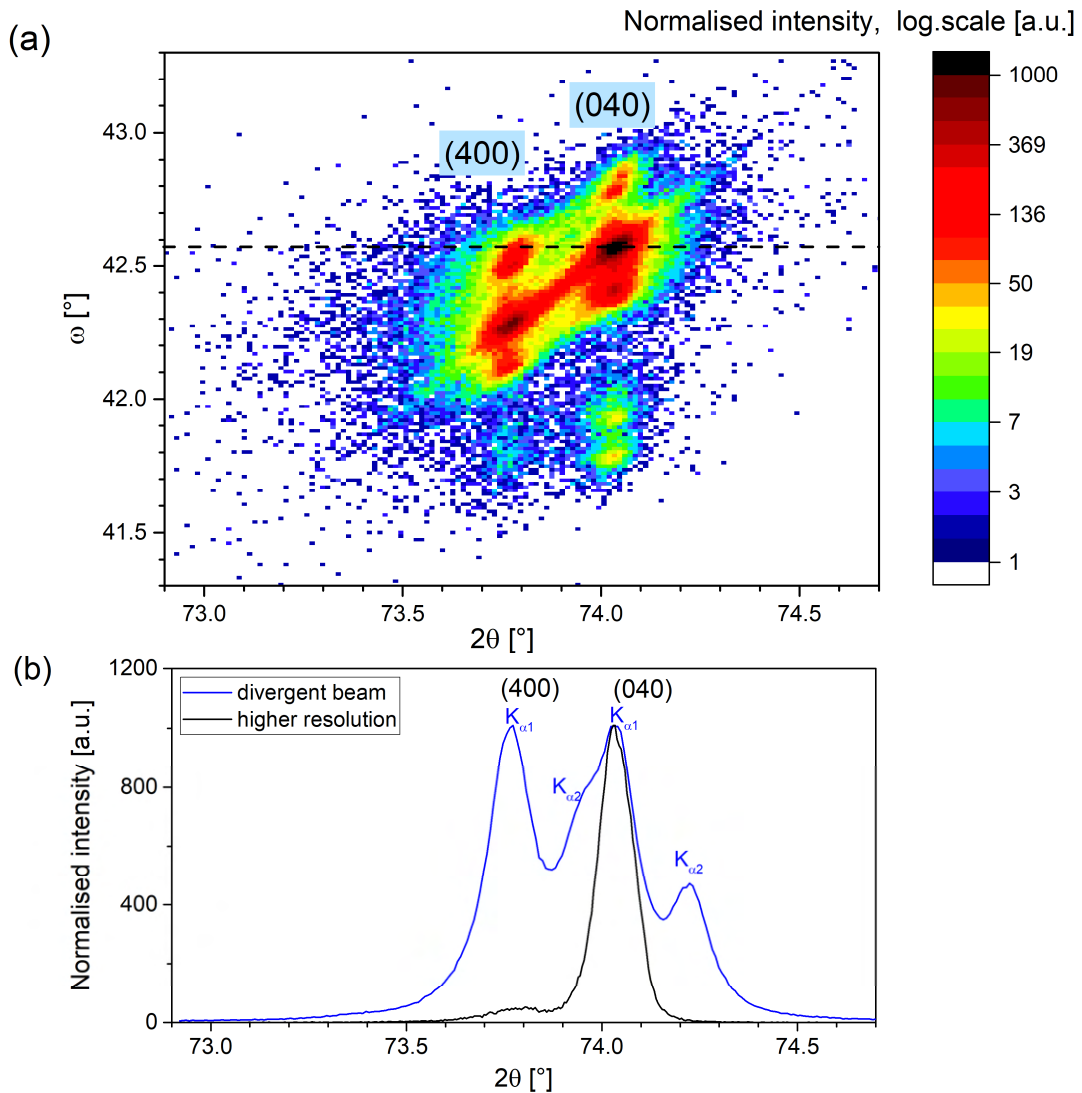


**Fig. 23:** (a) 2D  $2\theta_{\omega}$  map of (400) and (040) reflections measured with higher-resolution optics employing hybrid monochromator. Several crystallographic domains are well apparent in the  $\omega$  direction. (b) Fast 1D scans measured after alignment for the highest intensity of the (040) peak with divergent (blue) and higher-resolution optics employing hybrid monochromator (black, corresponding to the single line from the 2D map marked by black dash line) demonstrating the advantage of divergent geometry for fast analysis: both twinned domains with slight difference in orientation are detected in fast 1D scan.

The dedicated single-crystal, synchrotron or neutron diffractometers do operate with well-defined beam of negligible divergence. There, to get the full information on martensite variants and mosaic blocks, measurements require either adjustments of the crystal orientation for each variant or mosaic block, or time-consuming and/or data-heavy measurements of 2D maps that are more difficult to process than the fast 1D scans. Similar case represents also the use of parallel beam achieved by parabolic mirror in our multipurpose diffractometer – here the vertical divergence is almost negligible, providing the high sensitivity in the  $\omega$  angle. In contrast to this, the horizontal beam divergence from the parabolic mirror is relatively large but can be lowered by the aforementioned Soller slits.

Importantly for our measurements, great advantage of divergent beam geometry lies in the ability to perform different kinds of in-situ measurements. Typical example is the case of single crystal of 10M martensite, where both  $a$  and  $b$  lattice parameters can be quickly evaluated based on one fast 1D scan that takes as low as 20 seconds, allowing continuous tracking of these lattice parameters with temperature with fine steps ( $\sim 0.25$  K) in reasonable time [88]. This will be later demonstrated in chapter 4.5.

## 2.2.4 Neutron diffraction

The neutron diffraction experiments were carried out in *ILL Grenoble* using the following diffractometers:

- D9 hot neutron four-circle diffractometer with He cryostat. The used wavelength was  $\lambda_{D9} = 0.838$  Å.
- D10 single crystal four-circle diffractometer with He cryostat. The used wavelength was  $\lambda_{D10} = 2.360$  Å.
- CYCLOPS (CYlindrical CCD Laue Octagonal Photo Scintillator) neutron Laue single-crystal diffractometer with high flux on the sample from a continuous white neutron source. We used He cryostat for sample cooling/heating. Due to the high flux and fast total readout time ( $\sim 1$  s), this diffractometer was used in the search for the (inter)martensitic transformation(s). It was also used for confirmation of the sample orientation.
- Test instrument IN3: three-axis spectrometer on a through-going neutron guide suitable for sample orientation checking and q-scans measurements.

Given the broadness of the instrumentation, the details on the methodology and data interpretation for various tasks will be provided directly in chapters 3 and 4.

## 2.2.5 Diffraction data processing

We used PANalytical X'Pert Texture [89] for visualisation and processing of the measured pole figures and PANalytical Epitaxy [90] for visualisation and processing of the measured 2D reciprocal space maps. The final charts, maps and figures were drawn mostly in Origin [91].

The phase identification and powder diffraction data fitting was done using TOPAS [92], PANalytical HighScore [93] and employed the ICSD [94] and PDF-4 databases [95].

The neutron diffraction data collected in ILL Grenoble were processed using Rplot [96] and LAMP [97]. Neutron Laue images from CYCLOPS were processed with Esmeralda [98].

The majority of the diffraction profile fitting and peak analysis was performed in FitExc [99–101], see below.



## 2.2.6 FitExc – diffraction profile fitting program

The symmetric and asymmetric 1D  $2\theta$ - $\omega$  scans and q-scans were fitted in my custom-built diffraction profile fitting program FitExc, **Fig. 24**. [99–101] My aim in developing the program was to obtain the utmost precision and controllability of the fitting process. This side-project helped me significantly with the analyses of the shape memory alloys and thus it is included in my dissertation. The program allows for simultaneous fitting of multiple overlapped peaks, which is favourable for the complex twinned martensite structure. The controllability of the fitting process is excellent and thanks to advanced fitting approaches and possible parameter fixing, it can deal with overlapped reflections of up to several-order intensity difference.

Currently, the program consists of more than 10 000 lines of *Visual Basic for Application*-based code that controls the MS Excel processes and functions and adds new functionality. Furthermore, I created user-friendly interface that made my program accessible to other users. Currently, *FitExc* is being used for specific tasks in several laboratories across the globe.

*FitExc* was employed when processing the majority of the data discussed in chapters 3 and 4 and data from the fits were published, e.g., in references [57,88,102–107].

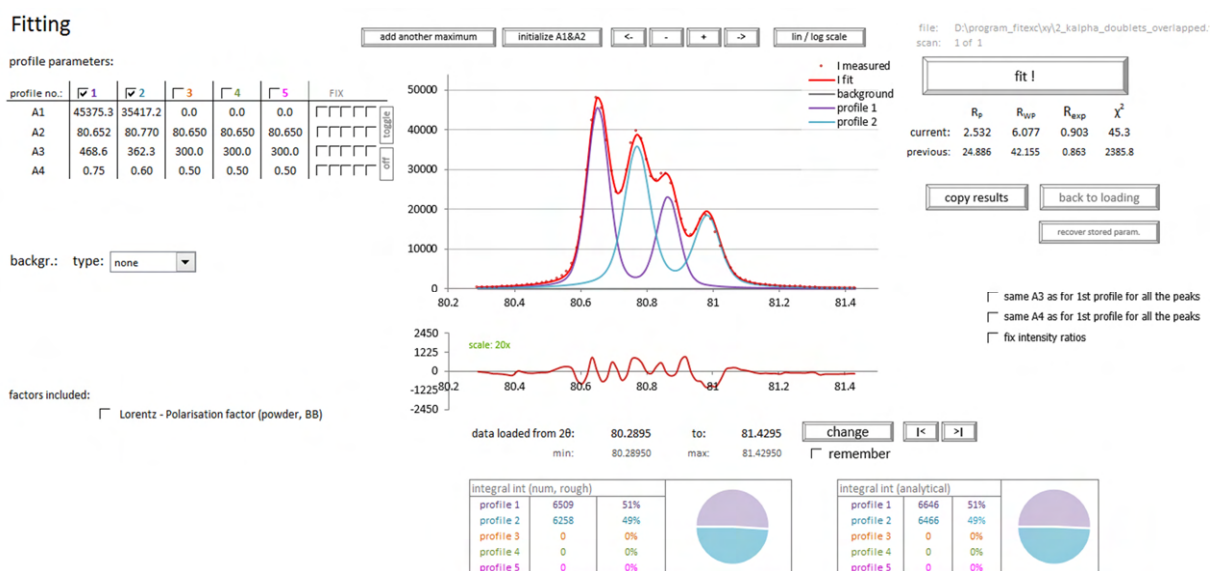


**Fig. 24:** FitExc interface – the fitting sheet. Fitting of two overlapped  $K_\alpha$  doublets for illustration.

## 2.3 Complementary experimental techniques

### 2.3.1 Magnetic measurements

AC magnetic susceptibility was measured using the system of three coils – the primary coil, producing the AC magnetic field ( $f = 486$  Hz,  $\mathbf{H} = 56$  A/m r.m.s.), and two identical secondary coils: one for reading the response of the sample and the second, wound in the opposite direction, for the background signal cancellation. The signal was detected by SR830 Lock-In amplifier.

DC magnetic susceptibility curve presented in the thesis for illustration were obtained in collaboration with M. Rameš (*FZU*). Measurements were done with the vibrating sample magnetometer (VSM) option of Quantum Design Physical Property Measurements System (PPMS).

### 2.3.2 Electrical resistivity measurements

The temperature dependence of electrical resistivity was measured in a Cryogenic cryostat with a closed cycle using a custom-built stage employing the AC four-probe method. It used a Stanford Research Systems SR830 DSP lock-in amplifier, a Pico Precision PP102 current source and a PP560 low noise amplifier.

### 2.3.3 Scanning electron microscopy

The scanning electron microscopy (SEM) micrographs shown in this thesis were taken in collaboration with L. Klimša at the *FZU* using TESCAN FERA3 GM iFIB-SEM equipped with a Peltier-element-based heating/cooling stage. Method based on back-scattered electrons (BSE) sensitive to different  $a/b$  twin variants due to channelling contrast was developed and used. [108]

### 2.3.4 Resonant ultrasound spectroscopy

Resonant ultrasound spectroscopy (RUS) measurements were performed by group of H. Seiner (Institute of Thermomechanics, CAS), using laser-based contactless modification of the standard RUS method.

### 2.3.5 Differential scanning calorimetry

The DSC curve shown for demonstration in the first chapter was measured by S. Sedláková using Linkam DSC6000 system equipped with the LNP95 cooling system.

### 3 Methodology of diffraction characterisation of martensites of Ni-Mn-Ga-based single-, poly- and oligocrystalline samples

In the MSM group, I focused on phase analyses, oriented the samples, determined lattice parameters, and/or texture (in case of polycrystalline or oligocrystalline samples), all depending on the actual needs. Complete list of analysed samples (of various forms, grain distributions etc) is listed in Appendix II. I began with the simple lattice parameter determination for large single crystals and quickly approached more complicated tasks – polycrystalline samples with strong texture, multiphase samples, heavily twinned single crystals etc. The main challenge represented the arc-melted samples that usually contained many large grains, where I had to employ and standardise the approach of oligocrystal characterisation described later in chapter 3.5.

Although being a routine task, the initial phase determination and lattice parameter calculation usually represents a crucial precursor for any future studies and development. In the following sub-chapters, I will provide an overview of the basic martensite characterisation possibilities I encountered, depending on the individual methods and sample state. I will present examples of results obtained during particular steps. Individual published results will then be addressed in chapter 4. For coherence, we will begin with the simplest characterisation of the single crystals (first employing the Laue method and then constant wavelength (CW) methods employing the multipurpose diffractometer), then we will discuss the rare case of ideal polycrystals, and, in the end, we will describe the possibilities of the basic characterisation of the oligocrystals representing the difficult region between the single crystals and polycrystals, typical case for arc-melted Ni-Mn-Ga-based Heusler alloys).

The aim is not only to present the individual results, but also to provide a brief guide to diffraction characterisation of similar alloys, especially when employing a multipurpose in-lab X-ray diffractometer. Here, established procedures have been missing in the field due to the non-standard nature of some of the tasks. Therefore, addressing the need, I present compilation of my characterisation methods as a part of my dissertation with hope to standardise the process for the future.

#### 3.1 Single-crystal Laue diffraction and sample orientation

Laue diffraction method which uses the continuous X-ray tube spectrum (also known as *die Bremsstrahlung*) still represents a valuable tool for crystal orientation and basic sample character determination (i.e., one can quickly recognize single crystal pattern, multiple grains, polycrystalline contribution etc). Regarding the Ni-Mn-Ga-based alloys, this method can be easily used especially for the cubic austenite. Nevertheless, it is known to struggle for twinned martensites, especially if hierarchical twin system is combined with structural modulation. Due to the heavy spots overlapping in twinned martensites, the use of this method is limited for characterisation of multivariant martensites. For these reasons, I used the Laue diffraction only occasionally for the aforementioned crystal orientation in austenite state and in case of simple NM martensite samples in single variant state.

Example of Laue diffractogram for a single-variant NM tetragonal martensite is presented in **Fig. 25** representing the final Laue pattern after sample orientation. The (001) orientation and the tetragonal symmetry is well-apparent. The misorientation from the true (001) direction was calculated to be  $< 1^\circ$ .

Unfortunately, as mentioned earlier, the reality is not always that kind for twinned martensites. To illustrate that, **Fig. 26** represents the case of heavily twinned 10M modulated monoclinic martensite. The evaluation of such a pattern is difficult due to the peak overlapping and worse signal-to-noise ratio due to the used imaging plate. Better resolution for distinguishing of the overlapped reflections could be obtained by larger sample to image plate distance (we used 30 mm) at the expense of lower amount of the detected spots and weaker signal. Greater improvement could probably be achieved with better detector (e.g., modern CCD-based panel). Nevertheless, our instrument did not have such an option.

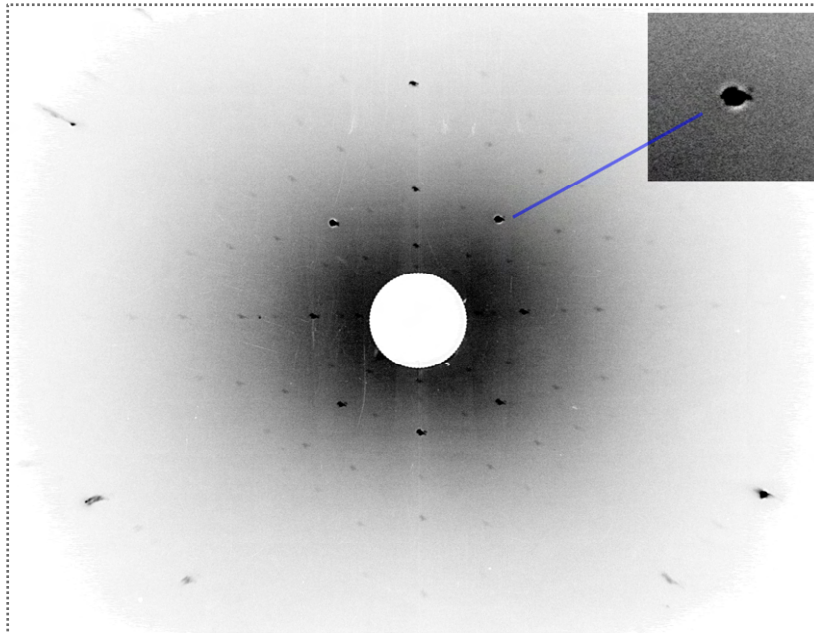


**Fig. 25:** Laue pattern of the (001) oriented  $\text{Ni}_{46}\text{Mn}_{24}\text{Ga}_{22}\text{Co}_4\text{Cu}_4$  single crystal. Non-modulated tetragonal martensite in single variant state. Four-fold symmetry axis is well apparent. Enlarged well-defined diffraction spot is shown in the inset for illustration.

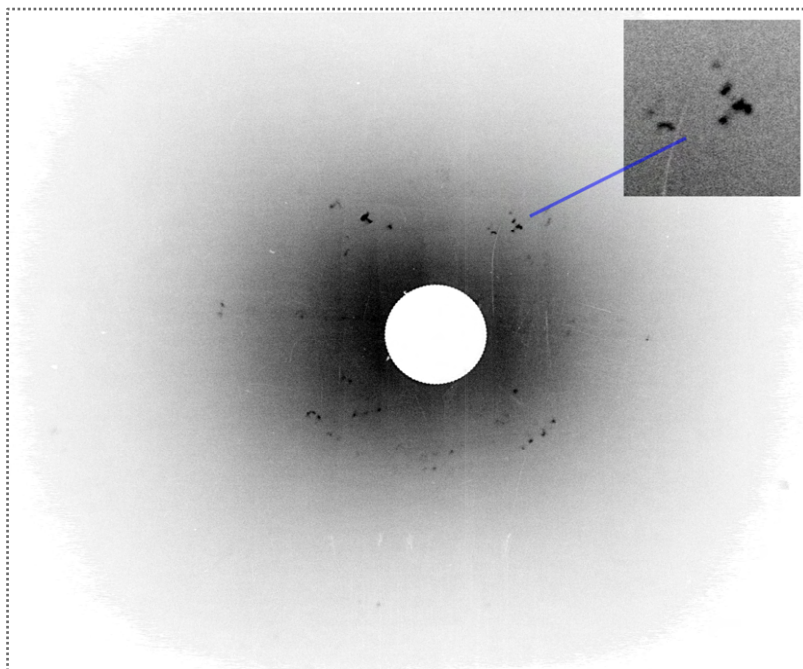


**Fig. 26:** Laue pattern of the  $\text{Ni}_{50}\text{Mn}_{28.5}\text{Ga}_{21.5}$  single crystal. 10M modulated martensite with possible contribution from another martensite phase. Peak asterism indicates complex twinned microstructure. Due to peak overlapping and worse dynamic range, further data analysis from such Lauegram is practically impossible. Enlarged region of multiple overlapped diffraction spots is shown in the inset for illustration.

To sum up, even though the X-ray Laue diffraction represents a valuable tool for sample orientation that is still present in the majority of the XRD laboratories, its use in our case of Ni-Mn-Ga-based martensites is quite limited with experimental setup that was available to me. Therefore, in the rest of the text, we will stick to the constant-wavelength (CW) X-ray diffraction experiments that usually led to desired information more quickly and relatively more easily.

But, in the contrary to the in-lab application of the X-ray Laue method, the neutron Laue method brought valuable results in our case. It's implementation in the instrument CYCLOPS in *ILL Grenoble* which was used for some of our measurements, deals with most of the disadvantages of our X-ray Laue thanks to larger irradiated sample volume, high neutron flux and, especially, the octagonal detector array surrounding the whole sample. Here, one can obtain almost the full image (including both transmission and reflection patterns). In our allocated experimental time, this method was used for initial temperature scans and determination of intermartensitic transformations.

Typical neutron Laue pattern for austenite of the  $\text{Ni}_{50}\text{Mn}_{27}\text{Ga}_{22}\text{Fe}_1$  single crystal with indexed reflections is presented in **Fig. 27** (a). Diffraction pattern changes noticeably after the transition to the 10M modulated martensite, **Fig. 27** (b). There, the changes in symmetry caused minor shifts of the diffraction spots, but, most importantly, also the appearance of the new satellite reflections in the  $[110]^*$  direction indicating the structural modulation.

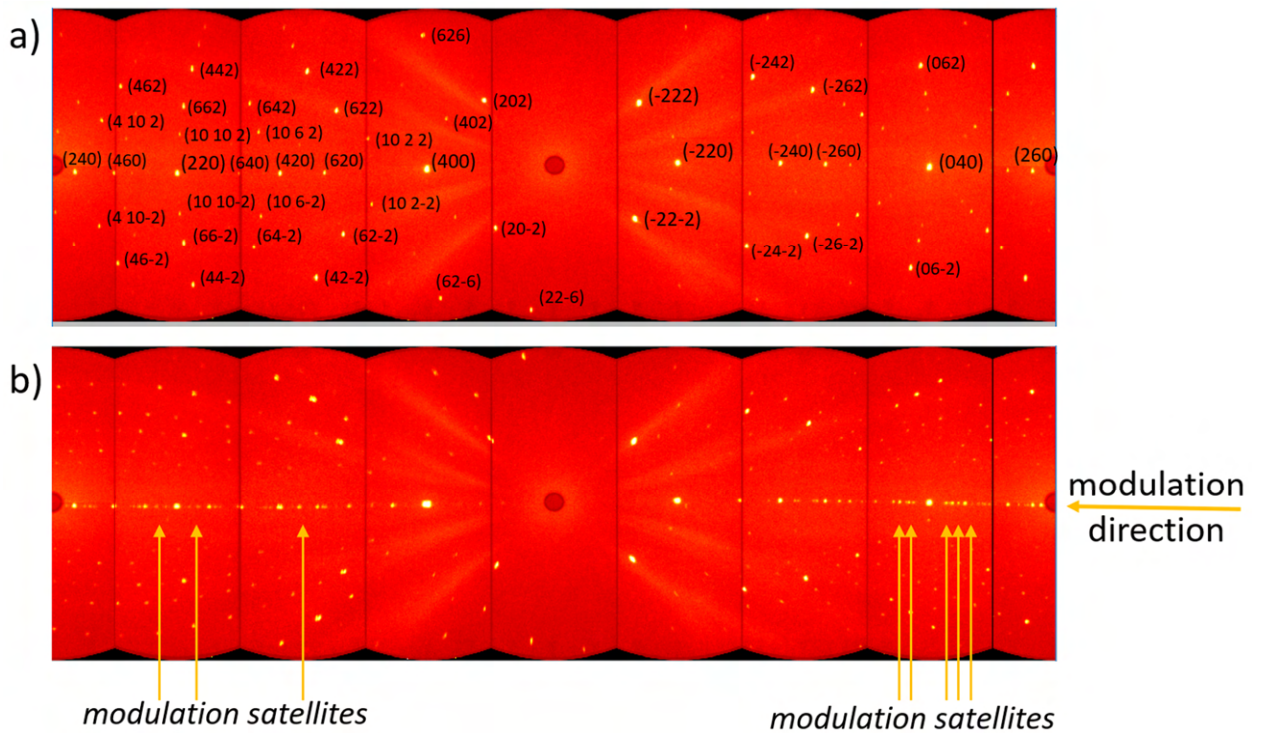


**Fig. 27:** Neutron Laue patterns of the of  $\text{Ni}_{50}\text{Mn}_{27}\text{Ga}_{22}\text{Fe}_1$  single crystal. a) Cubic austenite with indexed peaks. b) 10M modulated martensite with the modulation satellites visible in the  $[110]^*$  direction.

During our allocated experimental time, we ran such experiments with three selected alloys in small temperature steps (as small as 1 K in some of the cases). Our measurements served as one of the bases for the following CW measurements with higher resolution performed using the instrument D10 (results will be discussed later). Furthermore, obtained Lauegrams (Laue diffractograms) served as confirmation of successful martensite variant reorientation of 10M martensite sample prior to the follow-up measurements (e.g., when we applied mechanical stress to remove the *c*-oriented variant).

Although our CYCLOPS results were not yet published on their own, they served as important pre-experiments for the studies described later in sub-chapter 4.5 and published in [107,109].

## 3.2 XRD characterisation of Ni-Mn-Ga-based single crystals employing the multipurpose X-ray diffractometer

Now, we will move to the constant-wavelength (CW) diffraction experiments and we will continue with the simplest sample form - the single crystals. During my work, I analysed large number of single-crystal samples in various martensite states. Complete list of analysed samples is presented in Appendix II. In this chapter, the basic methods of the single-crystal characterisation employed in the MSM group at the *FZU* will be described. The more advanced studies will be described later in the chapter 4.

Dictated by the necessity of the characterisation of the large single crystals, different scales of the twinned microstructure, and considering the notable advantages of the divergent beam, the multipurpose diffractometers (often referred as powder diffractometer) were employed in all our CW XRD studies instead of the dedicated single crystal diffractometer. Nevertheless, we are fully aware of the possibilities, pros and cons of crystal characterisation and structure determination employing a dedicated single crystal diffractometer that is usually equipped with kappa goniometer. Although our choice of instrument does not represent a tool for an automated XRD data collection from single crystals and complete structure solution, it is perfectly capable of dealing with the partial tasks, sometimes with notable advantages for our applied research.

### 3.2.1 Phase identification and the unit cell determination

The initial step represents the phase identification or its confirmation (when the prediction based on various methods, such as magnetic measurements or microscopy, is available). Every phase is characterised by its unique typical diffraction pattern. In practice, we can restrict ourselves to matching of our obtained diffraction patterns to single or multiple known phases expected in our range of stoichiometries of the Ni-Mn-Ga-based alloys since their amount is very limited (see chapter 1.5). **Fig. 28** represents a simulation of powder XRD patterns of the most common Ni-Mn-Ga phases for the Co radiation. Here, the powder patterns are shown as a standard and relatively easily approachable representation of the diffraction pattern that transforms the 3D data of the single crystal into 1D. In all the cases, pseudo-austenitic coordinates for the indexing of the peaks of martensite phases were used. This allows direct correlation of our results with other measurements and observations.

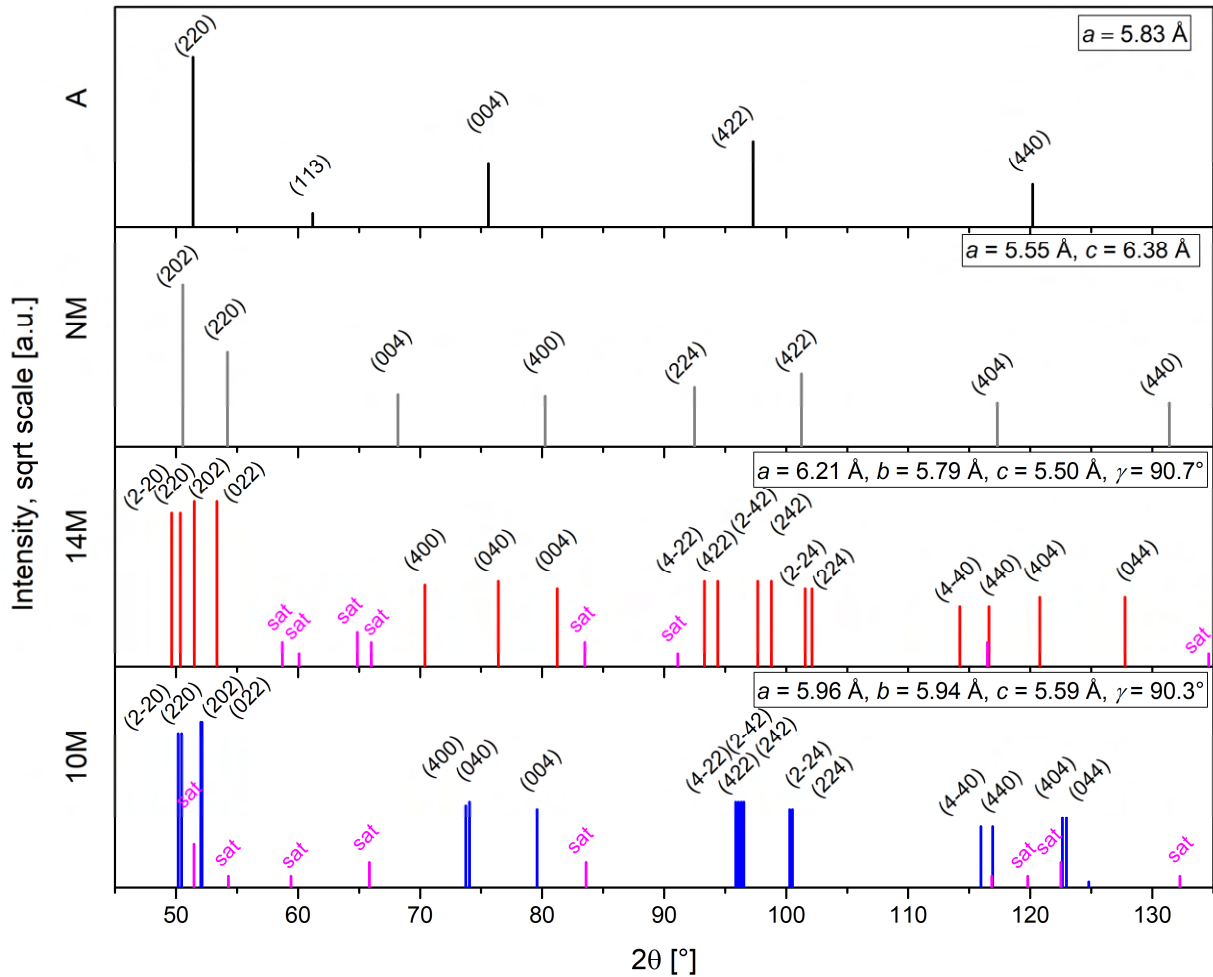


**Fig. 28:** Simulated powder patterns calculated for the most common phases of Ni-Mn-Ga-based alloys. For clarity, peaks are represented as single vertical lines, their lengths are equal to intensities (calculated from the structure factors) plotted in sqrt scale for accentuation of low-intensity reflections. Strong satellite peaks of the modulated phases are marked with magenta. Indices of martensite phases use the pseudo-cubic coordinates. Bragg angles correspond to the Co radiation ( $K_{\alpha 1} = 1.78901 \text{ \AA}$ ), the chosen  $2\theta$  interval of  $45\text{-}135^\circ$  represents an interval where the strong reflections appear.

Using the dedicated single-crystal diffractometer, one would be able to measure the whole (reachable) reciprocal space at once and collect multiple reflections in one go. Even though automated reciprocal space scanning becomes slowly available even in multipurpose diffractometers, machines that I used unfortunately did not offer such functionality. Furthermore, such measurements would require long data acquisition time for basic tasks such as simple unit cell determination in our case of limited amount of the probable phases.

Therefore, the data collection was performed using different approach – by initial inquiry on the presence of the typical strong reflections and their orientation and by measurements of several pole figures for expected  $2\theta$  Bragg angles (based on the reflections of the expected phases from **Fig. 28**) and then by measurements of higher resolution  $2\theta$ - $\omega$  scans at selected  $(\chi, \varphi)$  angles for individual reflections to obtain precise  $2\theta$  values for the lattice parameters calculation.

Explicitly, our standard procedure for the Ni-Mn-Ga single crystal of unknown phase looked as follows:

1. **Pole figures:** First, set of pole figures at expected  $2\theta$  angles for the strong principal reflections of martensite phases and austenite (especially the  $\{400\}$  and  $\{220\}$  fundamental reflections) were measured, **Fig. 29** (showing only the pole figures where reflections were found). The measurement was done with larger detector acceptance angle, i.e., the detector collected the intensity in the  $2^\circ$  interval around the desired  $2\theta$ . Results presented here indicated the 10M martensite and excluded presence of other phases (i.e., no intensity was detected at the  $2\theta$  angles corresponding to other phases, not shown).

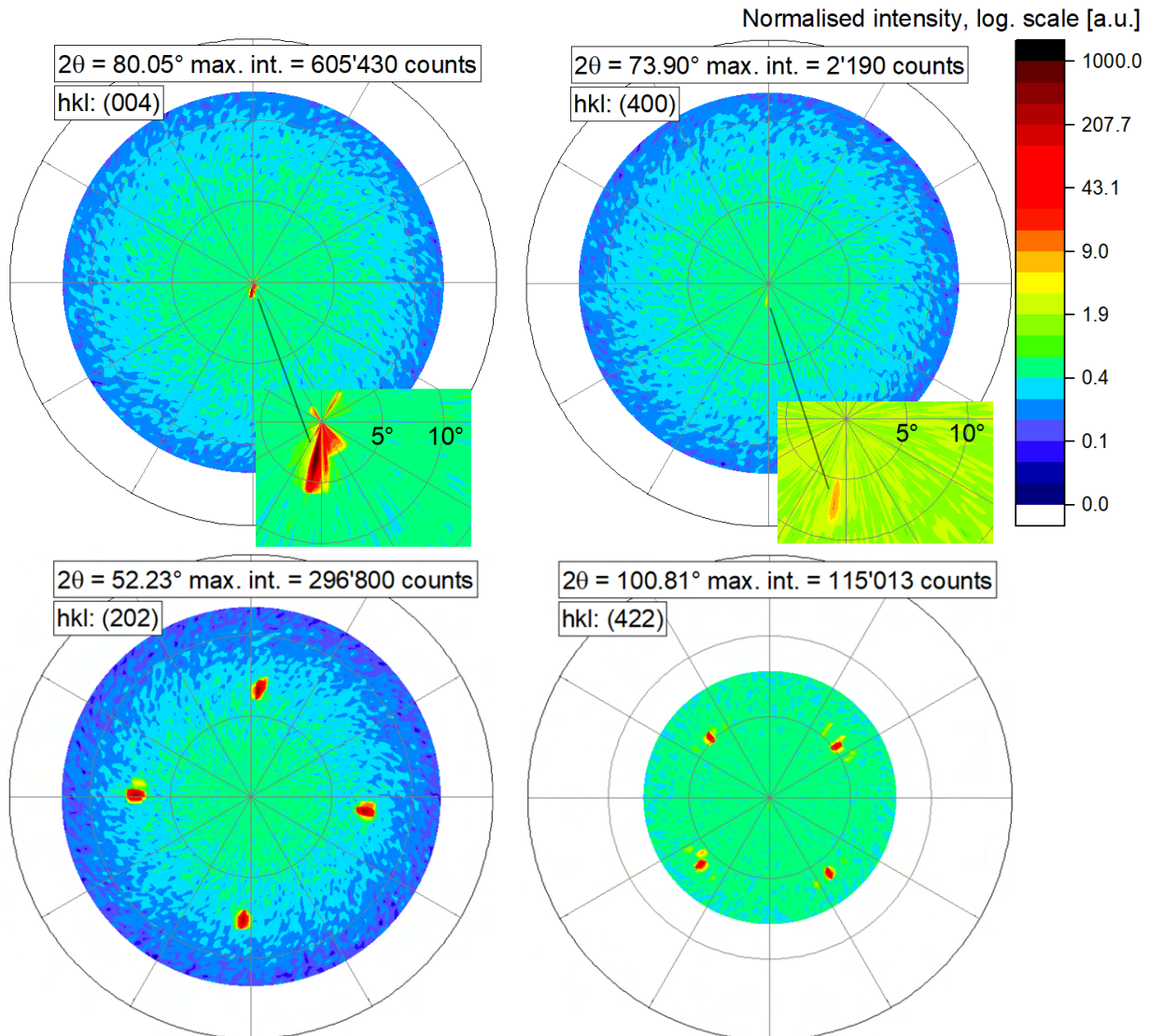


**Fig. 29:** Typical pole figures for relatively well oriented single crystal of  $\text{Ni}_{50}\text{Mn}_{28}\text{Ga}_{22}$  - 10M martensite phase. Low-intensity (400) and (040) reflections are detected at orientation close to (004) due to twinning, c-oriented martensite variant is clearly dominant in this set of measurements. All the pole figures use the same intensity scale normalised to the global maximum of intensity.

2. **Orientation refinement:** If any reflections were detected in the pole figures, manual alignment followed around the suggested  $(\chi, \varphi)$  coordinates by manual  $\chi$ ,  $\varphi$ , and (if necessary)  $\omega$  scans and more precise  $2\theta$  scans, to refine the orientation of the peak. The orientation refinement was done repeatedly to achieve desired precision. For this step, optics were usually changed from divergent to parallel to obtain better precision.
3.  **$2\theta$ - $\omega$  scans:** For every such orientation,  $2\theta$ - $\omega$  scan containing individual reflection (sometimes overlapped reflections from twinned variants) was measured. If better precision was needed or



in case of crystal with strong mosaicity (later discussed in chapter 3.5), smaller reciprocal space maps (usually  $2\theta$ - $\omega$ - $\omega_{\text{offset}}$  maps) were measured to obtain more insight.

4. **Peak fitting, Bragg angle evaluation:** Measured scans were fitted with the FitExc program to obtain the  $2\theta$  maxima. This advanced fitting was necessary because of the frequent presence of the overlapped peaks due to twinning. It also dealt with the possible peak asymmetry due to higher tilt angles etc.
5. **Lattice parameters calculation:** Following previous points, as many reflections as possible or necessary (usually  $\sim 10$ , depending on the previous knowledge about the sample) were collected. Then, peaks were manually indexed with the pseudo-austenitic cell following the marking shown in **Fig. 28** and least-squares method was used to calculate the precise lattice parameters from all the reflections simultaneously.

Example of the measured reflections for the 10M martensite of  $\text{Ni}_{50}\text{Mn}_{28}\text{Ga}_{22}$  at room temperature is shown in **Table 2**. The lattice parameters were calculated as:  $a = 5.961 \text{ \AA}$ ,  $b = 5.943 \text{ \AA}$ ,  $c = 5.601 \text{ \AA}$ ,  $\gamma = 90.32^\circ$ . From the maximum difference between the measured and calculated  $2\theta$  positions, the precision was determined as  $0.001 \text{ \AA}$  and  $0.01^\circ$ .

**Table 2:** Reflections measured for the  $\text{Ni}_{50}\text{Mn}_{28}\text{Ga}_{22}$  sample

$h$	$k$	$l$	$2\theta$ calculated	$2\theta$ measured	difference
6	0	0	128.435	128.422	0.012
0	6	0	129.131	129.142	-0.011
0	0	6	146.769	146.773	-0.004
4	0	0	73.783	73.768	0.015
0	4	0	74.034	74.034	0.000
0	0	4	79.409	79.406	0.004
4	4	0	116.981	116.973	0.008
6	2	0	143.987	144.005	-0.018
2	6	0	144.816	144.811	0.005
0	4	4	122.761	122.754	0.007
-4	4	0	115.951	115.958	-0.007
6	0	2	145.657	145.653	0.004
0	6	2	146.631	146.628	0.003

In some cases, the analysis is noticeably simplified by the previous expectation of the particular single martensite phase (e.g. based on magnetic measurements, information from the producer or based on the stoichiometry). Nevertheless, in case of totally unknown state of the sample, large amount of pole figures is needed to exclude possible simultaneous presence of other expected or even unexpected phases and to investigate possible presence of multiple grains. This makes the analysis quite long (i.e., approximately 1-2 days for one sample). Further details on characterisation of multigrain samples are discussed in sub-chapter 3.5.

### 3.2.2 Reciprocal space mapping and the study of modulation

After the crystallographic unit cell and the sample orientation were determined, the reciprocal space mapping is possible, example of the part of reciprocal space map is shown in **Fig. 30**. Usually, the reciprocal maps in the direction of modulation are measured in order to collect the satellite reflections. Based on these, the modulated martensite phases can unambiguously be confirmed and analysed. Noteworthy, reciprocal space maps can bring additional information on twinning, i.e., when the modulation twins are involved, modulation satellites of 10M and 14M phases appear in both  $(110)^*$  and  $(-110)^*$  directions. Alternatively, the single q-scans (one dimensional scans of the reciprocal space, usually in the direction of modulation, **Fig. 31**) can be measured (if implemented in the data collection software) in case of simple 1D modulation.

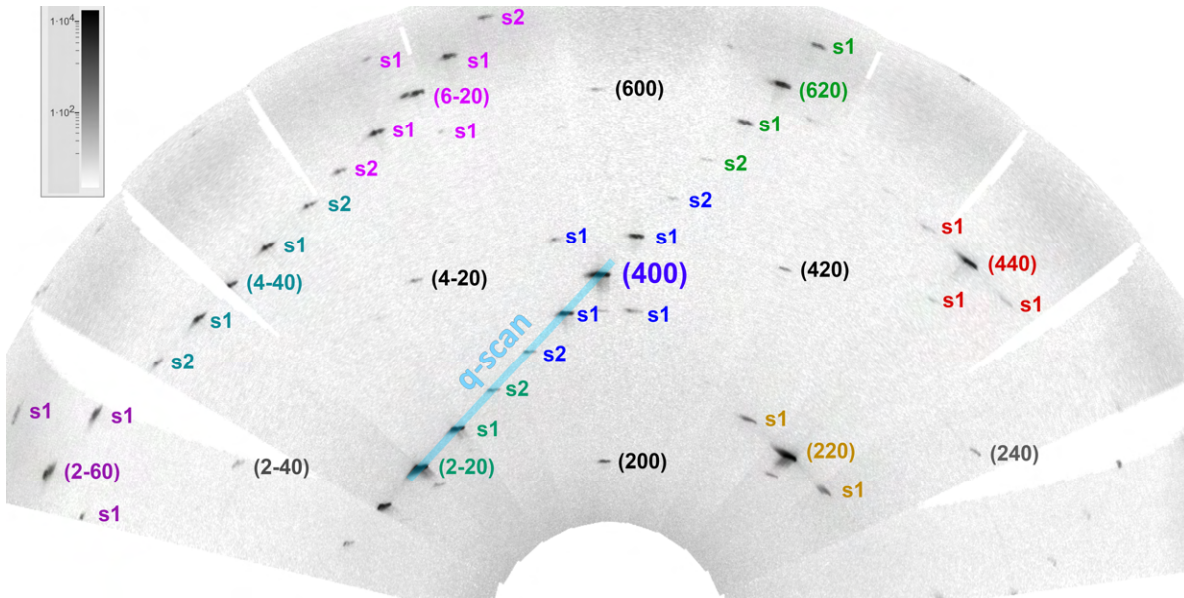


**Fig. 30:** Example of the part of the RSM measured for the 10M martensite of  $\text{Ni}_{50}\text{Mn}_{28}\text{Ga}_{22}$ . Azure line illustrates a q-scan in the  $(110)^*$  direction, see Fig. 31. Due to the modulation twins, both  $(110)^*$  and  $(-110)^*$  directions exhibit modulation satellites.

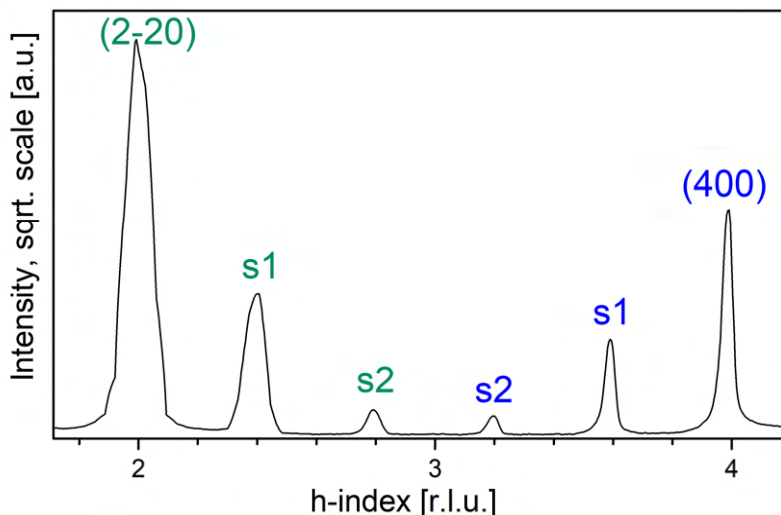


**Fig. 31:** The q-scan corresponding to the azure line from **Fig. 30**.

The approach of measuring q-scans instead of full reciprocal space maps has the advantage of diminishing the necessary measuring time considerably compared to the full reciprocal space maps. Nevertheless, this is only possible after the initial RSM measurements confirming the modulation direction.

### 3.2.3 Martensite variants distribution

From the pole figure measurements, one can naturally gain the insight on the twin variants distribution and their orientation in the single crystal. Illustration for the NM martensite can be seen in **Fig. 32** and **Fig. 33**. Both pole figures were measured with the same sample of the same orientation. **Fig. 32** indicates major presence of the *a*-oriented variant in the measured direction. Nevertheless, some minor contribution from the *c*-oriented variants can be clearly detected, **Fig. 33**. The difference in the  $(\chi, \varphi)$  orientation of the variants is given by the nature of the *a/c* twinning, orientation of the three present crystallographic domains is illustrated in **Fig. 34**. From the intensities, the variant distribution can be roughly estimated: 96.4 % of the intensity comes from the *a*-oriented variant, 3.6 % of intensity come from both the *c*-oriented variants.

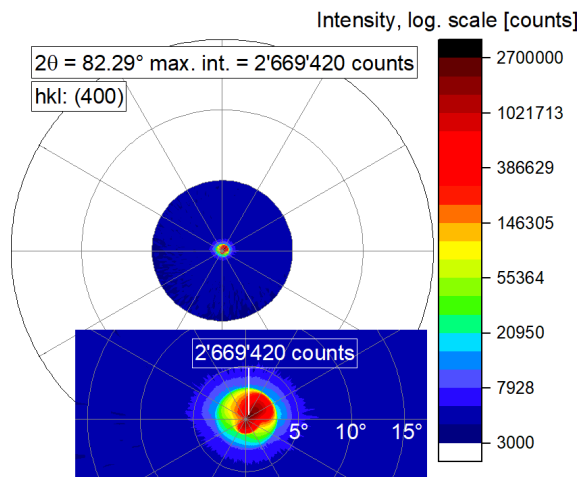


**Fig. 32:** Pole figure of the (400) reflection of the Ni-Mn-Ga NM martensite clearly indicating the *a*-axis perpendicular to the sample surface.

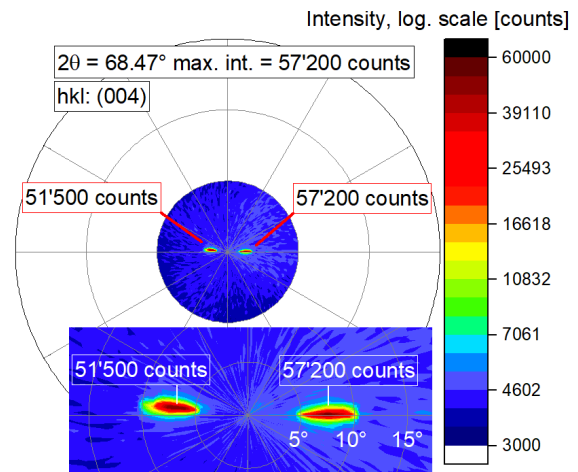


**Fig. 33:** Pole figure of the (004) reflection of the Ni-Mn-Ga NM martensite indicating two *c*-oriented twins present in the sample due to the *a/c* twinning.

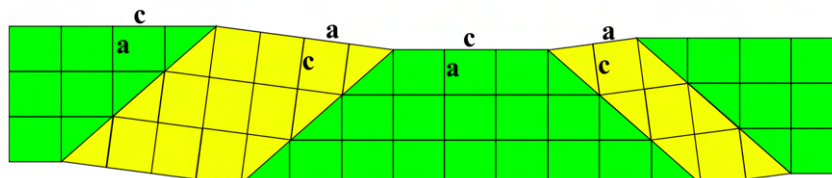


**Fig. 34:** Illustration of the orientation of the twin domains suggested by the pole figures. According to the intensities, the *a*-oriented variant (green) is strongly dominant in the sample. The real microstructure is more complex and usually contains large number of *a*- and *c*-oriented parts.

Similar experiments represent a valuable proof of the twin variant reorientation which is needed for some of the experiments and is usually achieved with strong magnetic field or mechanical stress. Nevertheless, one should always bear in mind the smaller penetration depth ( $\sim$  tens of  $\mu\text{m}$ , depending on the source) of conventional XRD. For full volume, neutron measurements are needed.

Good example of fast analysis allowed by the divergent beam (see chapter 2.2.3) represents the case of 10M martensite. Here, due to very small difference between the *a* and *b* lattice parameters and the  $\gamma$  angle very close to  $90^\circ$ , usually the *a*- and *b*- oriented variants can be present in one single  $2\theta$ - $\omega$  scan consisting of overlapped (400) and (040) reflections when the divergent geometry is used, **Fig. 35**. Therefore, from this fast single scan (and keeping in mind the structural factor) distribution ratio of

*a*- and *b*-oriented variants can be evaluated fast. Here, for illustration, the ratio of integral intensities of the (400) and (040) reflections was determined as 43% : 57% with FitExc. The *c*-oriented variant was not detected in wider  $2\theta$ - $\omega$  scan, confirming the full martensite reorientation with magnetic field (in the particular analysed volume).

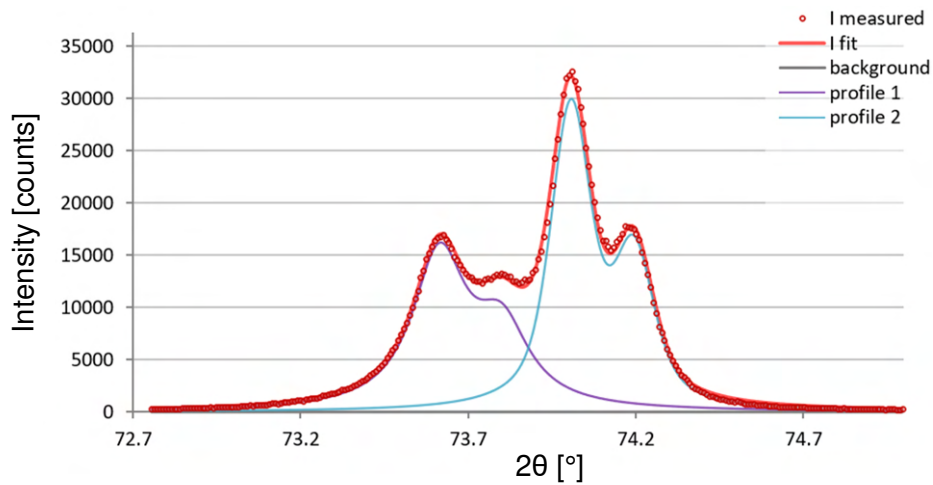


**Fig. 35:** Overlapped (400) and (040) reflections of the 10M martensite of the  $\text{Ni}_{50.0}\text{Mn}_{28.7}\text{Ga}_{21.3}$  single crystal detected in a single  $2\theta$ - $\omega$  scan and fitted with FitExc. Integral intensities of the individual peaks were calculated as  $I_{400} = 6731$  counts,  $I_{040} = 8778$  counts, giving the intensity ratios of 43:57.

Reciprocal space mapping can bring more information on the orientation of the twinned microstructure. This is a valuable tool to recognise the orientation of the *a/b* twin laminate of the 10M martensite, **Fig. 36**, which usually cannot be distinguished easily with other common methods, such as optical microscopy with Nomarski contrast (DIC), due to the very small angle between the *a*- and *b*-oriented variants. This angle can be easily calculated as  $90^\circ - 2 \arctg(b/a)$ , giving the value of  $\sim 0.15^\circ$ . [110]

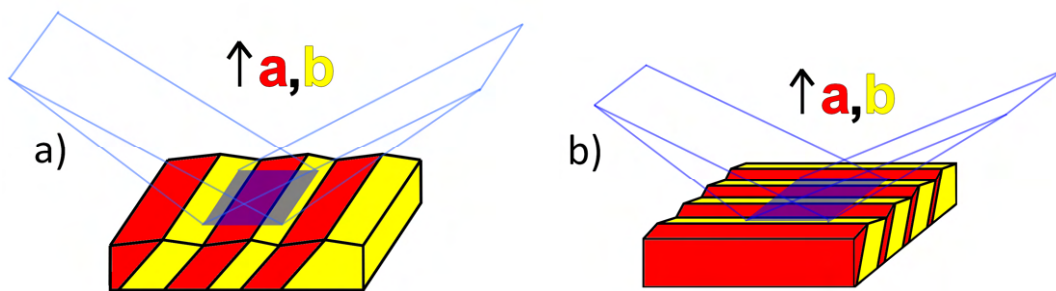


**Fig. 36:** Schematic depiction of *a/b* laminate of 10M martensite in two cases: a) *a/b* boundary perpendicular to the plane of the goniometer, b) *a/b* boundary parallel to the plane of goniometer. The angular difference between the orientations of the *a*- and *b*-oriented twin domains is exaggerated for illustration, the real difference is  $\sim 0.15^\circ$ .

When such a sample is examined under XRD, two contrasting reciprocal space maps can be obtained (depending on the resolution). When the *a/b* twin boundary is perpendicular to the plane of the goniometer, **Fig. 36 a)**, the (400) and (040) reflections in the reciprocal space maps are detected at different  $\omega_{\text{offset}}$  angles, **Fig. 37 a)**. In case of *a/b* twin boundaries parallel to the goniometer, **Fig. 36 b)**, both reflections are detected at the same  $\omega_{\text{offset}}$  angle, **Fig. 37 b)**. [110]

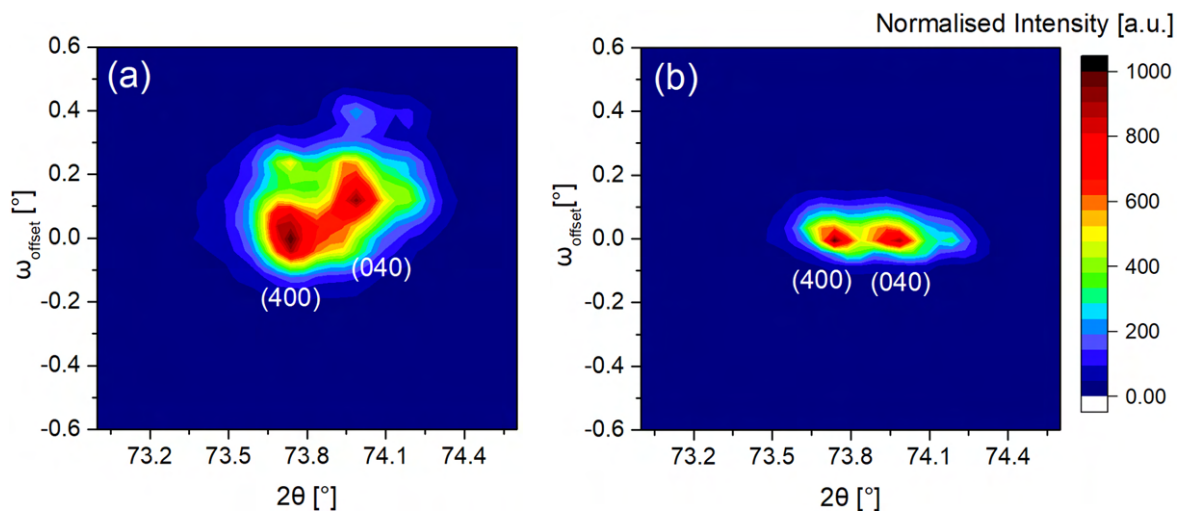


**Fig. 37:** Reciprocal space maps of (400) and (040) peaks in the instrumental coordinates. a) The *ab* twin boundary is perpendicular to the plane of the goniometer - the peaks appear at different  $\omega$  angles. b) The *ab* twin boundary is parallel to the plane of the goniometer – both peaks appear at the same  $\omega$ . Adapted from [110].

### 3.3. ND studies of the modulation and processing of q-scans

In the later discussed neutron experiments, we studied the evolution of the structural modulation with temperature. The base of the method is very similar to the one described above, therefore only some specific aspects are described here.

In our ND measurements at the *ILL Grenoble* [111,112], mainly the four-circle diffractometers with He cryostats were used to analyse the q-scans in the [110]\* direction (explained in the previous chapter).

Prior the ND measurements, our samples were oriented and analysed by the XRD, following the procedures described in chapter 3.2. Therefore, the lattice parameters of our crystal, direction of modulation etc., were already known.

At the *ILL*, mechanical compression was used to diminish the contribution of the *c*-oriented variant in the measured scans and the samples were aligned in the goniometer based on the set of selected strong fundamental reflections, specifically (4 0 0), (8 0 0), (2 2 0), (0 2 2), (2 0 2), (6 2 0), (8 4 0), (0 4 8), (4 8 0), and superstructural reflections (3 1 1), (1 1 1), (5 3 3), (2 0 0), (0 2 0) and (0 0 2). The UB orientation matrix was determined at room temperature before enclosing the sample into cryostat. The entire automated process was carefully supervised to prevent the errors caused by contributions from the twinned variants.

The cryostats of D9 and D10 instruments allowed us to track the modulation changes while cooling down to 10 K and heating to approx. 320 K. Expectably, the sample orientation slightly changes with temperature due to the thermal expansion/compression and, more importantly, the intermartensitic transitions (newly created martensite variants change the shape of the sample). Ideally, one should refine the sample orientation (the UB matrix) based on the set of preselected reflections at every temperature step. We indeed adjusted sample orientation at every step during our XRD experiments. Unfortunately, due to time limitations and necessity to supervise the process (due to inevitable twinning that might send the algorithm toward wrong solution), this was not possible at every temperature step of our ND measurements. Additionally, we needed to cope with the aforementioned twinning of martensite, i.e., we needed to exclude the unwanted differently oriented martensite variants from the q-scans.

To cope with this problem, our measurements employed the 2D detector and specific data processing according to the following procedure:

- The q-scans were not recorded purely as 1D scans. In fact, each step in the q-scan contained the full 2D image from the detector, **Fig. 38**.
- For each such a scan, the appropriate area of the detector was chosen for the intensity integration. With this, we got rid of the problem of possible minor misorientation, problem of contributions from the multiple variants, and we generally increased the signal-to-noise ratio, see **Fig. 39** and **Fig. 40** for demonstration.

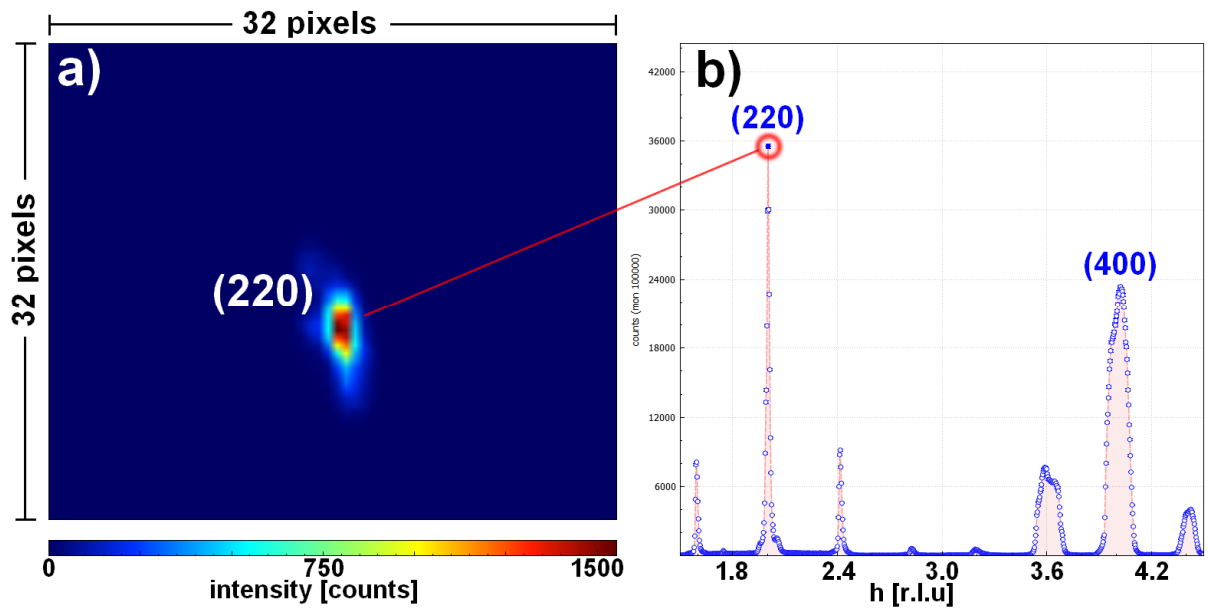


**Fig. 38:** Adapted screenshot from Rplot [96] containing two parts: a) Image from the detector containing the pixel range for the intensity integration and b) the resulting q-scan. The presented detector image corresponds to the (220) peak. The q-scan contains the intensity from the full detector area of 32×32 pixels integrated at each step along the “q-line”. Such a result is clearly obscured, as combined contributions from multiple peaks are integrated at some steps (see further). It is also visible that the sample is not perfectly aligned at this temperature, since the reflection is slightly off-centre.

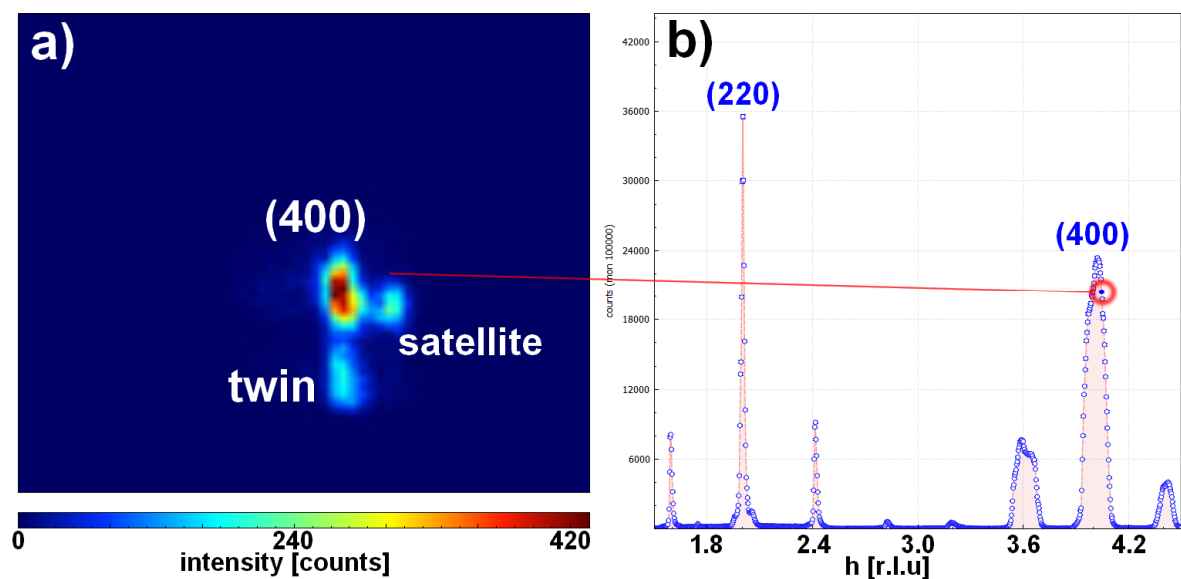


**Fig. 39:** Screenshot from Rplot [96] containing two parts: a) Image from the detector containing the pixel range for the intensity integration and b) the q-scan. Now, the focus is given on the particular point close to the (400) peak in the q-scan. The detector image indeed reveals that multiple peaks contribute to the integrated intensity: the (400) reflection, parasite reflection from twin variant and satellite reflection that appears in the detector area due to geometry reasons. This suggests that the detector area used for data integration needs to be reduced.

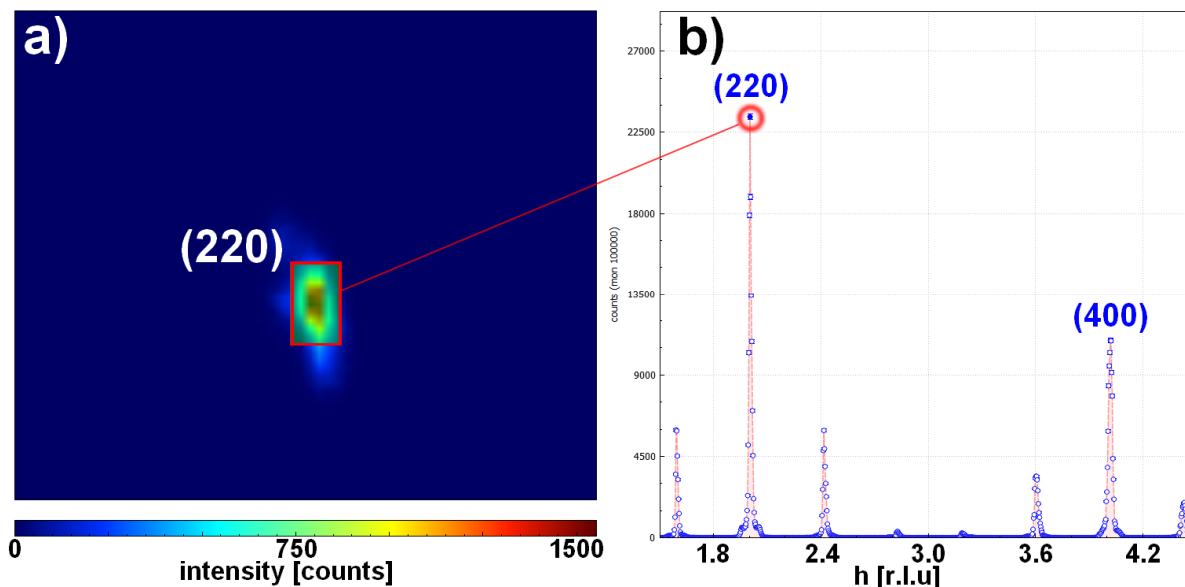


**Fig. 40:** After selection of the appropriate integration area (used area is highlighted light green, the full detector range is shown here just for context) chosen empirically based on the 2D detector images along the whole measured “q-line”, resulting q-scan is clear and reveals minor satellite peaks that appear close to the main reflections (later demonstrated in log. scale in **Fig. 71** and others). Now, the q-scan is ready to be fitted.

This procedure could not have been automated due to the different nature of every sample (different mixture of variants present, different crystal mosaicity etc.) and different transformation temperatures. Therefore, I processed more than 100 such scans manually and chose the appropriate integration area. To obtain coherent results for all the temperatures, described procedure was performed in several iterations while comparing the resulting 1D q-scans to each other and making sure that the overall intensity has not decreased too much, noise is not gained and/or new peaks from random variants are introduced. With this, the later-presented final 1D q-scans were obtained.

For every q-scan, every peak was fitted with pseudo-Voigt function which showed the best agreement with the character of the peaks. Given the peak overlapping and up to three orders intensity difference of some satellites compared to the main reflections, this procedure was also done manually, employing FitExc. With this, set of reflections (main and satellites) present in q-scan was obtained, together with their positions and integral intensities. Then the indexing was performed and modulation vector has been determined.

Altogether, for illustration, behind every point in the presented later in the final  $q(T)$  charts (later shown **Fig. 74** etc.), there were tens of minutes of intense experimental work and elaborate data processing.



### 3.4 XRD characterisation of the Ni-Mn-Ga bulk polycrystals and powders

The diffraction pattern of a polycrystal (usually referred to as *powder diffraction pattern*) represents a one-dimensional snapshot of the reciprocal space, where the scattered intensity is measured as a function of a single independent variable – the Bragg angle  $2\theta$ . The powder diffraction pattern includes large amount of additional information (e.g. on texture of the sample, crystallite size, etc.) and, when properly collected and processed, a great deal of detail on about a material can be established. [113]

The advantage of the powder XRD when it comes to our materials lies in the fact, that the contribution from all possibly twinned martensite variants is gathered in one scan. Therefore, the complicated separation of the contributions from the particular twinned domains which must be employed for the structure solution from twinned single crystals is not needed here. The powder pattern also carries the information on structural modulation. Nevertheless, the method has many practical disadvantages when it comes to studies of our martensites.

#### 3.4.1 Limits

The full 3D (or even 4D in case of modulation) information is collapsed onto 1D. Therefore, the structure solution from the powder data is difficult, results might not be singular and good initial model is needed. When it comes to the modulated phases, the high-order modulation satellites of low intensity might get overlooked as they might be immersed in the background.

There is also a problem of sample preparation: obtaining an ideal polycrystalline sample with random grain distribution and small particle size ( $<50\ \mu\text{m}$ ) is not simple. In practice, the bulk polycrystalline samples produced by conventional methods (such as arc melting) are often highly textured and contain large grains complicating the analysis. The attempts to produce powder samples (by milling etc.) often result in influenced microstructure and large residual stresses. [113]

And last, but perhaps most importantly, the MIR functionality of our materials is manifested mainly in single crystals and the results obtained from powders might be of limited practical use given the possibly influenced structure and microstructure. This was earlier addressed in chapter 1.7.

In some cases, PND can be used with advantage – due to larger irradiated sample volume, the requirement of large amount of randomly oriented grains can be fulfilled more easily. Nevertheless, there are only several neutron sources with small-enough instrumental broadening suitable for studies of overlapped reflections of some of the Ni-Mn-Ga martensites.

#### 3.4.2 Powder pattern analysis and Rietveld refinement

When it comes to sample characterisation practice, if we forget about the aforementioned limits, there are multiple methods to approach the measured powder samples consisting of the known martensite phases. The most used is the Rietveld refinement, where all the structural and instrumental parameters are refined by fitting a calculated profile to the observed data [113–115]. After the initial qualitative phase analysis, the determination of lattice parameters, texture, microstrains, crystallite size and (in the presence of multiple phases) quantitative phase analysis can be done by Rietveld refinement. In case of more complex texture or cases without the known structural model, structure-less hkl fitting (i.e. Pawley or LeBail fitting, where peak intensities are free parameters to some level) can be employed to gain at least some part of the information (such as lattice parameters) in several software suites, such as TOPAS [92]. The use of the hkl fitting is unfortunately limited for modulated martensites and other low-symmetry phases given the large number of reflections and resulting peak overlapping.

Furthermore, for Rietveld refinement, a reasonable initial model is needed. When it comes to the Ni-Mn-Ga-based alloys, the structure databases contain several inconsistent entries, especially when it comes to modulated martensites.

Despite my experience with the Rietveld refinement performed on various Zn-, Mg-, and Ti-based materials and their difficult corrosion products, see e.g. [116–121], and further experience with Ni-Ti-based alloys and Fe-Cr-Ni-Ti-Mn high-entropy alloys, I have unfortunately never encountered refinable Ni-Mn-Ga powder sample. The structure was always broken by pulverisation and did not correspond to the original bulk.

Typical case of the samples I encountered is illustrated in **Fig. 41** representing the diffraction pattern from the  $\text{Ni}_{45}\text{Mn}_{25}\text{Ga}_{25}\text{Co}_5$  powder prepared by ball-milling. Agate balls were chosen during sample preparation to prevent the contamination with Fe or other elements.

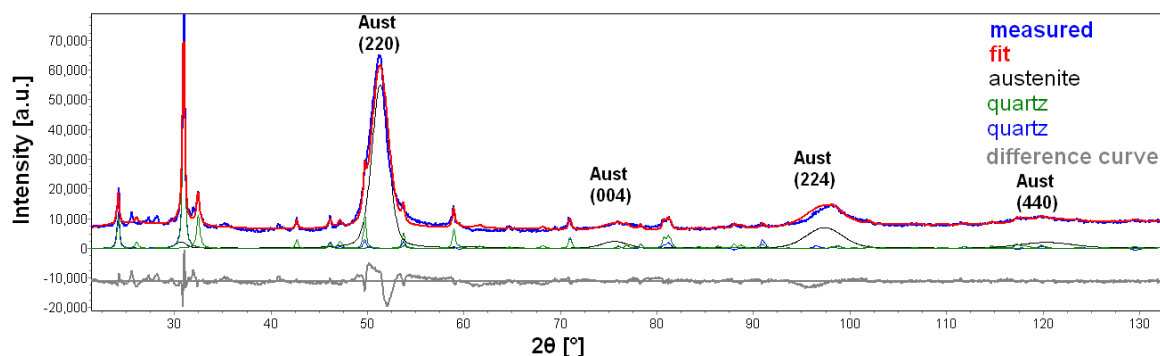


**Fig. 41:** The powder pattern obtained from the  $\text{Ni}_{45}\text{Mn}_{25}\text{Ga}_{25}\text{Co}_5$  sample, screenshot from TOPAS. Strong contamination with  $\text{SiO}_2$  has been discovered. Non-specified additional (probably martensitic) phase is indicated at the low angles.

Originating bulk oligocrystal exhibited pure austenite. The obtained powder consisted mainly (volume content  $\sim 80(10)$  %) of textured austenite phase with low crystallite size ( $< 20$  nm) and high microstrain. A small ( $\sim 3$  %) a residue of martensite phase indicated by the reflections at low angles. Surprisingly, the strong contamination ( $\sim 17$  %) from the  $\text{SiO}_2$  in two forms of hexagonal quartz was discovered in the pattern, probably originating from the milling. Given the smaller crystallite size, possible quantification error is large. This demonstration is therefore included just for the completeness of our explanation of the characterisation possibilities.

## 3.5 XRD characterisation of Ni-Mn-Ga oligocrystals and heavily textured polycrystals

Between the ideal single crystals and ideal polycrystals/powders, there is the region of oligocrystals – samples consisting of several units or tens of single grains. Here, the application of standard single-crystal or polycrystal XRD methods is hindered noticeably since the basic requirements (either single grain or the distribution of large amount of randomly oriented small grains) are not satisfied. The resulting diffraction pattern consists of the contributions from all the irradiated grains that usually cannot be reasonably resolved, and, at the same time, the number of single grains is not large enough to form the reasonable powder-like diffraction pattern. Unfortunately, this is the case of typical samples of the Ni-Mn-Ga-based alloys produced by arc-melting and thus I had to establish a standard method of oligocrystalline samples characterisation.

There are two approaches that could be used to deal with such samples: *i*) trying to distinguish the individual contributions from the individual grains and approaching them with single-crystal diffraction methods, or *ii*) trying to obtain powder-like 1D  $2\theta$  diagram from these samples. Both will be briefly described in the following chapters.

### 3.5.1 Structural characterisation of Ni-Mn-Ga oligocrystals using the single-crystal XRD approach

In case of several large-grains-containing oligocrystals, one could try to focus on a single grain by choosing the appropriate X-ray optics (e.g., monochromator optics or point focus with the very small slits) and follow the single-crystal routine listed in chapter 3.2. When such an approach is not possible (beam is too large, resp. grains are too small), one could still try to distinguish the contributions from distinct grains if their number is low. One should always bear in mind not only the contributions from the single grains, but also the contributions from the twinned variants possibly formed in each grain. In practice, especially in the case of twinned martensites, if the overlapped patterns from more than  $\sim 5$  grains are detected, one has to abandon this method and shift directly to the second approach (chapter 3.5.2).

Optionally, in case of large-enough grains, one can think of an extraction of single grain (e.g., by cutting or shock-freezing in liquid nitrogen that might break sample into single grains) and proceed with single-crystal characterisation techniques.

### 3.5.2 Structural characterisation of Ni-Mn-Ga oligocrystals and highly textured polycrystals using the powder XRD approach

The second approach represent various methods for collection of the powder diffraction pattern from single crystals, oligocrystals or highly textured polycrystals. In practice, these methods rely on the collection of the combined powder pattern consisting of contributions from different sample orientations achieved by sample rotation, oscillation, or other movements and their summation/integration. The most popular is probably the *Gandolfi method* for obtaining the powder pattern from single crystal while keeping the intensities ratio related to the structural factors.

Several analogue setups and experiments can be run using the conventional multipurpose X-ray diffractometer without the dedicated Gandolfi stage, usually at the expense of several notable limits: *i*) the intensities of the resulting diffraction peaks depend on various factors and usually cannot be easily related to the structure (e.g., in case of non-ideal sample shape without complex absorption correction, in case of different irradiated volume caused by sample tilts, or when all the sample orientations are not achieved); *ii*) the defocusing caused by the sample tilts influences the shape

of the diffraction maxima; *iii*) in some cases, results might not be complete (i.e., using these methods, one can detect the presence of various phases, nevertheless, one sometimes cannot reasonably disprove the possible presence of additional ones that have not been discovered).

Nevertheless, even though this method cannot be reasonably used for the complete structure solution, it can usually be used for the basic characterisation including the phase identification (in our case of limited possibilities), lattice parameter evaluation, detection of phase transitions during heating/cooling etc.

In practice, the sample rotation/oscillation/etc. is sometimes not necessary, and one could limit oneself to collection of as many reflections as possible from several grains. In this case, for each reflection the maximum in  $(\chi, \varphi)$  space can usually be found leading to the more precise peak positions. The limitation is that traces of other phases (if present) might sometimes be overlooked resulting in incomplete results. For certainty, larger amount of measured pole figures for different  $2\theta$  angles is necessary together with the measurements of the  $2\theta$  scans in broad  $2\theta$  interval. Alternatively, this method could be used in combination with other (magnetic, electric etc.) measurements.

Noteworthy, even if it might look that the inevitable twinning is a nuisance complicating the analysis of single crystals, when it comes to collection of as many reflections as possible from oligocrystalline samples, twinning is in fact beneficial and in some cases allows measuring multiple  $\{hkl\}$  reflections in one  $2\theta$  scan.

### 3.5.2.1 Highly textured polycrystal

During my work, I encountered many arc-melted samples that were of polycrystalline nature (although sometimes with larger grains) with strong fibre texture. Here, the (100) and (001) axes of the martensite variants (**Fig. 42**) usually went in the heat dissipation direction, while the axes perpendicular to these covered symmetrically the whole circle of orientations as indicated by the pole figures showing typical fibre texture, **Fig. 43**.

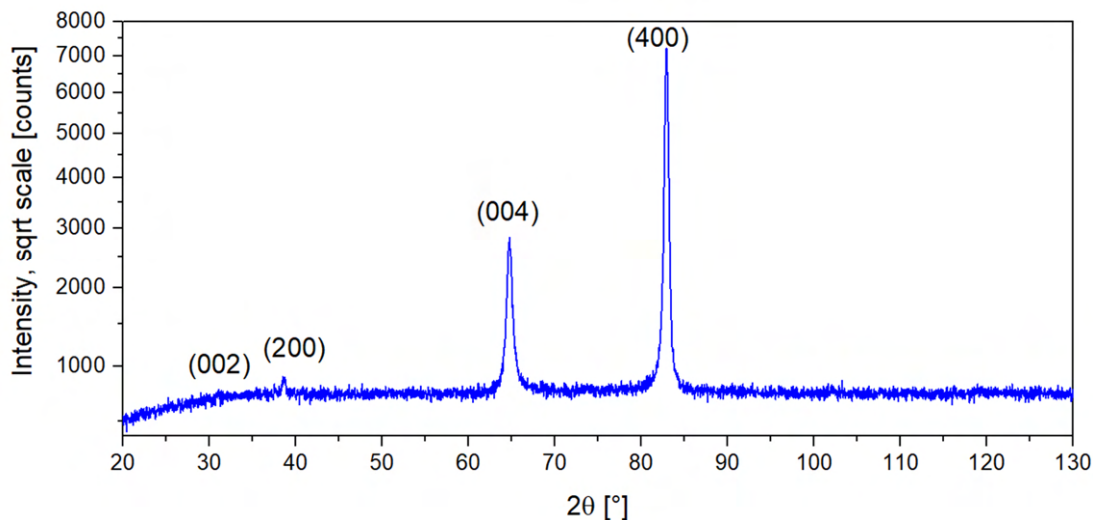


**Fig. 42:** Original Bragg-Brentano scan for the arc-melted  $\text{Ni}_{50}\text{Mn}_{24}\text{Ga}_{18}\text{Fe}_4\text{Cu}_4$  at  $\varphi = 0^\circ$ ,  $\chi = 0^\circ$ . Two detected peaks are the (400) and (004) reflections of the non-modulated martensite, both are present due to the *a/c* twinning and the beam divergence.

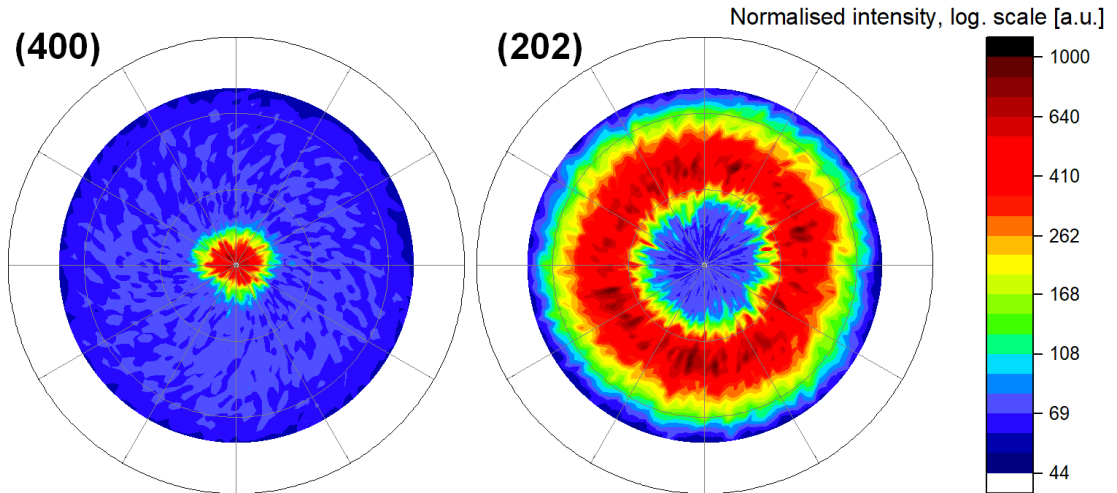


**Fig. 43:** Pole figures of (400) and (202) reflection of the arc-melted  $\text{Ni}_{50}\text{Mn}_{24}\text{Ga}_{18}\text{Fe}_4\text{Cu}_4$  sample clearly indicating strong fibre texture.

In case of such fibre texture, full set of achievable reflections can be collected by simple automated measurements of individual gonio scans with different sample  $\chi$  tilts (covering reasonable range) for one or several  $\varphi$  angles indicated by the pole figures. Such measurement is demonstrated in **Fig. 44** for  $\varphi = 0^\circ$ . After the summation of the individual scans and peak indexation (here following the unit cell and symmetry of the non-modulated tetragonal martensite), **Fig. 45**, lattice parameters were determined as  $a = 5.408 \text{ \AA}$ ,  $c = 6.678 \text{ \AA}$ .

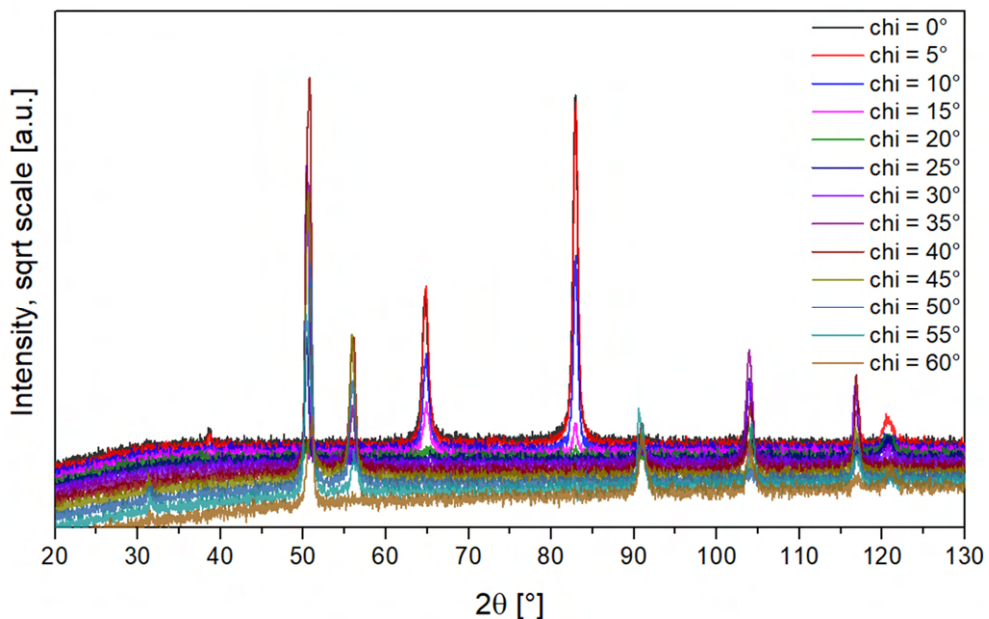


**Fig. 44:** Set of Gonio scans collected for the newly casted  $\text{Ni}_{50}\text{Mn}_{24}\text{Ga}_{18}\text{Fe}_4\text{Cu}_4$  alloy. 13 scans were performed for different  $\chi$  tilts from  $\chi = 0^\circ$  (top) to  $\chi = 60^\circ$  (bottom) in  $5^\circ$  steps. For clearer visualisation, constant offsets are used to accentuate individual scans. Given the strong fibre-like texture of the bulk polycrystal, all the achievable reflections were reasonably measured with this procedure.

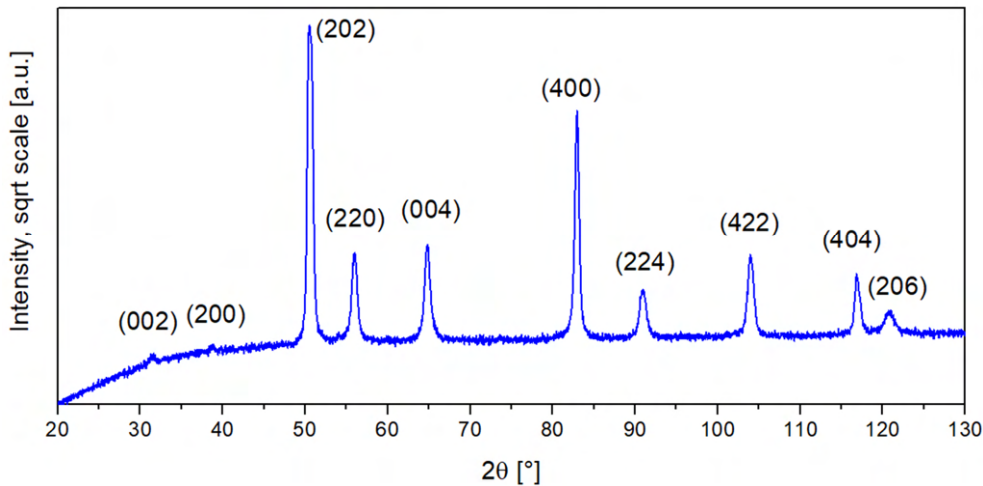


**Fig. 45:** Overall 1D scan obtained as a sum of individual scans from **Fig. 44**.

### 3.5.2.2 True oligocrystal

The unsuccessful attempts to obtain real single crystals sometimes bring bulk samples of oligocrystalline nature. This can also be the case of arc-melted samples containing elements like Co, that seems to increase the grain growth. Resulting samples usually contain several units or tens of grains. Here one usually has to “hunt” for single reflections by initial measurement of multiple pole figures and then hunting for the precise  $2\theta$  values, similarly to the procedure described in chapter 3.2.

Illustration of the situation can be shown for the  $\text{Ni}_{50}\text{Mn}_{25}\text{Ga}_{20}\text{Co}_5$  oligocrystal. From the magnetic measurements with temperature (not shown), a non-modulated martensite was expected. Nevertheless, to exclude potential presence of another phases, collection of pole figures at  $2\theta$  angles:  $66^\circ$ - $82^\circ$  with  $2^\circ$  steps was conducted (here the main martensite/austenite reflections (400), (040) and (004) appear). Open detector with  $2\theta$  acceptance angle of  $\sim 2.1^\circ$  covered the interval fully (especially given the usual broadness of the peaks). In other words, was there any reflection present, it would be detected in such pole figures.

Only peaks at  $2\theta$  angles corresponding roughly to the (400) and (004) reflections of NM martensite were found in the pole figures, shown in **Fig. 46**. Measurements clearly indicated the oligocrystalline nature of the sample. The rest of pole figures excluded possible presence of other phases expected for Ni-Mn-Ga (i.e., 10M and 14M martensite and austenite), **Fig. 47**.

Measurement was followed by pole figure scans at  $2\theta$  of  $50.4^\circ$ ,  $55.5^\circ$ ,  $91.1^\circ$  and  $103.7^\circ$ , where the (202), (220), (224) and (422) reflections were expected, **Fig. 46**.

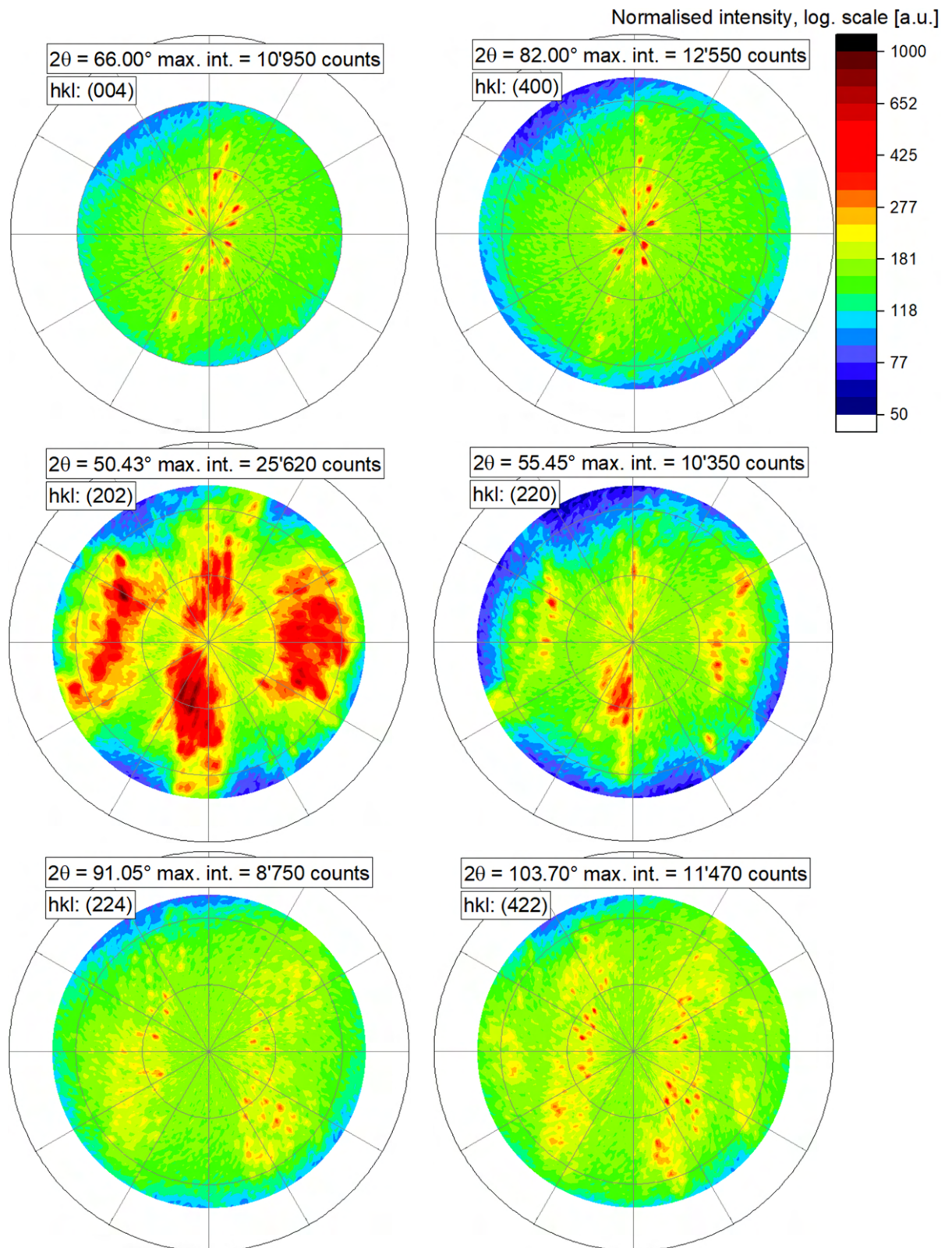


**Fig. 46:** Pole figures of the (004), (400), (202), (220), (224), and (422) reflections collected for the  $\text{Ni}_{50}\text{Mn}_{25}\text{Ga}_{20}\text{Co}_5$  sample (created by arc melting in 2021). Individual spots indicate presence of multiple ( $\sim 15$ ) grains. All the pole figures use the same intensity scale normalised with respect to the global maximum of intensity (25620 counts).

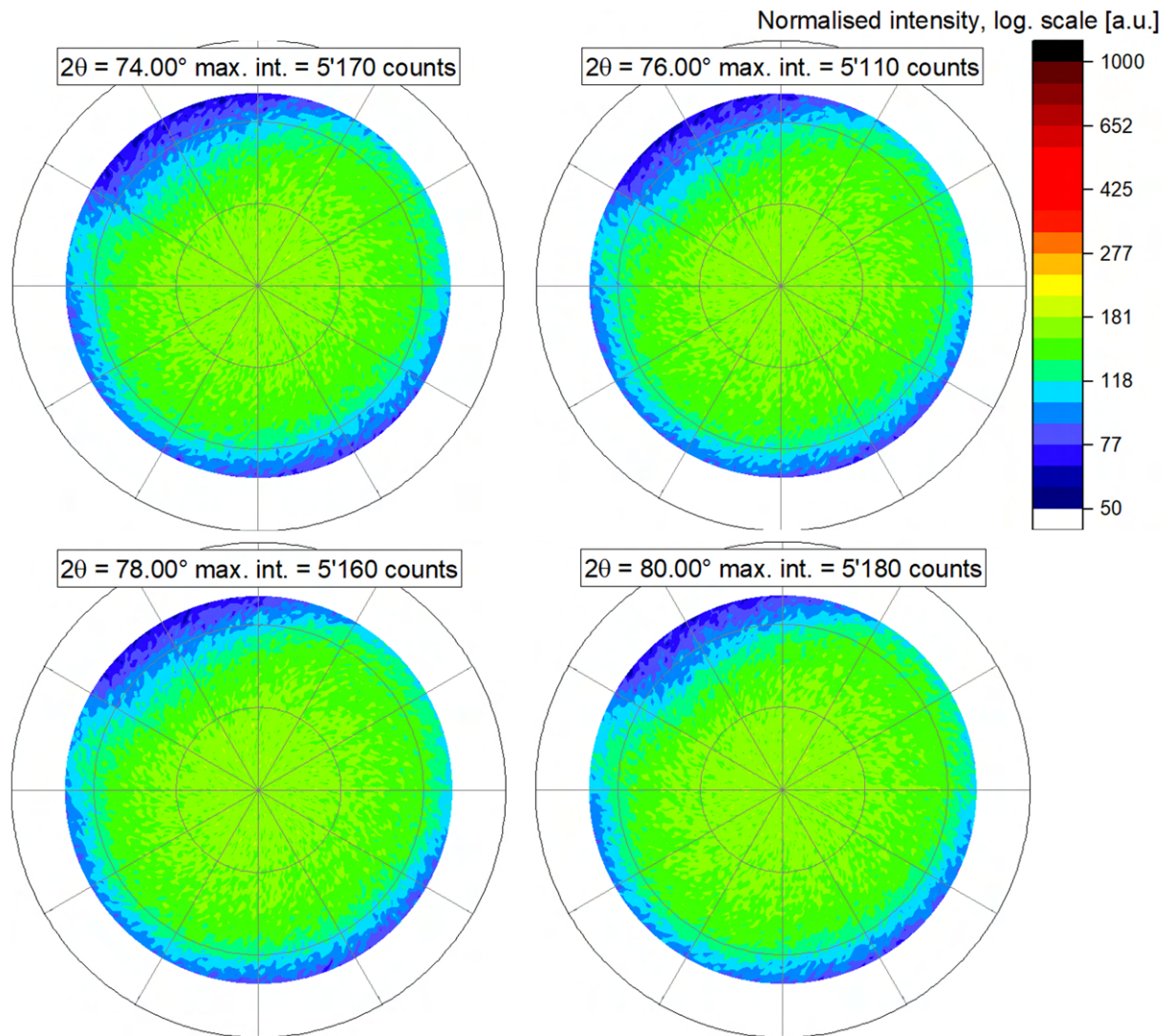


**Fig. 47:** Examples of the pole figures serving for exclusion of other phases measured in the  $2\theta$  region of expected reflections from 10M, 14M, and/or austenite in the  $\text{Ni}_{50}\text{Mn}_{25}\text{Ga}_{20}\text{Co}_5$  sample (created by arc melting in 2021). No peaks were detected, all the detected intensity is the background. All the pole figures use the same intensity scale as the pole figures in Fig. 46 normalised with respect to the global maximum of intensity (25620 counts).

All the measured pole figures confirmed the presence of  $\sim 15$  grains. To calculate the lattice parameters of the detected NM martensite, several points from the figures were chosen (preferably those with the highest intensity and those requiring the smallest sample tilt), followed by the  $2\theta$ - $\omega$  scans with parallel beam optics (for better focusing and elimination of the possible sample displacement effect during tilting) for the (400), (004), (220), (202), (422) and (224) reflections. For illustration, all the collected scans are plotted together in **Fig. 48**.



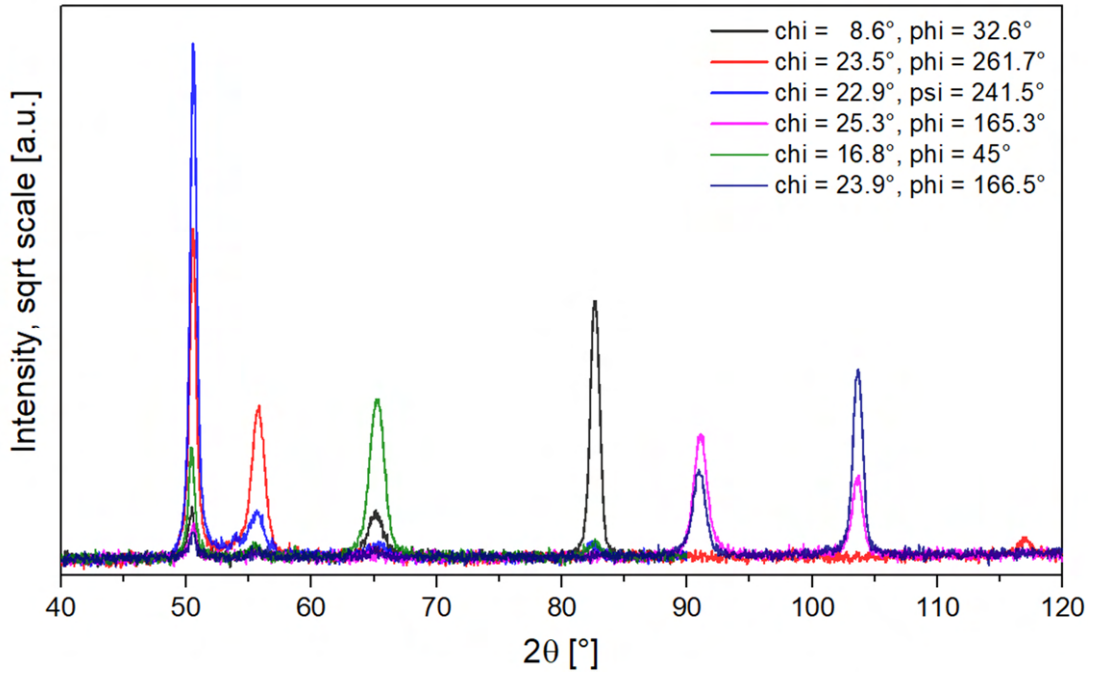


**Fig. 48:**  $2\theta$  scans measured for the several  $(\chi, \phi)$  orientations chosen from the pole figures.

Each peak in the scans was fitted using *FitExc* fitting program to obtain the accurate values of the Bragg angles. Then, least squares method was used to obtain the final lattice parameters  $a = b = 5.420 \text{ \AA}$ ,  $c = 6.635 \text{ \AA}$ . Given the high precision of the peak maxima determination and the number of peaks used for calculation of two parameters, the lattice parameter precision was estimated as  $0.002 \text{ \AA}$  or better.

Described approach works for the situations of several units to tens of grains. In case of single-phase samples, the whole process can usually be performed within one day of measurement and simultaneous data processing. Unfortunately, given the necessity of on-the-go adjustments, the active presence of the XRD operator is necessary during the whole experiment.

## 4 Results and discussion

Focusing on structural characterisation, I have contributed to the fundamental and material research of Ni-Mn-Ga-based Heusler alloys within MSM group. I addressed several essential topics of the field. My experimental work dived deeply into structural problems connected with twinned and modulated martensites and contributed to the understanding of the structure, which is still far from complete. Given broadness of the topic, the results and discussion section are divided into these parts:

- Characterisation of the newly casted Ni-Mn-Ga-based single-, poly- and oligocrystalline samples
- Evaluation of the crystal quality of Ni-Mn-Ga single crystals
- Characterisation of the NM martensite – the extrapolation of zero-Kelvin lattice parameters for ab-initio study
- Characterisation of the 14M modulated martensite
- Analysis of nanotwinned form of 10M martensite
- Studies of the structural modulation within the 10M modulated martensite of Ni-Mn-Ga(-Fe) single crystals

These are ordered from the simplest routine tasks to more fundamental research with valuable outcomes for the field. In each part, the main scientific conclusions and their implication will be described and discussed together with the references to the published work.

### 4.1 Characterisation of the newly casted Ni-Mn-Ga-based single-, poly- and oligocrystalline samples

My XRD results represented a crucial (although routine) part in the research of newly casted Cu-, Cr- and Fe-alloyed  $\text{Ni}_2\text{MnGa}$ -based alloys. Here, the information on phase composition, crystal nature and lattice parameters represent the very base of understanding of the material. Presented results are divided into three sub-chapters based on the alloying elements used and the connection to publication outputs.

#### 4.1.1 Full variation of site substitution in Ni-Mn-Ga by ferromagnetic transition metals

I took a part in the studies of full variation of site substitution in Ni-Mn-Ga by ferromagnetic transition metals [57]. In the study, nine different Fe-, Co-, and Ni- alloyed  $\text{Ni}_2\text{MnGa}$  samples were analysed with nominal compositions:  $\text{Ni}_{45}\text{Mn}_{25}\text{Ga}_{25}\text{Fe}_5$ ,  $\text{Ni}_{50}\text{Mn}_{20}\text{Ga}_{25}\text{Fe}_5$ ,  $\text{Ni}_{50}\text{Mn}_{25}\text{Ga}_{20}\text{Fe}_5$ ,  $\text{Ni}_{45}\text{Mn}_{25}\text{Ga}_{25}\text{Co}_5$ ,  $\text{Ni}_{50}\text{Mn}_{20}\text{Ga}_{25}\text{Co}_5$ ,  $\text{Ni}_{50}\text{Mn}_{25}\text{Ga}_{20}\text{Co}_5$ ,  $\text{Ni}_{50}\text{Mn}_{25}\text{Ga}_{25}$ ,  $\text{Ni}_{55}\text{Mn}_{20}\text{Ga}_{25}$ , and  $\text{Ni}_{55}\text{Mn}_{25}\text{Ga}_{20}$ . Samples clearly were of oligocrystalline nature, as illustrated in the (400) and (202) pole figures of the  $\text{Ni}_{45}\text{Mn}_{25}\text{Ga}_{25}\text{Fe}_5$  sample, **Fig. 49**, and (400) and (004) pole figures of the  $\text{Ni}_{50}\text{Mn}_{25}\text{Ga}_{20}\text{Co}_5$  sample, **Fig. 50**.

Similarly to the approach described in chapter 3.5.4, for all the measured alloys, care was taken to clearly exclude the possible presence of other phases typical for Ni-Mn-Ga. Illustration is also presented in **Fig. 50**, here excluding the possible presence of austenite, 10M or 14M martensite in the  $\text{Ni}_{50}\text{Mn}_{25}\text{Ga}_{20}\text{Co}_5$  sample. Further proof was presented in **Fig. 47** used earlier for the demonstration of the method – here the pole figures were measured for the sample of the same composition from the new batch of casted alloys).

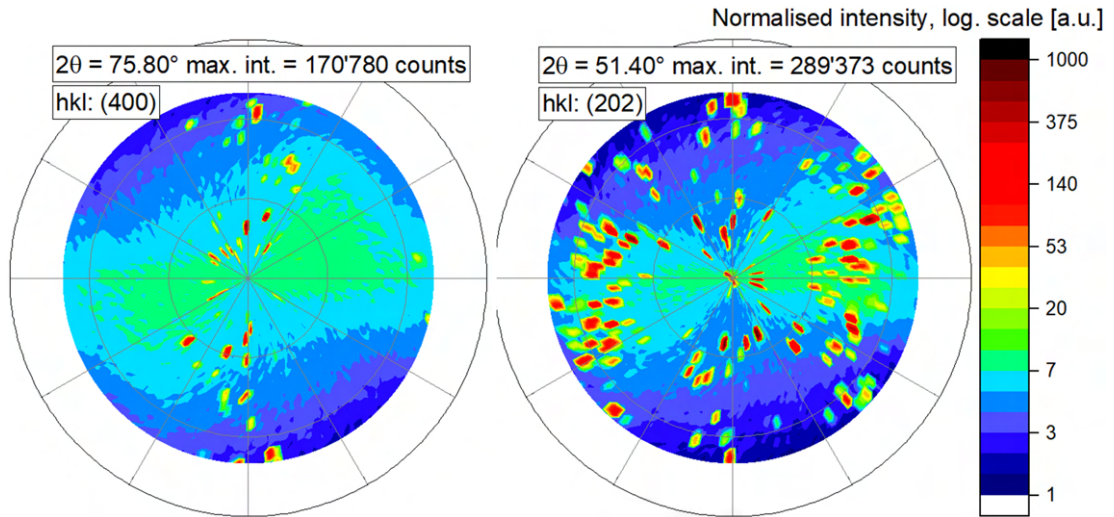


**Fig. 49:** Pole figures of (400) and (202) reflections of the austenite phase of the  $\text{Ni}_{45}\text{Mn}_{25}\text{Ga}_{25}\text{Fe}_5$  sample indicating oligocrystalline nature with  $\sim 25$  grains.

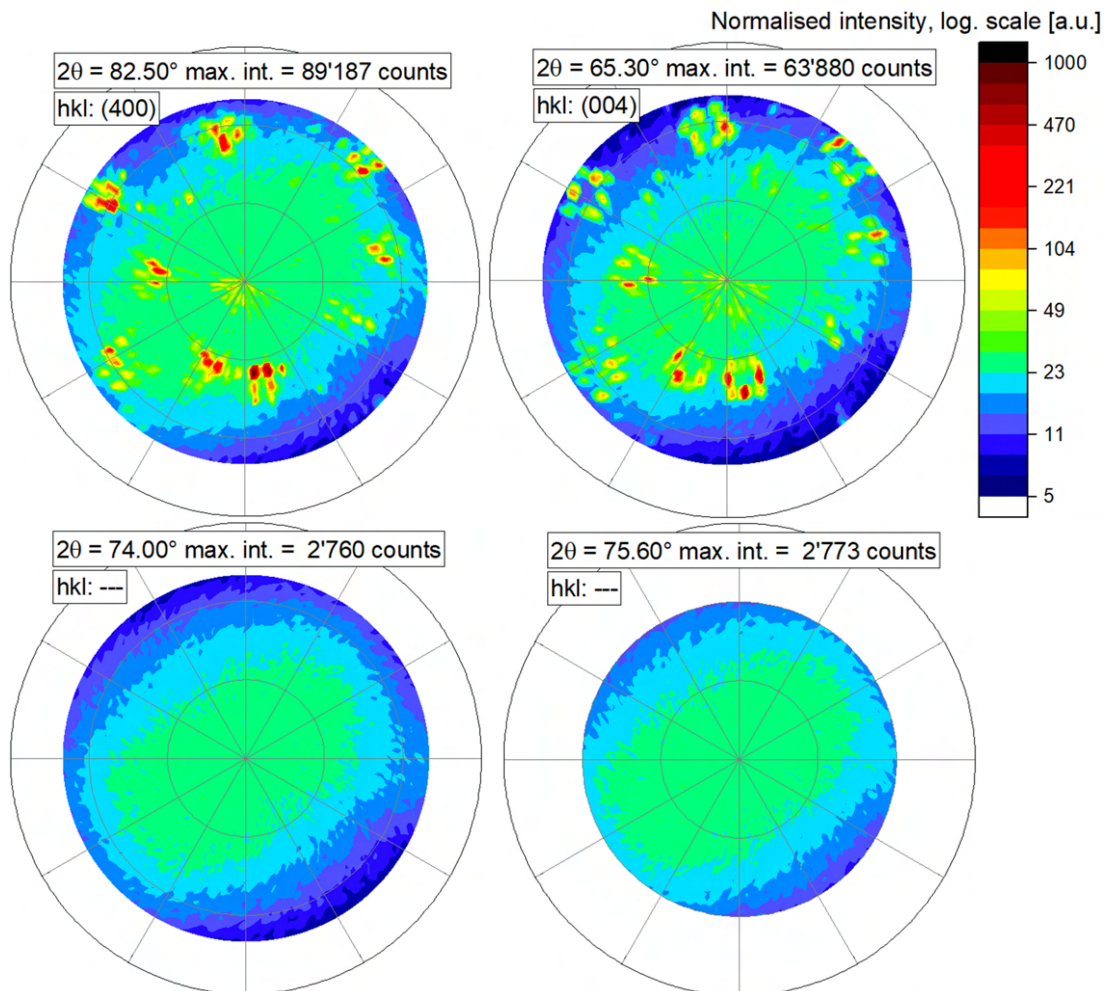


**Fig. 50:** Pole figures of the  $\text{Ni}_{50}\text{Mn}_{25}\text{Ga}_{20}\text{Co}_5$  sample (created by arc-melting in 2019). Peaks at the almost same positions in the (400) and (004) pole figures indicate *alc* twinning, slight differences in the orientations are given by the orientation relation between a- and c-oriented variants. Pole figures measured for  $2\theta$  of  $74.0^\circ$  and  $75.6^\circ$  are plotted as a proof that neither austenite nor 10M martensite phase were present in the sample.

Noteworthy, the (400) and (004) reflections of the NM martensite appearing with the very similar orientation in the pole figures presented in **Fig. 50** indicate the twinned microstructure within individual grains of the oligocrystal.

Combined diffraction patterns representing the sums of individual  $2\theta$ - $\omega$  scans measured for each sample are plotted in **Fig. 51** with names using simplified previously described identifier. From the pole figures and these patterns, phase and lattice parameters were evaluated. Results are summarized in **Table 3**.

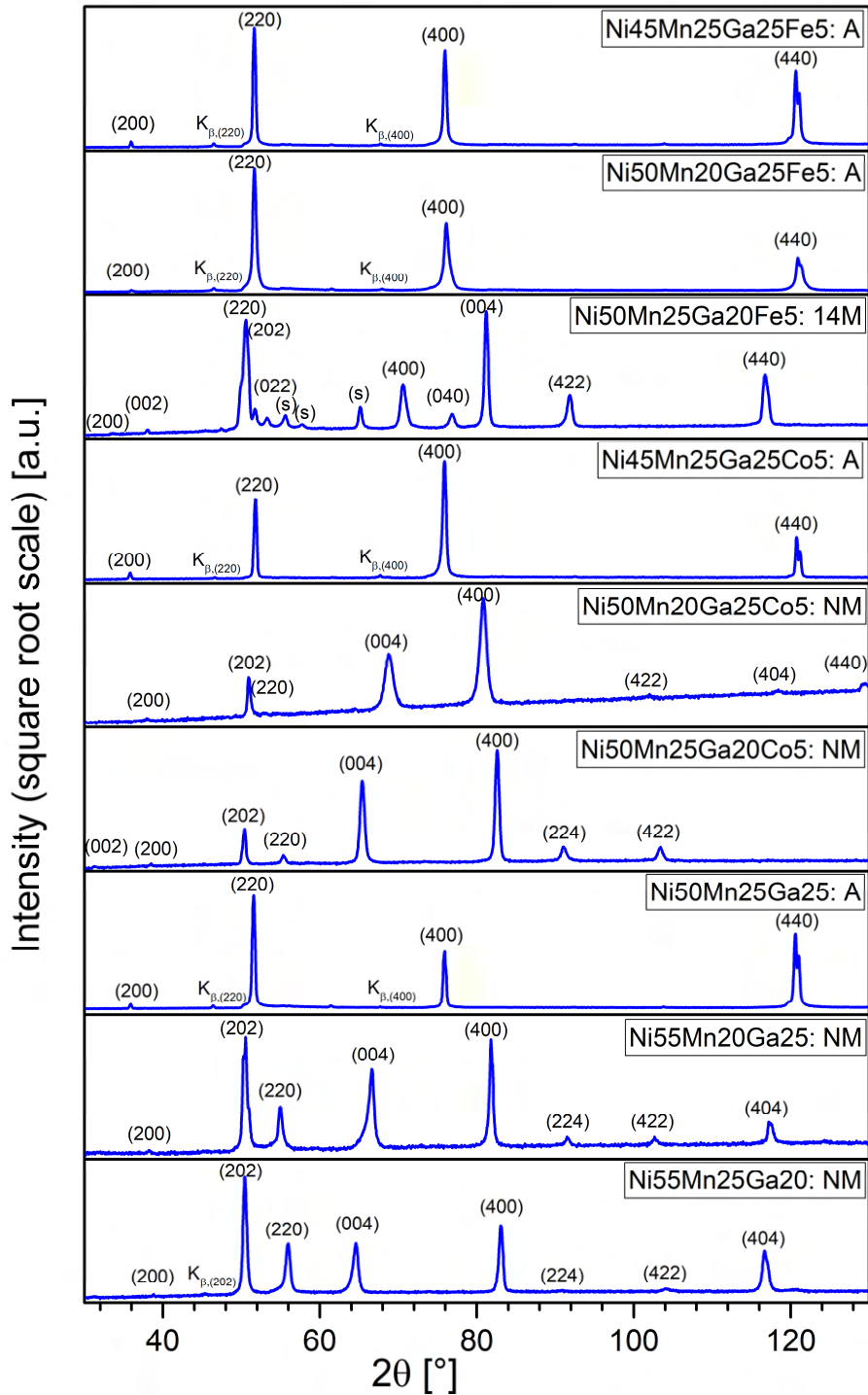


**Fig. 51:** Indexed diffraction patterns of the  $\text{Ni}_2\text{Mn}$ -Ga alloyed by 5% of Ni, Co, or Fe. Each pattern represents the sum of at least 4 scans collected for different  $(\chi, \varphi)$  orientations chosen based on the pole figures. Based on these, the distinct austenite (marked A) and martensite phases (14M and NM) were identified. Modified image published in [57] (supplementary).

**Table 3:** Determined phase and the lattice parameters (in Å) of the newly casted Fe-, Co-, and Ni-alloyed Ni-Mn-Ga. Adapted from the original publication with the approval of the first author [57]

Sample	$a_0$	$a$	$b$	$c$	$\gamma$	$c/a$	Structure
Ni <sub>45</sub> Mn <sub>25</sub> Ga <sub>25</sub> Fe <sub>5</sub>	5.827(1)	-	-	-	90	-	A
Ni <sub>50</sub> Mn <sub>20</sub> Ga <sub>25</sub> Fe <sub>5</sub>	5.814(1)	-	-	-	90	-	A
Ni <sub>50</sub> Mn <sub>25</sub> Ga <sub>20</sub> Fe <sub>5</sub>	-	6.200(2)	5.764(2)	5.506(2)	90.4(2)	0.89	14M
Ni <sub>45</sub> Mn <sub>25</sub> Ga <sub>25</sub> Co <sub>5</sub>	5.822(1)	-	-	-	90	-	A
Ni <sub>50</sub> Mn <sub>20</sub> Ga <sub>25</sub> Co <sub>5</sub>	-	5.535(2)	-	6.384(2)	90	1.15	NM
Ni <sub>50</sub> Mn <sub>25</sub> Ga <sub>20</sub> Co <sub>5</sub>	-	5.424(2)	-	6.630(2)	90	1.22	NM
Ni <sub>50</sub> Mn <sub>25</sub> Ga <sub>25</sub>	5.818(5)	-	-	-	90	-	A
Ni <sub>55</sub> Mn <sub>20</sub> Ga <sub>25</sub>	-	5.469(4)	-	6.515(5)	90	1.19	NM
Ni <sub>55</sub> Mn <sub>25</sub> Ga <sub>20</sub>	-	5.392(2)	-	6.701(1)	90	1.24	NM

#### 4.1.2 Systematic trends of transformation temperatures and crystal structure of Ni-Mn-Ga-Fe-Cu alloys

Similar characterisation was performed during the study of systematic trends of transformation temperatures and crystal structure of Ni-Mn-Ga-Fe-Cu alloys, i.e., Ni<sub>50</sub>Mn<sub>25</sub>Ga<sub>23</sub>Fe<sub>1</sub>Cu<sub>1</sub>, Ni<sub>50</sub>Mn<sub>25</sub>Ga<sub>21</sub>Fe<sub>2</sub>Cu<sub>2</sub>, Ni<sub>50</sub>Mn<sub>25</sub>Ga<sub>17</sub>Fe<sub>4</sub>Cu<sub>4</sub>, Ni<sub>50</sub>Mn<sub>25</sub>Ga<sub>24.5</sub>Cu<sub>0.5</sub>, Ni<sub>50</sub>Mn<sub>25</sub>Ga<sub>22.5</sub>Fe<sub>2</sub>Cu<sub>0.5</sub>, and Ni<sub>50</sub>Mn<sub>25</sub>Ga<sub>20.5</sub>Fe<sub>4</sub>Cu<sub>0.5</sub> (nominal compositions) [104]. Samples were mostly of highly textured polycrystalline nature with large grains, as illustrated in the pole figures, **Fig. 52** and previously shown **Fig. 43**. The aim of the XRD characterisation was to determine the phase composition and lattice parameters at room temperature and, for selected samples, also on cooling to 250 K. The results are summed up in Table 4. Analysis was performed for both the as-cast and annealed sample states. In some cases, multiple coexisting phases were identified, especially in the as-cast samples. Illustrative examples of final XRD patterns obtained using the procedures described in chapter 3.5 are shown in **Fig. 53**. Results were published in [104].

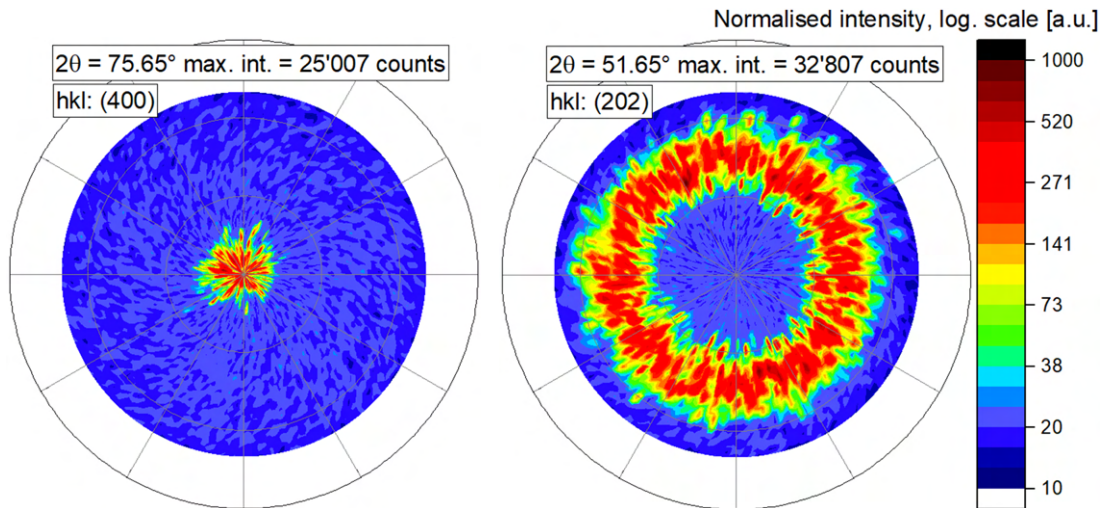


**Fig. 52:** (400) and (202) pole figures of the austenite of Ni<sub>50</sub>Mn<sub>25</sub>Ga<sub>24.5</sub>Cu<sub>0.5</sub> sample indicating complicated character of the sample – highly textured polycrystal with large grains.

Interesting side result of the characterisation of these new alloys is the detected strong fibre texture in the majority of the analysed samples. This indicates that this bulk material in polycrystalline form can probably exhibit the MIR in the specific directions of preferred orientation.

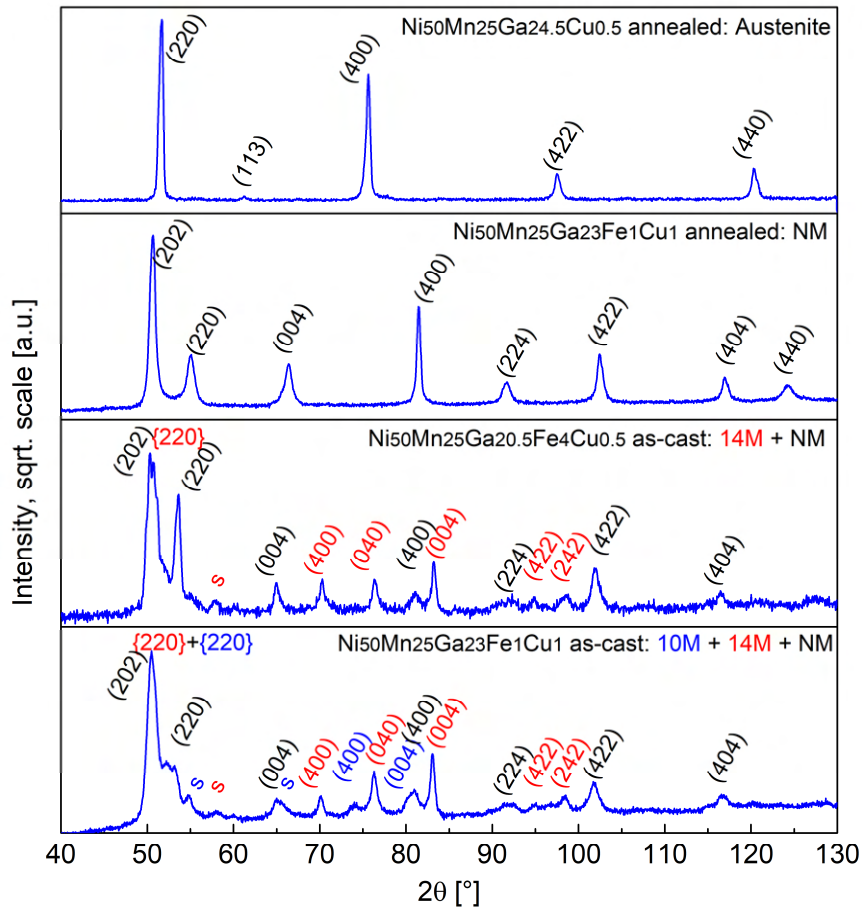


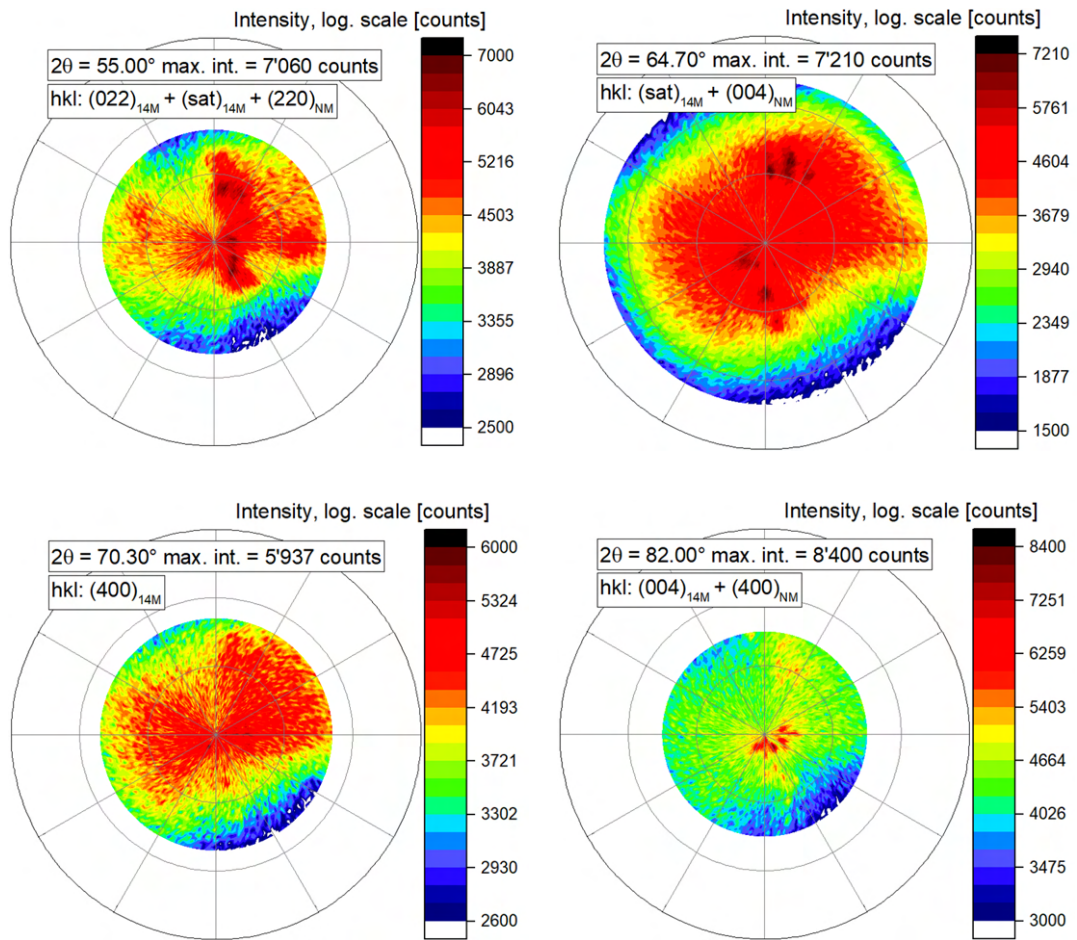
Fig. 53: Illustration of four summed patterns obtained for Ni-Mn-Ga-Fe-Cu samples.

Table 4: Determined phases found in the newly casted Ni-Mn-Ga-Fe-Cu samples. Adapted from [104]

sample	state	phase	a [Å]	b [Å]	c [Å]	$\gamma$ [°]
Ni <sub>50</sub> Mn <sub>25</sub> Ga <sub>23</sub> Fe <sub>1</sub> Cu <sub>1</sub>	as-cast	10M+14M+NM	- not	analysed	further	-
	annealed	NM	5.48		6.54	
Ni <sub>50</sub> Mn <sub>25</sub> Ga <sub>21</sub> Fe <sub>2</sub> Cu <sub>2</sub>	as-cast	NM	5.46		6.60	
	annealed	NM	5.45		6.60	
Ni <sub>50</sub> Mn <sub>25</sub> Ga <sub>17</sub> Fe <sub>4</sub> Cu <sub>4</sub>	as-cast	NM	5.41		6.68	
	annealed	NM	5.40		6.68	
Ni <sub>50</sub> Mn <sub>25</sub> Ga <sub>24.5</sub> Cu <sub>0.5</sub>	as-cast	A	5.83			
	annealed	A	5.83			
Ni <sub>50</sub> Mn <sub>25</sub> Ga <sub>22.5</sub> Fe <sub>2</sub> Cu <sub>0.5</sub>	as-cast	A	5.83			
	annealed	A	5.83			
	annealed, T=250 K	10M	5.99	5.96	5.59	90.3
Ni <sub>50</sub> Mn <sub>25</sub> Ga <sub>20.5</sub> Fe <sub>4</sub> Cu <sub>0.5</sub>	as-cast	14M	6.22	5.78	5.50	90.7
		NM	5.39		6.67	
	annealed	14M	6.22	5.78	5.50	90.7
		NM	5.39		6.67	

### 4.1.3 Highly textured polycrystal of $\text{Ni}_{50}\text{Mn}_{25}\text{Ga}_{20}\text{Cr}_5$

Slightly more difficult problem represented the recent characterisation of the  $\text{Ni}_{50}\text{Mn}_{25}\text{Ga}_{20}\text{Cr}_5$  alloy. Measurements indicated highly textured polycrystalline nature with the mixture of small and very large grains as indicated by the pole figures, **Fig. 54**. Due to the nature of the sample and content of Cr, the signal-to-noise ratio (SNR) was unfortunately low further complicating the analysis. Full set of measured  $2\theta$ - $\omega$  scans in the  $(\chi, \varphi)$  orientations suggested by the pole figures are shown in **Fig. 55** after background subtraction necessary for further processing due to the low SNR.



**Fig. 54:** Pole figures measured for the  $\text{Ni}_{50}\text{Mn}_{25}\text{Ga}_{20}\text{Cr}_5$  sample at  $2\theta$  angles of  $55.0^\circ$ ,  $64.7^\circ$ ,  $70.3^\circ$  and  $82.0^\circ$  indicating polycrystalline nature of the sample with some larger grain grown in specific directions. Given the noticeable overlap of NM and 14M reflections and detector acceptance range of  $2.1^\circ$ , contributions from multiple reflections are present in the pole figure.

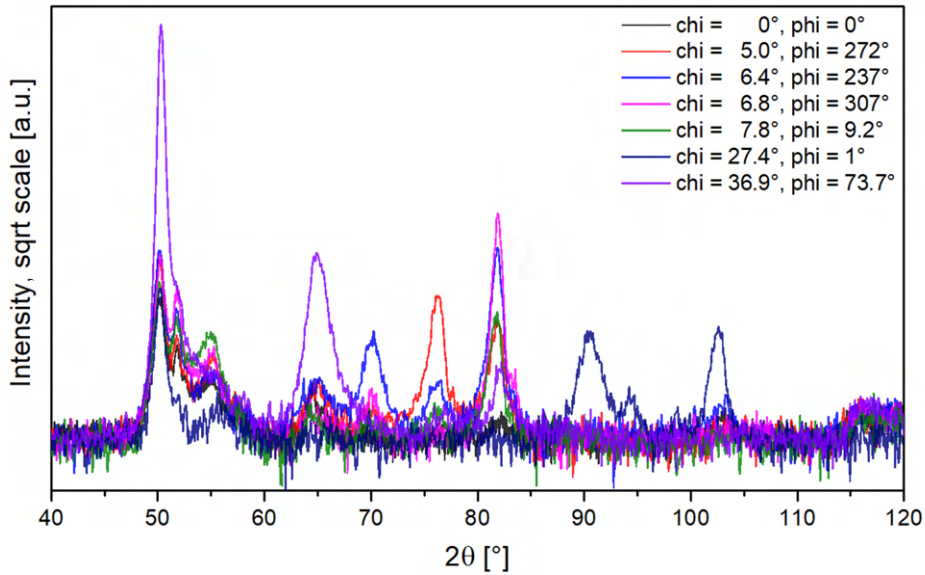


**Fig. 55:** Seven  $2\theta$ - $\omega$  scans measured for the  $\text{Ni}_{50}\text{Mn}_{25}\text{Ga}_{20}\text{Cr}_5$  alloy. Due to the low signal-to-noise ratio, background has been partially subtracted for better peak visibility.

The resulting combination of the scans was fitted with combination of NM and 14M phases. These were chosen as suitable initial candidates based on the magnetic measurements and based on the presented single scans. Twinned NM and 14M variants are indicated by the detected reflections in one scan – i.e., the curve for  $\chi = 6.8^\circ$ ,  $\varphi = 307^\circ$  in **Fig. 55** contains both (400) and (004) peaks of NM martensite thanks to the divergent beam geometry. Indexed combined diffraction pattern is presented in **Fig. 56**. The lattice parameters of the NM martensite were determined as  $a = 5.458 \text{ \AA}$ ,  $c = 6.664 \text{ \AA}$ , and 14M martensite as  $a = 6.229 \text{ \AA}$ ,  $b = 5.797 \text{ \AA}$ ,  $c = 5.562 \text{ \AA}$ ,  $\gamma = 90.78^\circ$ .

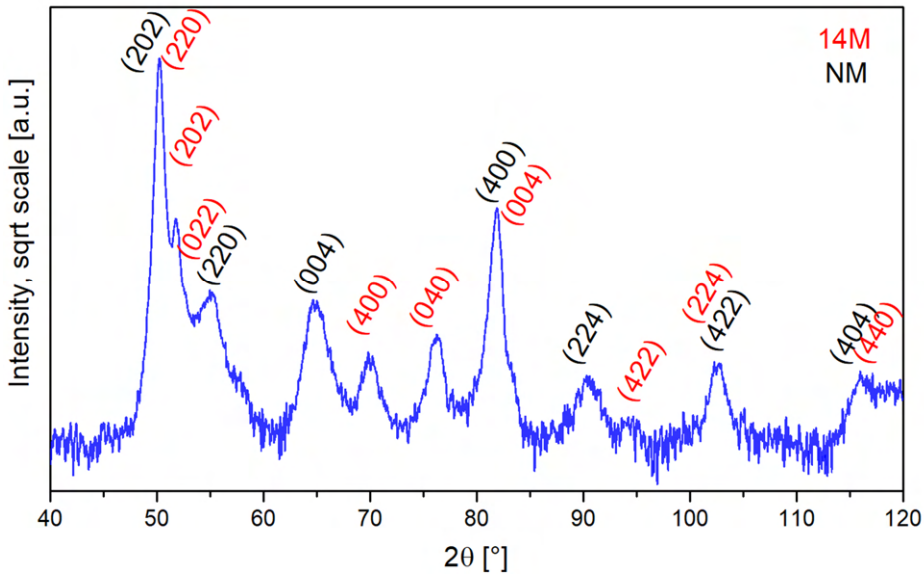


**Fig. 56:** Indexed combined diffraction pattern of  $\text{Ni}_{50}\text{Mn}_{25}\text{Ga}_{20}\text{Cr}_5$  sample.



## 4.2 Evaluation of the crystal quality of Ni-Mn-Ga single crystals

To see what can influence the MSM functionality or twin boundary motion, we studied crystal quality of four single crystals of the same stoichiometry ( $\text{Ni}_{150}\text{Mn}_{28}\text{Ga}_{22}$ ) obtained from four different producers: the *FZU*, Charles University (*CU*), Boise State University (*BSU*), and commercially available sample from Goodfellows (*GF*). All the crystals were cut in the plane with (100) normal direction. The crystal mosaicity was chosen as a suitable crystal quality metric readily available.

Following the traditional approaches, one would measure one-dimensional  $\omega$  scans of the reflection with suitable orientation – in our case, the strong (400) reflection. Nevertheless, this approach is not correct in case of twinned Ni-Mn-Ga crystals, because of the overlapped (400) and (040) twinned reflections that might influence the 1D rocking-curve and lead to misinterpretation. Orientation of these twinned reflections in space depends on the orientation of the *ab* twins in the crystal, see chapter 3.2.3 and [110].

Instead, two-dimensional maps were measured as these contain the full information, i.e., spread of both overlapped reflections due to mosaicity (analogue of the rocking curve) as well as the information on the contribution from the *a*- and *b*- oriented variants.

The measurements (in form of  $2\theta$ - $\omega$ - $\omega_{\text{offset}}$  2D maps for (400) + (040) reflections) indicated the lowest mosaicity in the CU crystal, **Fig. 57**. Here, one mosaic block was observed with FWHM (full width at half-maximum) of  $0.66^\circ$  in the rocking direction. Both *FZU* and *BSU* crystal showed presence of multiple mosaic blocks. The GF crystal showed a noticeably wider peak in the rocking direction with FWHM of  $1.7^\circ$  indicating larger crystal mosaicity.

The overall results of the paper showed that the crystal quality affects the magnitude of the twinning stress only indirectly, through its impact on the character of the twin boundaries. [103] The article also showed slight discrepancy from the nominal  $\text{Ni}_{150}\text{Mn}_{28}\text{Ga}_{22}$  stoichiometry. This was obvious also from my XRD measurements – differences in the  $2\theta$  positions of the (400) and (040) reflections indicate slight differences in *a* and *b* lattice parameters, that are usually caused by slightly different compositions (in cases without any external or internal stresses etc.).

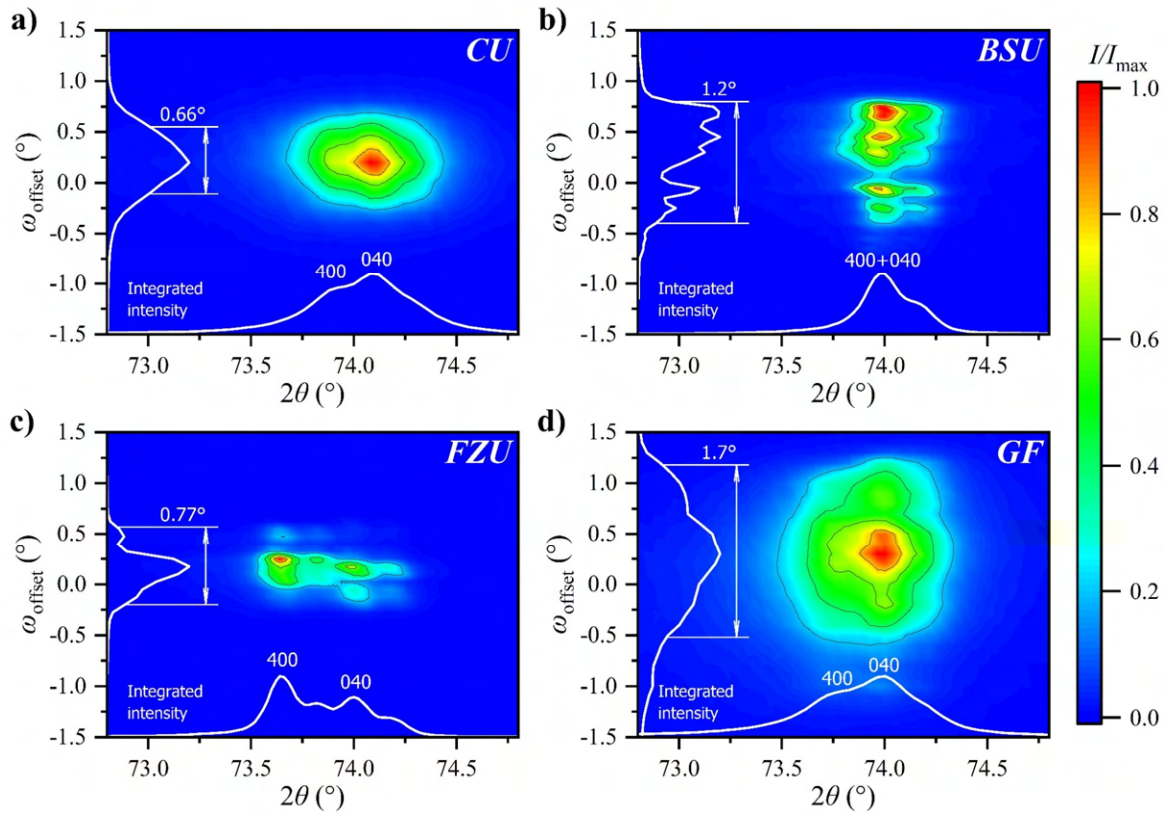


**Fig. 57:** 2D  $2\theta$ - $\omega_{\text{offset}}$  scans showing the crystal mosaicity. Including the projections to the  $x$ - and  $y$ -axes. [103]

### 4.3 Characterisation of the NM martensite – the extrapolation of zero-Kelvin lattice parameters for *ab-initio* study

During my PhD studies, I have often encountered the non-modulated martensite. Being usually stable at the lowest temperature (if present), it is often considered a ground martensite state. Even though the non-modulated martensite does not seem to be the most promising candidate for the MSM applications, its understanding still represents the keystone in understanding this whole class of alloys. Due to its relative simplicity, the NM martensite is also easiest approachable martensite phase by the *ab-initio* calculations. These first-principles calculations usually deal with the minimum-energy zero-Kelvin states. This brings the necessity to obtain experimental lattice parameters and the  $c/a$  ratio at temperatures as low as possible, or enough data for approximation at 0 K.

To provide such data,  $\text{Ni}_{53}\text{Mn}_{24}\text{Ga}_{23}$  single crystal was analysed. Crystal exhibited stable NM martensite for  $T < 360$  K. Thermal evolution of the lattice parameters was examined in the temperature range of (93-360 K). The temperature of 93 K was the lowest achievable with our DCS 500 domed cooling stage at the time of experiment. Aiming to obtain enough data for the reasonable extrapolation of the  $c/a$  ratio down to 0 K, lattice parameters were measured in small temperature steps for better precision of the extrapolation, **Fig. 58**. Data extrapolation to 0 K was performed with rational function. This led to better fit than the standard polynomial functions that are widely used. Furthermore, rational functions are known to have more stable interpolatory and extrapolatory properties [122]. Based on the fit of the  $c$ - and  $a$ - lattice parameters, the  $c/a$  ratio calculated for each temperature was extrapolated down to 0 K as  $(c/a)_{T=0\text{ K}} = 1.221$ , **Fig. 59**.

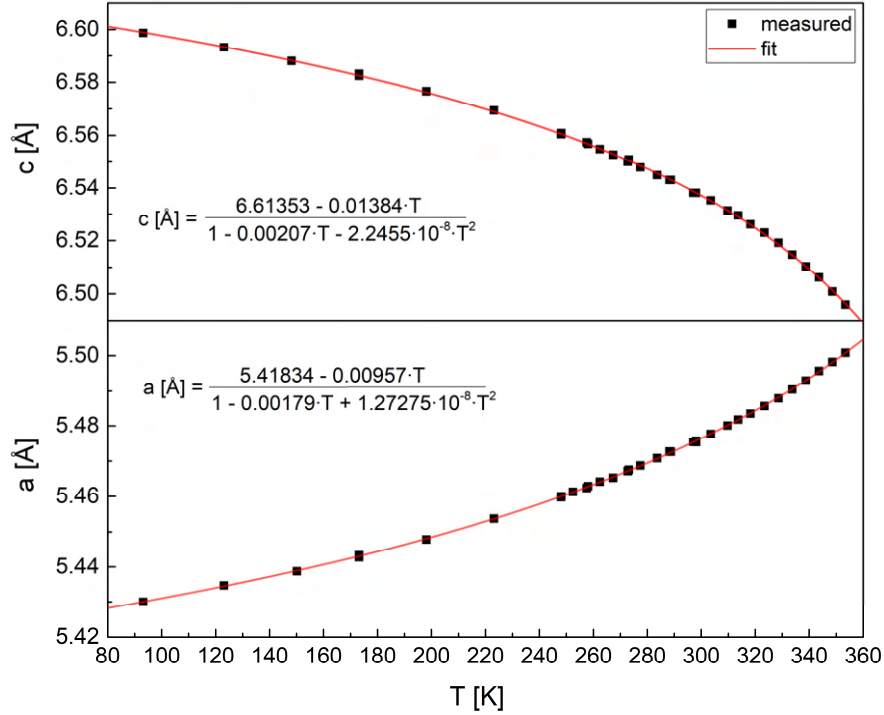


**Fig. 58:** Temperature evolution of the  $a$  and  $c$  lattice parameters of the non-modulated martensite of  $\text{Ni}_{53}\text{Mn}_{24}\text{Ga}_{23}$  single crystal and their fit with rational function. Measurements were performed using two diffractometers: PANalytical X'Pert diffractometer with custom-made heating/cooling stage in temperature range 245 – 360 K and Rigaku SmartLab equipped with then Anton Paar DCS 500 domed cooling stage in temperature range of 93 – 298 K.

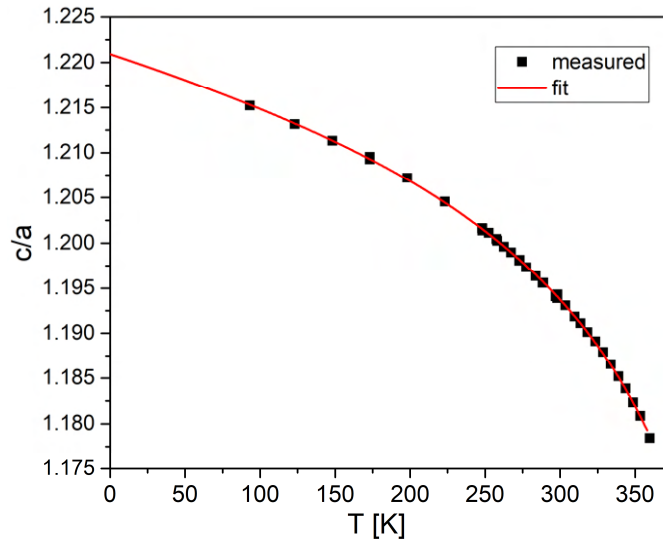


**Fig. 59:** Temperature evolution of the  $c/a$  ratio determined for the single crystal of  $\text{Ni}_{53}\text{Mn}_{24}\text{Ga}_{23}$ . Extrapolation down to 0 K is based on the approximation of  $c$  and  $a$  parameters with rational functions (**Fig. 58**).

Results served as one of the experimental keystones for the *ab-initio* study of the effect of electron localisation on prediction of material properties performed by M. Zelený of the VUT Brno, Czech Republic, published in [106]. The comparison between the extrapolated  $c/a$  ratio down to 0 K temperature and the *ab-initio* calculation once again proved the necessity to use the Coulomb repulsion parameter  $U$  when employing the Hubbard-model-based generalized gradient approximation for Ni-Mn-Ga. Comparison between our data and the predictions performed for the  $U$  interval from 0 to 3 eV restricted the appropriate interval of  $U$  to 1.4 – 2 eV. [106]

## 4.4 Characterisation of the 14M modulated martensite

During my stay at the LUT University (Finland) in the group of K. Ullakko and A. Sozinov, we have focused on the characterisation of the 14M modulated martensite of the  $\text{Ni}_{50}\text{Mn}_{25}\text{Ga}_{20}\text{Fe}_5$  alloy. 5 % Fe alloying was employed to bring the 14M martensite phase to the room temperature. Due to higher  $a/b$  ratio compared to the 10M martensite, one can get rid of  $a/b$  twins more easily in the 14M modulated martensite. This allows creation of the real single (martensite) variant state, favourable for the fundamental research.

Using the pseudo-austenitic coordinates, the lattice parameters at room temperature were determined as  $a = 6.194 \text{ \AA}$ ,  $b = 5.780 \text{ \AA}$ ,  $c = 5.499 \text{ \AA}$ ,  $\gamma = 90.55^\circ$  from 11 main reflections (i.e., (220), (022), (400), (040), (004), (440), (044), (620), (242), (224) and (422)). Modulation satellites were analysed with higher-resolution optics employing a hybrid monochromator to precisely determine the satellite positions and examine possible anomalies in their shape (despite expectation, they were not detected). The overall 2D map with all the analysed reflections is shown in **Fig. 60** in instrumental coordinates. Detailed high resolution maps of the detected satellites are shown in **Fig. 61**. The q-scan in reciprocal coordinates extracted from the RSM is shown in **Fig. 62**. Analysis proved that the modulation is commensurate with the modulation vector  $\mathbf{q} = 2/7 \mathbf{g}_{110}$ . Parts of these results served as a base for the publication [53].

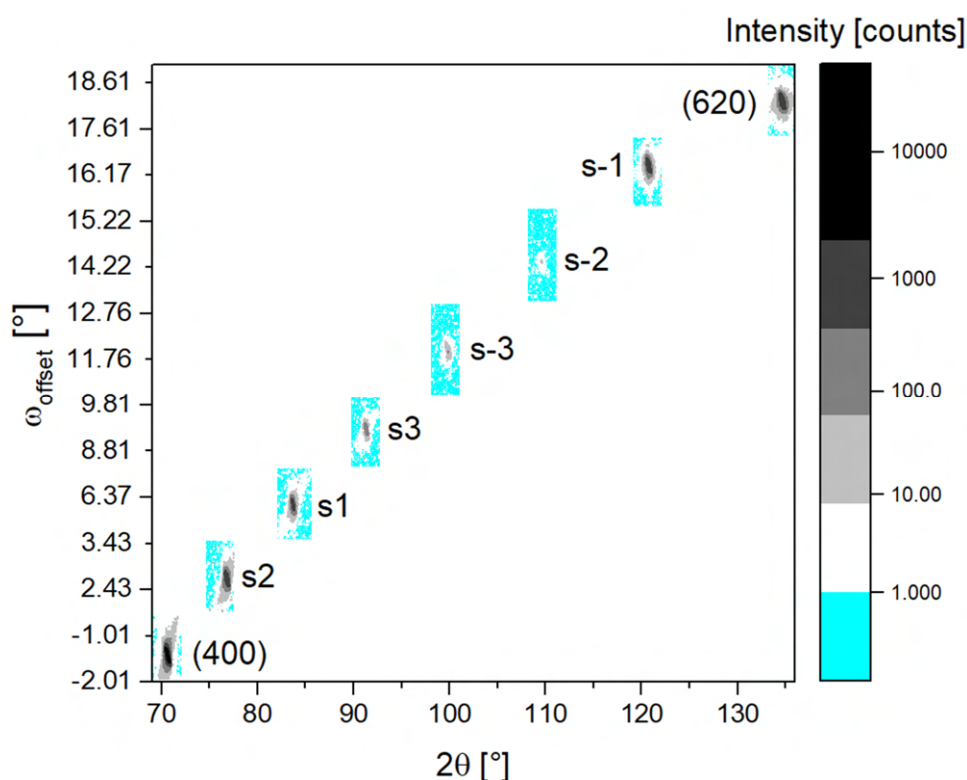


**Fig. 60:** The overall reciprocal space region between (400) and (620) reflections in instrumental coordinates measured for the  $\text{Ni}_{50}\text{Mn}_{25}\text{Ga}_{20}\text{Fe}_5$  single crystal. The azure highlighted regions represent the regions of the reciprocal space maps measured with higher resolution.

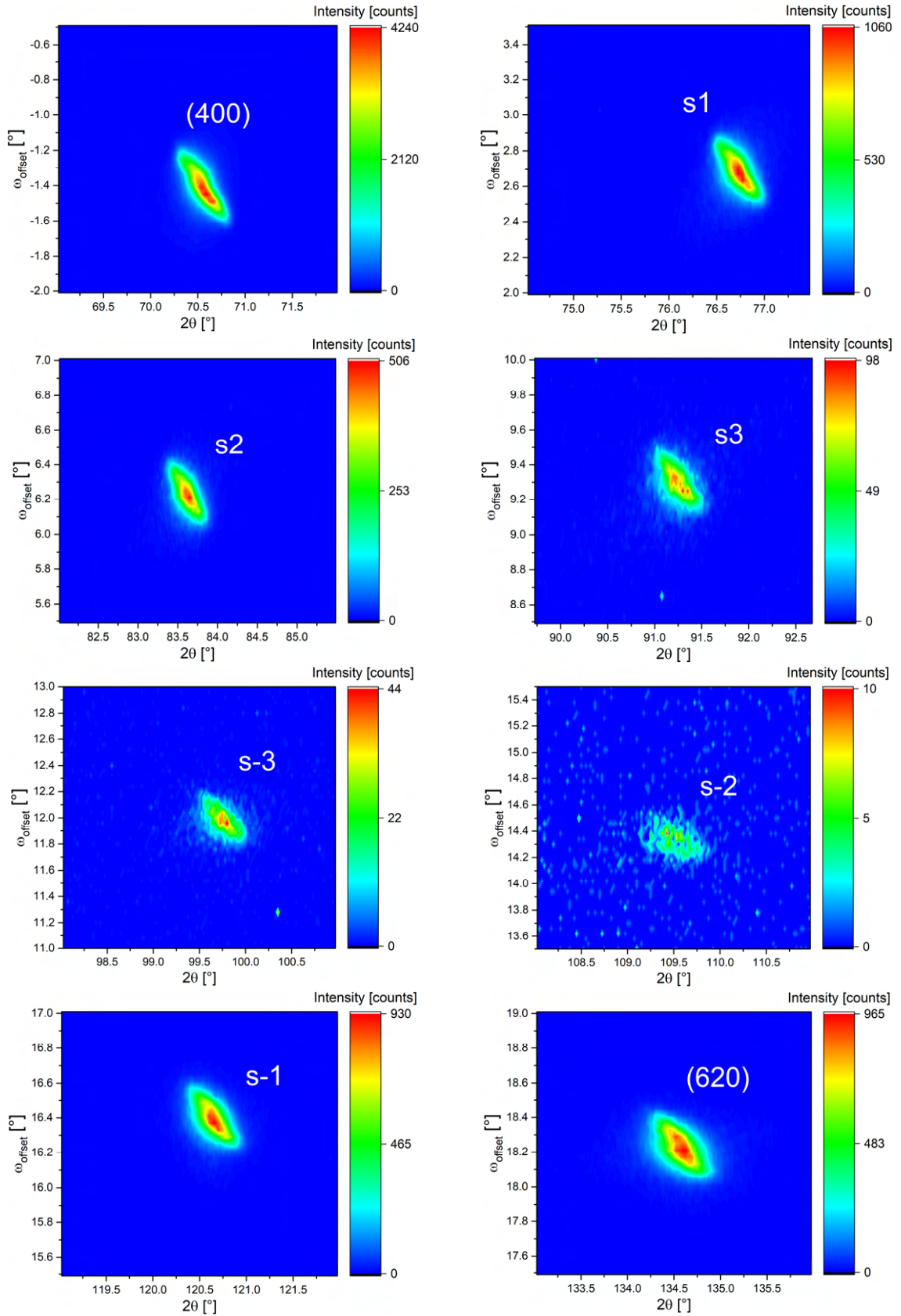


**Fig. 61:** Detailed 2D reciprocal space maps of the  $\text{Ni}_{50}\text{Mn}_{25}\text{Ga}_{20}\text{Fe}_5$  single crystal measured for the (400) and (620) reflections and the satellites in between presented in instrumental coordinates.

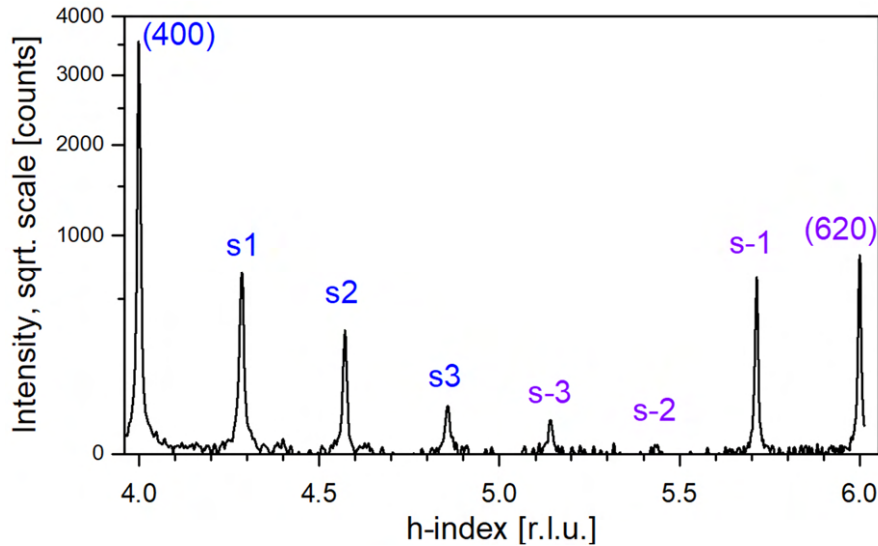


**Fig. 62:** The q-scan extracted from the RSM shown in **Fig. 60**. Satellite reflections are marked s1..s3 and s-1..s-3 depending on their order and direction from the main peaks.

Further proof of the commensurate modulation of our 14M martensites came from the ND measurements of the  $\text{Ni}_{50}\text{Mn}_{28.8}\text{Ga}_{22.2}$  alloy during cooling. Based on the measured q-scan at  $T = 180$  K, **Fig. 63**, modulation vector was determined as  $\mathbf{q} = 0.284(2) \mathbf{g}_{110}$ , which is equal to  $\mathbf{q} = 2/7 \mathbf{g}_{110}$  within measurement error. Further experiments in this field are currently underway, see chapter 5: Conclusions and outlook.

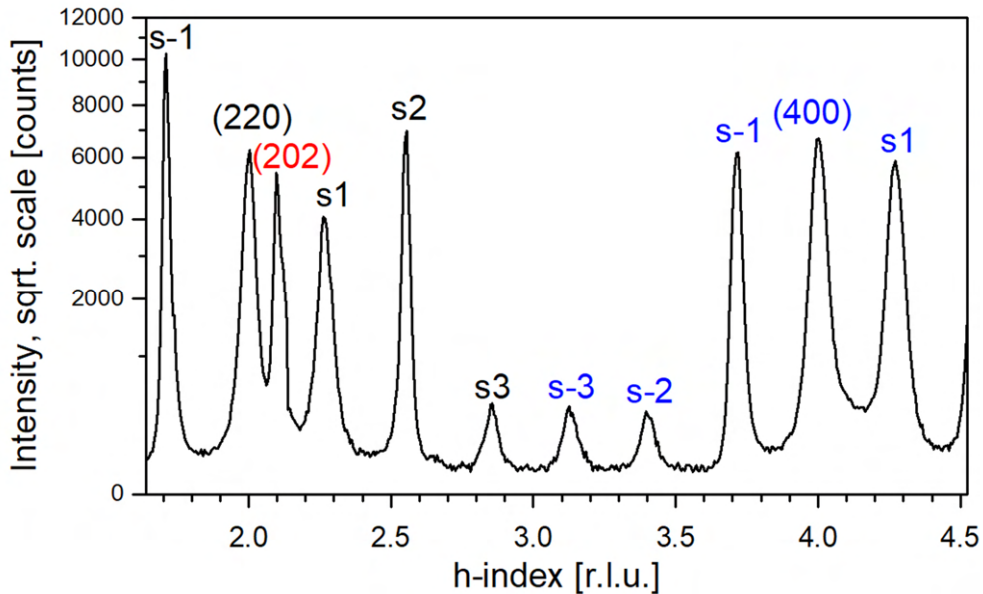


**Fig. 63:** q-scan measured for the  $\text{Ni}_{50}\text{Mn}_{28.8}\text{Ga}_{22.2}$  alloy during cooling at  $T = 180$  K with indexed reflections. Satellites of the (220) and (400) reflections are marked black and blue, respectively. Parasite (202) peak is present in the q-scan due to twinning.

## 4.5 Analysis of nanotwinned form of 10M martensite

In the first years of my doctoral studies, I took a part in research of structural evolution of the martensite close to the martensitic transformation. In the  $\text{Ni}_{50}\text{Mn}_{28.7}\text{Ga}_{21.3}$  single crystals, merging of  $(400)_{10\text{M}}$  and  $(040)_{10\text{M}}$  10M martensite reflections into one  $(400)_{10\text{M}'}$  reflection was discovered during the initial research of J. Drahokoupil and K. Fabianová in the temperature region close to the martensitic transformation ( $T_{10\text{M}-\text{A}} = 331 \text{ K}$ ). I analysed the evolution of the diffraction pattern in fine temperature steps, **Fig. 64**. Changes in the diffraction pattern exhibited thermal hysteresis. Nevertheless, the modulated character was conserved, as demonstrated in reciprocal space maps measured for both discussed states, **Fig. 65**. The newly discovered intermediate phase indicated by the peak merging was marked 10M' for clarity.

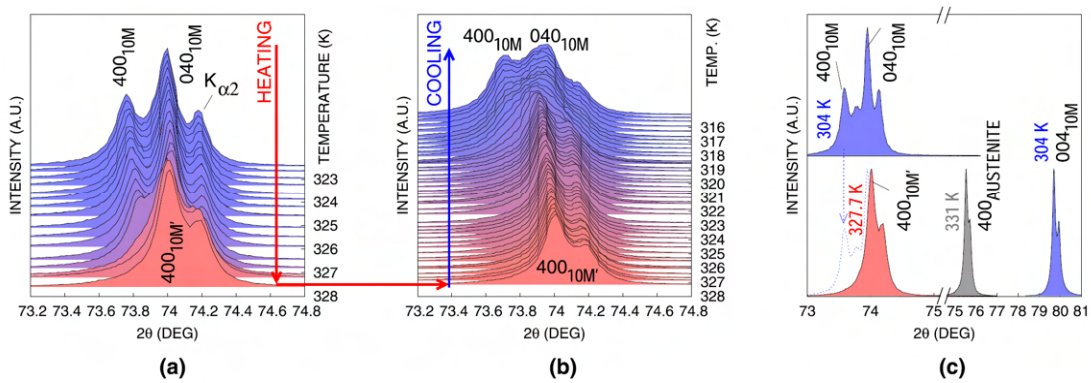


**Fig. 64:** Changes in the diffraction pattern of the  $\text{Ni}_{50}\text{Mn}_{28.7}\text{Ga}_{21.3}$  single crystal: Shifting of the  $(400)$  and  $(040)$  reflection as a function of temperature upon heating (a) and cooling (b) and selected XRD patterns at various temperatures (c): austenite  $(400)_{\text{A}}$ , 10M martensite  $(400)_{10\text{M}}$ ,  $(040)_{10\text{M}}$ ,  $(004)_{10\text{M}}$  and the  $(400)_{10\text{M}'}$  line from the intermediate 10M' martensite phase. [102]

Effect was initially explained by changes in crystal symmetry. Nevertheless, soon the changes in diffraction pattern were found to be connected to the refinement of the sizes of the  $ab$  twin domains: in the temperature region where the changes in diffraction patterns were observed, coarse  $ab$  twin domains scaled down to sizes of several tens of nm. [102] Connection between both effects was explained based on the diffraction theory of nanotwin superlattices proposed by Wang [123,124], where he presented, that refinement of the twin domains size leads to the presented diffraction effect due to the creation of apparently new average structure.

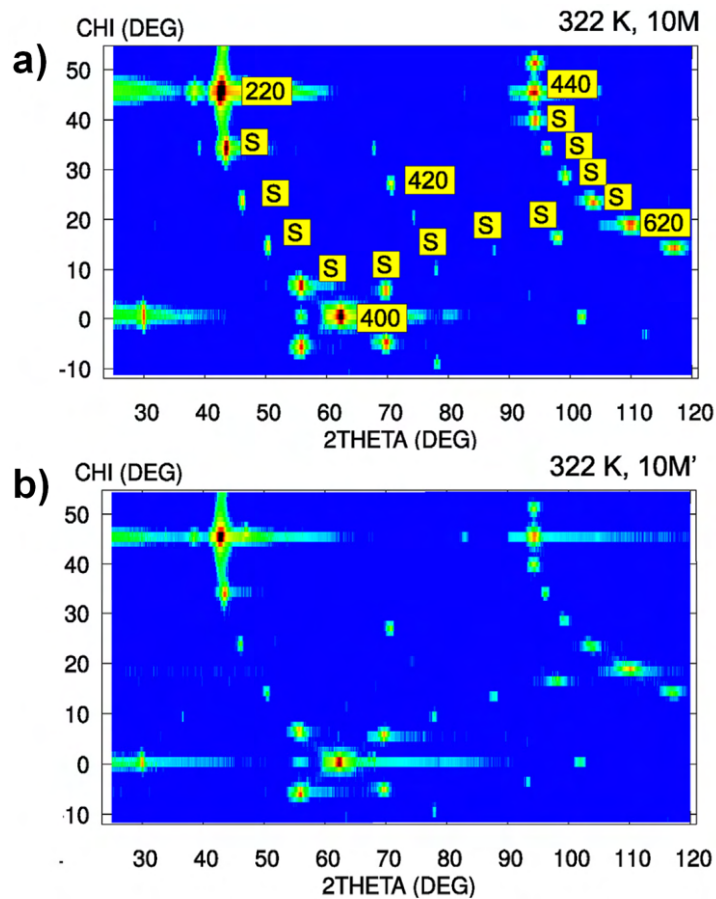


**Fig. 65:**  $2\theta$ - $\omega$ - $\chi$  reciprocal space maps in instrumental coordinates: a) 10M phase, b) intermediate 10M' phase. Both indicate standard 10M modulated phase. Adapted from [102]

Changes in the diffraction pattern in the region of (400) and (040) reflections were examined in detail and measured reflections were fitted using the advantage of FitExc, i.e., the full control of the fitting process with the possibility to fix some of the peak parameters or use the same values (such as width or shape) for multiple profiles. Representative examples of the fits in the temperature region of changes are shown in **Fig. 66**. From the fitted curves, integral intensities of each reflection, **Fig. 67**, and the lattice parameters of both 10M and 10M' phases were determined. Evolution of  $a$  and  $b$  lattice parameters (where changes were observed) and corresponding integral intensities are plotted in **Fig. 68**. Due to the overall low intensity of the  $(400)_{10M'}$  reflection in the lower temperature region, the error of the  $a_{10M'}$  lattice parameter is relatively large. Nevertheless, results indicated that both 10M and 10M' phases can coexist at the same temperature: thanks to the well-controlled fitting process, we were able to track minor contributions of the originating phases in a new one after transition, which was also demonstrated in **Fig. 66**.

To further examine the possible correlation with other physical properties, we measured the temperature evolution of the electrical resistivity, **Fig. 69**. Results indicated minor decrease in resistivity that strongly correlates with the presence of the nanotwinned 10M' phase. Based on this, possible channelling of the conductivity along the newly introduced twin boundaries can be speculated about.



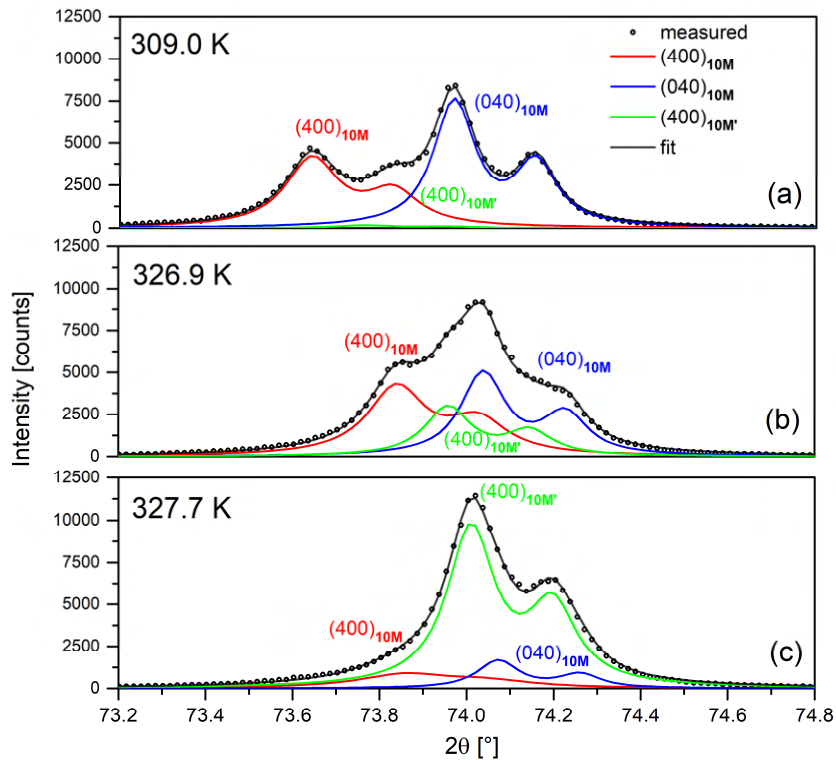


**Fig. 66:** Diffraction profiles measured at three selected temperatures. (a) At 309 K, two major reflections  $(400)_{10M}$  and  $(040)_{10M}$  are observable due to use of divergent geometry and the twinned microstructure. Including third reflection  $(400)_{10M'}$  originating from the nanotwinning led to a better fit. (b) At 326.9 K noticeable changes occur, the intensity of the  $(400)_{10M'}$  reflection increases significantly. (c) At 327.7 K, the  $(400)_{10M'}$  reflection is dominant while the  $(400)_{10M}$  and  $(040)_{10M}$  reflections are still present. [88]

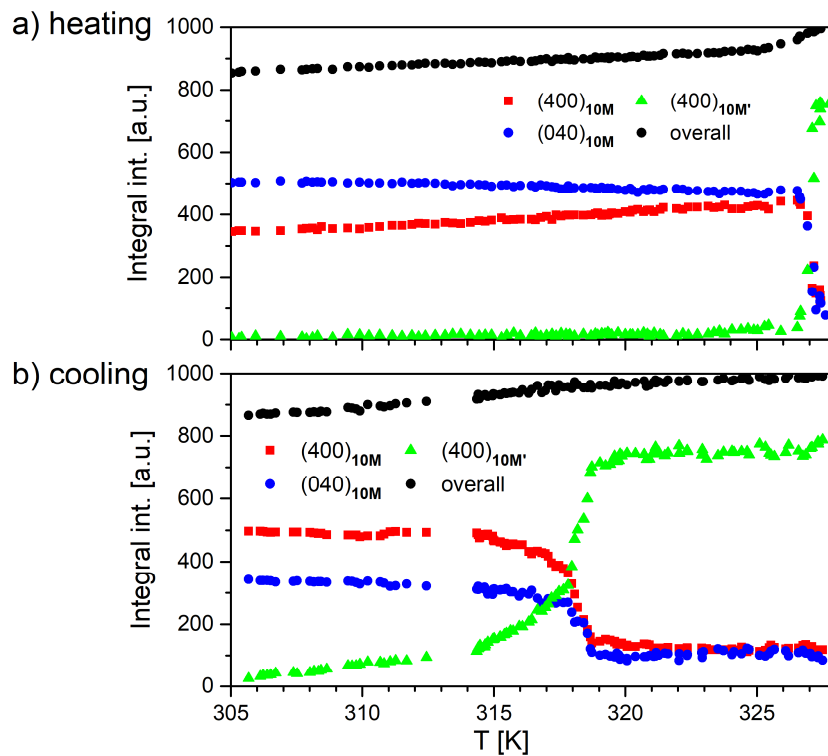


**Fig. 67:** Integral intensities of the observed reflections including the overall intensity during heating (a) and cooling (b). Original version was published in [88]

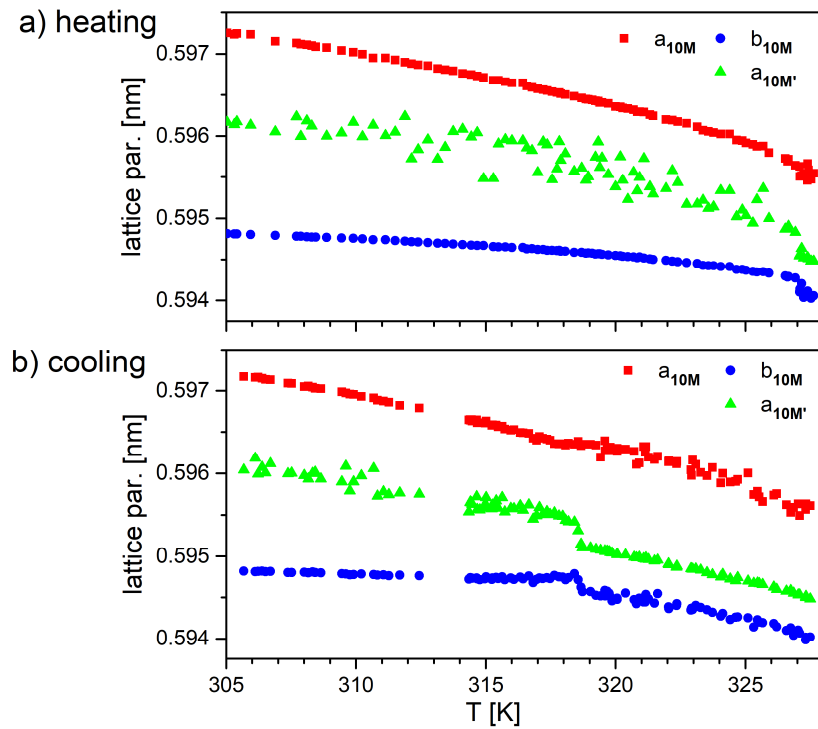


**Fig. 68:** Lattice parameters of the observed reflections during heating (a) and cooling (b). Original version was published in [88,102]

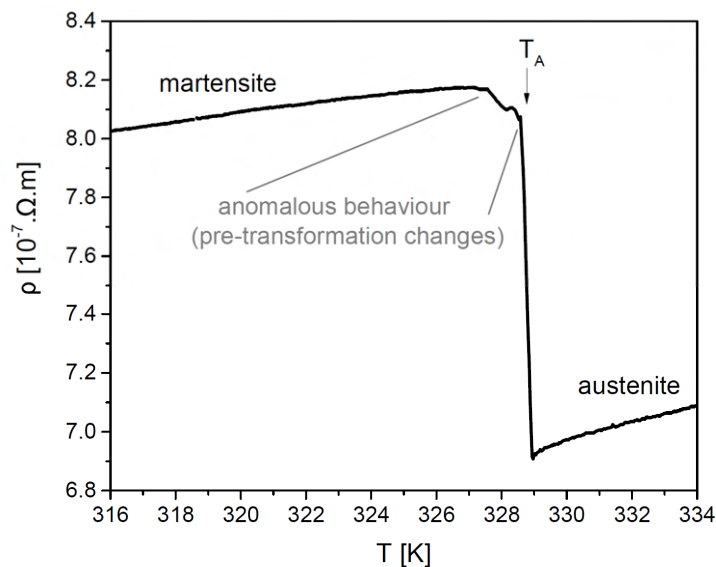


**Fig. 69:** Temperature evolution of the electrical resistivity reveals changes in the transport properties just before the transformation to the austenite ( $T_A$ ). [88]

Later, it was found that the nanotwinned form of 10M martensite was present in the broader range of  $\text{Ni}_{50}\text{Mn}_{25+x}\text{Ga}_{25-x}$  alloys, where  $2.6 < x < 3.5$  [105]. Surprisingly, unlike in the previous presented case, here the nanotwinned phase was stable in the lower temperature region, far from the austenite phase.

Altogether, our studies suggested that the nanotwinning presence in the microstructure can noticeably distort the diffraction patterns and false crystal symmetries can emerge. Therefore, for any structural study on Ni-Mn-Ga alloys, it is critical to recognize, whether the nanotwinning occurs or not. Results were published in [88,102,105].

## 4.6 Studies of the structural modulation within the 10M modulated martensite of Ni-Mn-Ga(-Fe) single crystals

The most fundamental topic of my doctoral studies was the study of the structural modulation of the 10M martensite in Ni-Mn-Ga-based single crystals possibly connected with the extreme mobility of the twin boundaries. Further motivated by the ongoing discussion regarding the nature of the modulation and the commensurate-incommensurate ambiguity (many conflicting reports previously discussed in chapter 1.5 can be found in the literature), I have investigated the structural modulation of multiple Ni-Mn-Ga(-Fe) single crystals of different compositions. Based on the diffraction studies and supported by magnetic measurements, electrical resistivity measurements, and known literature, selected suitable composition candidates for the studies have been chosen, following the requirement of the suitable temperature range of the 10M martensite stability. All the studies were carried out on large single crystals with proven MIR capability and highly mobile twin boundaries.

### 4.6.1 Hysteretic structural changes within 10M modulated martensite of Ni-Mn-Ga(-Fe)

As a base for our studies, I will first present the data obtained for the  $\text{Ni}_{50}\text{Mn}_{27}\text{Ga}_{22}\text{Fe}_1$  single crystal exhibiting a sequence of martensitic and intermartensitic transformations with the 10M martensite stable in the temperature range of 220 – 330 K (determined by the DC magnetic susceptibility (**Fig. 70**) and following XRD and ND studies).

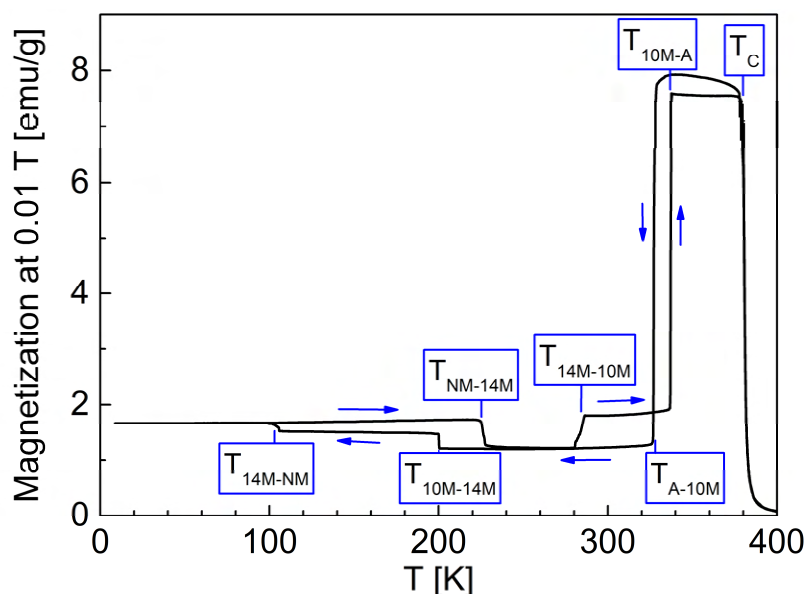


**Fig. 70:** DC magnetic susceptibility of the  $\text{Ni}_{50}\text{Mn}_{27}\text{Ga}_{22}\text{Fe}_1$  single crystal as a function of temperature. Transition temperatures (martensitic transformation, intermartensitic transformations and Currie point) are schematically marked. [109]

Following the usual monoclinic approximation using the lattice orientation inherited from the austenite [49,52,71], the lattice parameters of 10M martensite at the room temperature were  $a = 5.982 \text{ \AA}$ ,  $b = 5.945 \text{ \AA}$ ,  $c = 5.577 \text{ \AA}$ ,  $\gamma = 90.3^\circ$ .

The XRD experiments confirmed that the structure is modulated in the  $[110]^*$  direction. In the following description, we will stick to the previously introduced simpler notation using the magnitude of the modulation vector  $q$  defined by  $\mathbf{q} = q \mathbf{g}_{110}$ , where  $\mathbf{g}_{110}$  is the  $(110)^*$  reciprocal vector.

Given our case one-dimensional modulation of known direction, we have studied the  $q$ -scans between (400) and (620) reflections. Here I thank O. Pacherová of the FZU for the help with slightly quirky measurement software of the Bruker D8 Discover diffractometer.

Within the 10M stability region, two different patterns were found, **Fig. 71**. The *incommensurate* modulation with  $q = 0.416$   $\mathbf{g}_{110}$  was detected at room temperature ( $T = 298$  K). Upon heating, the pattern at  $T = 328$  K revealed *commensurate* 10M modulation with  $q = 0.400$ .

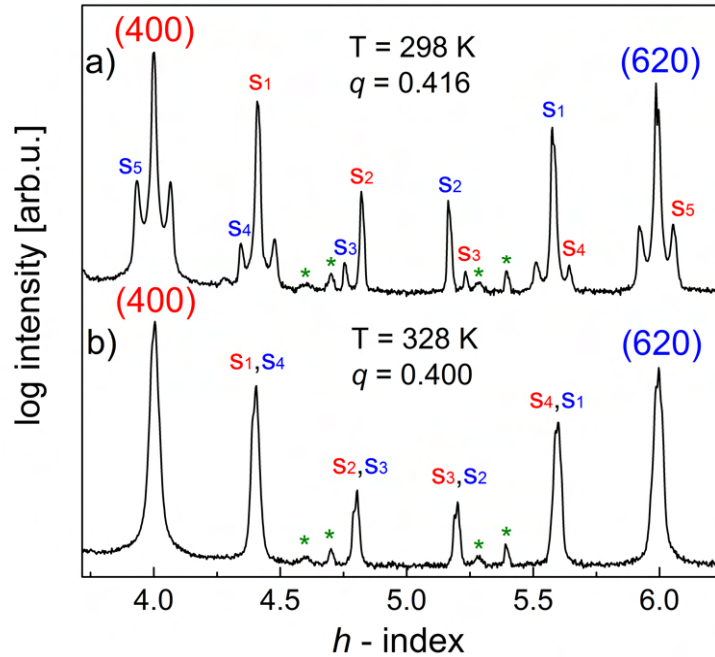


**Fig. 71:** q-scans in the  $[110]^*$  reciprocal direction determined by XRD for the  $\text{Ni}_{50}\text{Mn}_{27}\text{Ga}_{22}\text{Fe}_1$  single crystal. a)  $T = 298$  K (preceded by cooling to 260 K), b) after further heating to  $T = 328$  K. Equidistant modulation satellites  $s_1 \dots s_5$  belonging to (400) and (620) reflections are marked red and blue, respectively. Reflections from the polycrystalline sample holder are marked with green asterisks. [109]

To analyse the evolution of modulation in the whole temperature region of 10M martensite, we measured additional q-scans in smaller temperature steps during heating and cooling. We found that the shift of modulation satellites with temperature exhibits hysteretic behaviour. At  $T = 220$  K (few kelvins above the transition from 10M to 14M martensite,  $T_{10\text{M} \rightarrow 14\text{M}}$ ), the structure exhibited another (pseudo)*commensurate* state with  $q = 0.428(2) \sim 3/7$ . During following heating,  $q$  decreased, reaching  $q = 0.416(1)$  at room temperature and further decreased to  $q = 0.400(1)$  at 328 K (the aforementioned *commensurate* modulation). Surprisingly, during the following cooling, the modulation remained *commensurate*, but started to change again at  $T = 290$  K. Described hysteretic behaviour in the evolution of the diffraction patterns during thermal cycling is demonstrated in **Fig. 72**. [109]

As the XRD measurements are only sensitive to the surface layer (the effective penetration depth of X-ray in our sample is  $D_{99\%} \sim 15 \mu\text{m}$  for Cu radiation), the necessity of bulk-sensitive measurements was imminent and we applied for beam time in ILL Grenoble. There, we collaborated closely with M. Klicpera of MFF CUNI, who is an experienced expert on ND.

Our ND diffraction measurements performed with the instruments D9, D10 and CYCLOPS confirmed unambiguously the changes in modulation within the whole sample volume. The evolution of the satellite peaks followed the previously described scheme, illustration of the two obtained q-scans is shown in **Fig. 73**. All the neutron data were processed following the procedure described in chapter 3.3. For each temperature step, the resulting q-scans were fitted and the value of  $q$  was calculated. It was found that continuously  $q$  covers the range of  $2/5 - 3/7$  from which only distinct parts have been described previously in the literature. The development of  $q$  measured by ND shows an excellent agreement with XRD. The evolution of  $q$  with temperature is summarised in **Fig. 74**.

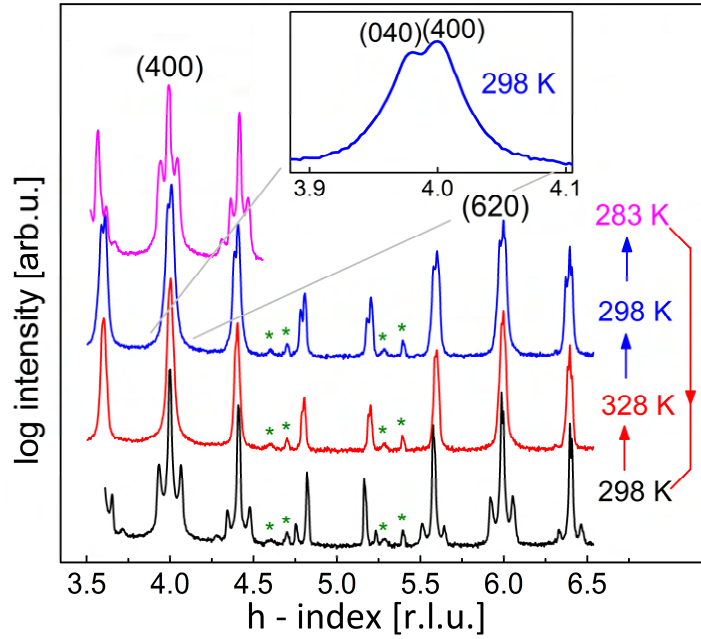


**Fig. 72:** Evolution of the XRD diffraction pattern during thermal cycling as seen in q-scans along  $[110]^*$  reciprocal direction. Owing to the  $ab$  twinning, both (400) and (040) reflections were present in the q-scans (zoomed in the inset). Reflections from the polycrystalline sample holder are marked with green asterisks. [109]

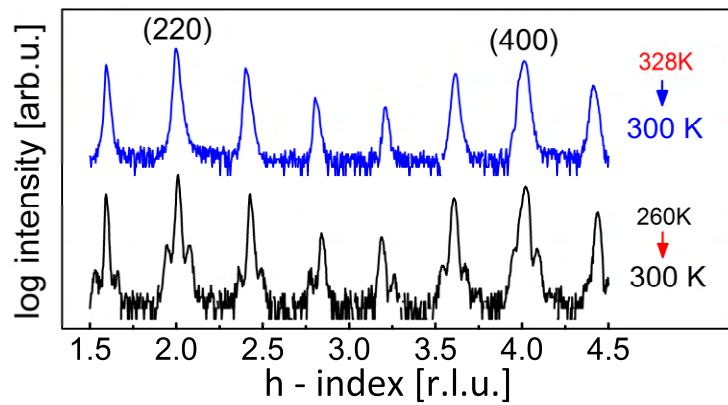


**Fig. 73:** Two typical ND q-scans obtained at  $T = 300$  K after different temperature history. Blue curve represents the measurement after heating to 328 K. Black curve represents the measurement after cooling to 260 K. [109]

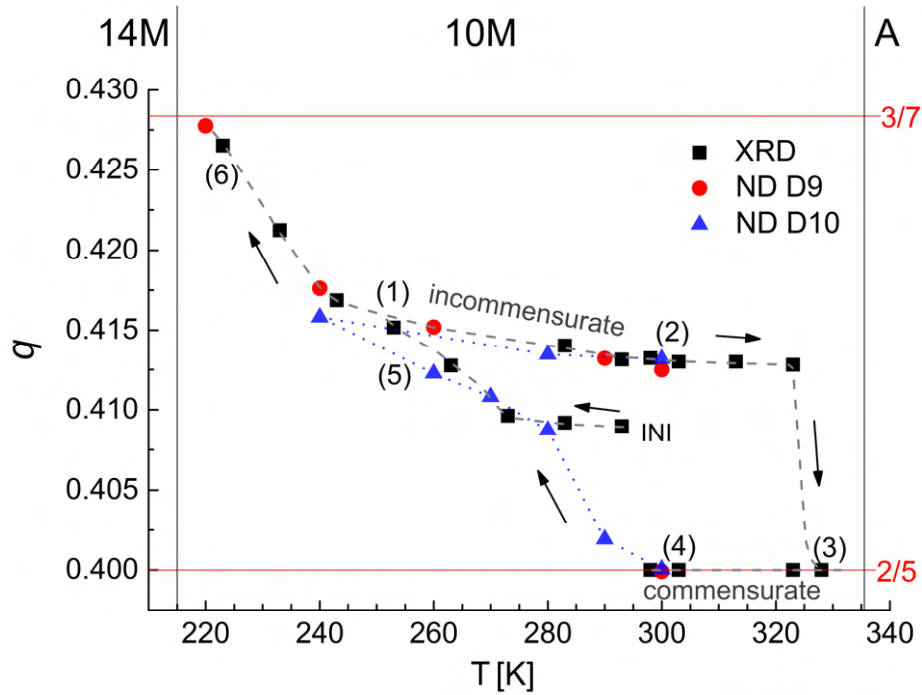


**Fig. 74:** Magnitude of the modulation vector  $q$  as a function of temperature determined for the  $\text{Ni}_{50}\text{Mn}_{27}\text{Ga}_{22}\text{Fe}_1$  single crystal. Black squares represent data from the XRD measurement, red circles and blue triangles stand for ND measurements on D9 and D10. Dotted and dashed lines connecting symbols serve purely as guides for the eyes. The arrows depict the sample heating/cooling cycles. Numbers in brackets refer to the SEM micrographs later shown in **Fig. 78**. The point marked INI corresponds to the initial undefined state of the sample. [109]

#### 4.6.2 Additional diffraction analysis

Complementarily to the  $q$ -scans,  $2\theta$ - $\omega$  scans were measured by the XRD. Measurement indicated refinement of the  $a/b$  twins down to nanoscale with decreasing temperature. Such refinement was detected by the observed merging of  $(400)_{10M}$  and  $(040)_{10M}$  reflections present in the single scans of commensurate phase into only one reflection  $(400)_{10M}$ , detected in the incommensurate phase. Such behaviour was detected earlier in  $\text{Ni}_{50.0}\text{Mn}_{28.7}\text{Ga}_{21.3}$  [88,102] and was discussed in chapter 4.5.

Furthermore, several follow-up neutron measurements were performed to further analyse the nature of the modulation. **Fig. 75** represents a wider  $q$ -scans measured by Dr. Klicpera with the IN3 experiment in *ILL*. Here the diffuse signal close to the first-order satellites of the  $(220)$  and  $(2-20)$  reflections indicates possible changes in the short-range order. Even though the sample was in random state, such finding once again proves the possible changes in the stacking, probably in the form of  $a/b$  nanotwinning in the structure/microstructure.

Rather interesting is the amount of the detected satellite reflections of relatively high intensity. Nevertheless, all of them can be indexed with respect to the main reflections with the use of the single aforementioned modulation vector. Even though the satellites of more than 3<sup>rd</sup> order are very rare in ordinary crystals, satellites of up to 9<sup>th</sup> order were reported in some specific cases [125,126]. Additional research in this direction is currently underway, see chapter 5 for details.

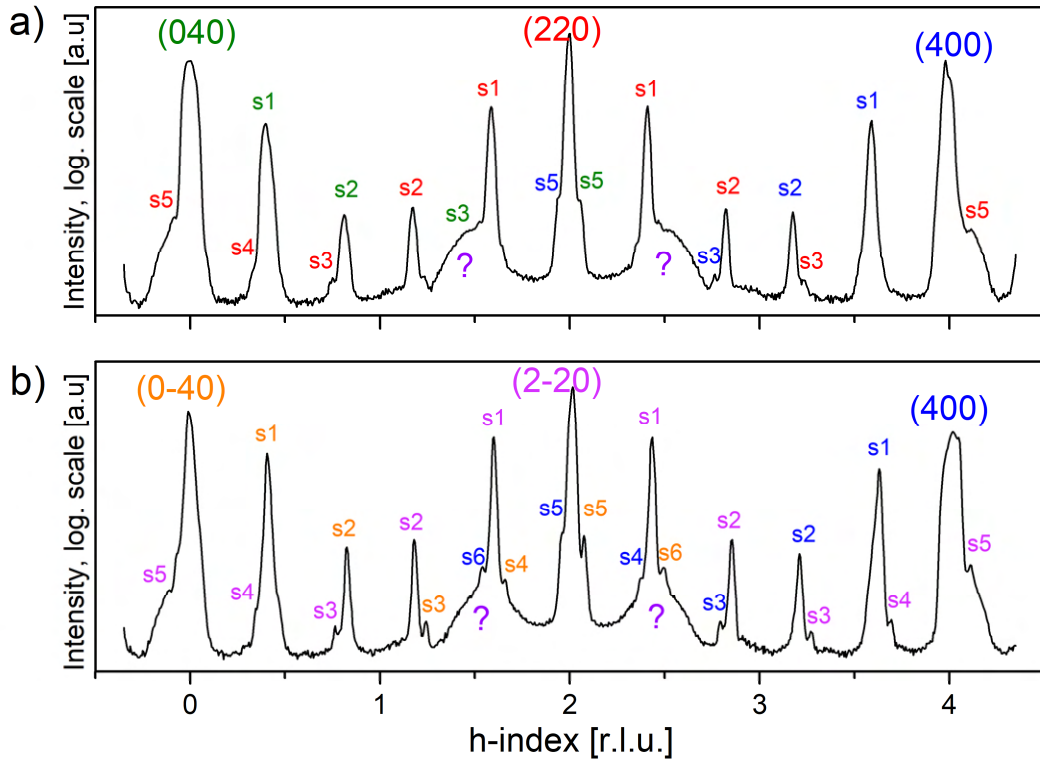


**Fig. 75:** Two  $q$ -scans of the  $\text{Ni}_{50}\text{Mn}_{27}\text{Ga}_{22}\text{Fe}_1$  single crystal measured with the IN3 diffractometer: a) in the  $(-110)^*$  direction and b) in the  $(110)^*$  direction. Broad peaks around the first order satellites of the  $(220)$  and  $(2-20)$  reflection indicate changes in short-range order.

#### 4.6.3 Relation of the minor changes of the structural modulation to other physical properties

To check the effect of the detected hysteretic changes in the structural modulation on other physical properties, electrical resistivity and elastic properties of the very same sample of the  $\text{Ni}_{50}\text{Mn}_{27}\text{Ga}_{22}\text{Fe}_1$  single crystal were examined in the temperature region of subtle modulation changes.

In the resistivity curve, gradual changes in conductive properties during the temperature evolution of the 10M martensite were observed after the subtraction of the metallic linear contribution, **Fig. 76**. Changes exhibited hysteretic behaviour very similar to that of the  $q$  with temperatures matching those from the diffraction experiments. [109]

Additional insight was obtained thanks to the fruitful collaboration with group of H. Seiner, who analysed our sample by the resonant ultrasound spectroscopy (RUS). After careful measurements of the RUS spectra and tracing of the resonant modes, we were able to again observe the similar hysteresis in the effective elastic modulus of the lowest detected resonant mode present throughout the whole temperature range of 10M existence, **Fig. 77**, [109]. Furthermore, no discontinuous changes of the microstructure or the elastic constants have been indicated by the measurement, excluding a presence of a first-order phase transition within the analysed temperature region.

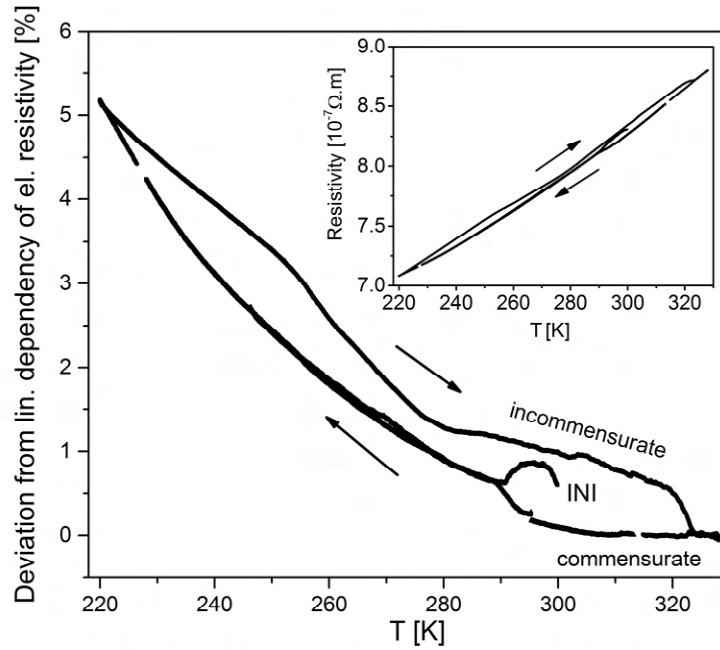


**Fig. 76:** Deviation from the linear dependency of electrical resistivity as a function of temperature measured for the  $\text{Ni}_{50}\text{Mn}_{27}\text{Ga}_{22}\text{Fe}_1$  sample. The points marked INI correspond to the initial undefined state of the sample. Inset: Full measured temperature evolution of the electrical resistivity before extraction of the linear trend. [109]

The RUS showed that the commensurate phase has some very soft shearing modes that are significantly stiffening with increasing incommensurateness. The soft modes in the commensurate phase are strongly dissipative, causing high damping of the RUS spectrum. Altogether, the RUS measurements suggest that the commensurate structure is much less stable than the incommensurate one, and that the commensurate state may be just a metastable form of 10M martensite, that appears only close to the martensitic transformation temperature. This structure tends to transform into more irregular but more stable structure. [109]

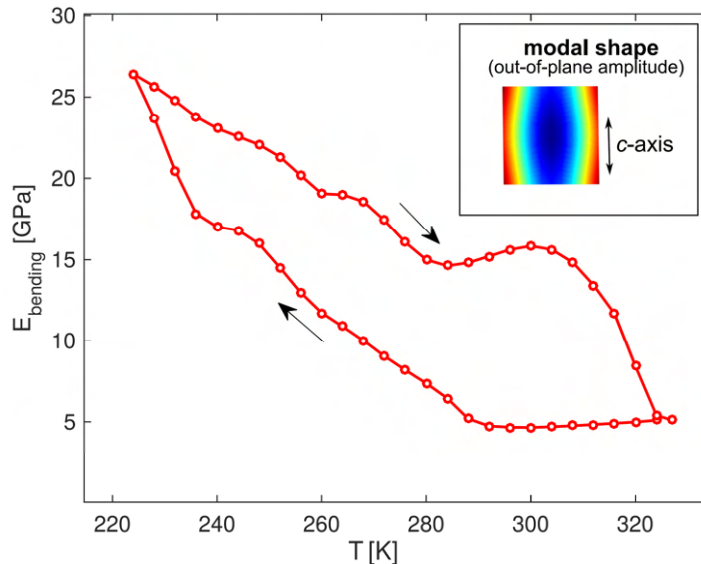


**Fig. 77:** Temperature evolution of an effective (mode-specific) elastic modulus for the field-cooled  $\text{Ni}_{50}\text{Mn}_{27}\text{Ga}_{22}\text{Fe}_1$  sample, calculated from the temperature evolution of the lowest detected resonant mode. The inset shows the corresponding modal shape and its orientation with respect to the dominant c-axis direction in the sample. Measurement and analysis done by H. Seiner. [109]



#### 4.6.4 Relation to the $a/b$ twinned microstructure

Merging of the (400) and (040) peaks suggested the refinement of the  $a/b$  twin domains (mentioned earlier in 4.6.2 and in detail discussed in chapter 4.5). In collaboration with L. Klimša of the FZU, we have analysed the  $a/b$  laminate in the region of the hysteretic behaviour of the modulation vector.

The SEM micrographs, **Fig. 78**, clearly showed that the  $a/b$  twin domains become finer in the temperature regions of the incommensurate modulation (mean width of the  $a/b$  twin domains was about 20 nm), while they become coarser for the commensurate case (mean width of  $\sim 150$  nm).

This indeed indicates that  $a/b$  nanotwinning previously discussed for our alloys is involved. Our measurements and observations suggest that the microstructure evolves by additional nanotwinning during cooling, introducing more  $a/b$  twin boundaries and new stacking faults. Both behave as obstacles for electronic transport, and, thus, increased electrical resistivity is detected on cooling.

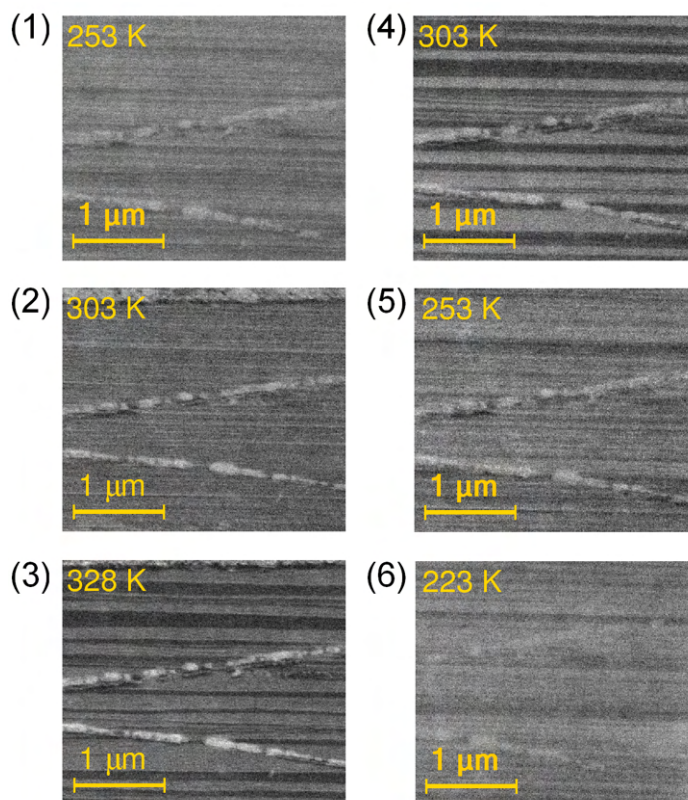


**Fig. 78:** SEM micrographs of the  $a/b$  twin domains. Numbers correspond to the points in the  $q$ -scan shown in **Fig. 74**.

#### 4.6.5 Follow-up neutron modulation studies of other stoichiometries

We performed similar studies for additional Ni-Mn-Ga(-Fe) alloys of various stoichiometries.

The single crystal of  $\text{Ni}_{50}\text{Mn}_{27.7}\text{Ga}_{22.3}$  was measured with the D10 instrument in ILL. This stoichiometry represents an interesting case for fundamental study as this alloy does not undergo any intermartensitic transformation. Our crystal exhibited slightly *incommensurate* modulation with  $q = 0.402(1)$  at 300 K (few kelvins below the martensitic transformation). During cooling, the  $q$  started to increase and below 150 K it almost stabilised at  $q = 0.416(1)$ . No further evolution was observed down to 10 K. During ongoing heating up from 10 K to 300 K, slight hysteretic behaviour was detected, **Fig. 79**, and confirmed by minor changes in neutron Laue patterns from CYCLOPS.

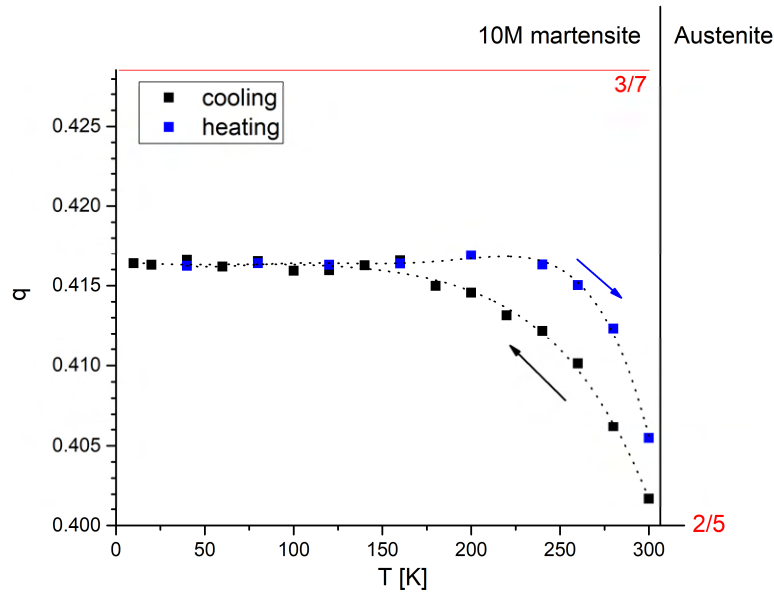


**Fig. 79:** Magnitude of the modulation vector  $q$  as a function of temperature during cooling (black) and heating (blue) determined for the  $\text{Ni}_{50}\text{Mn}_{27.7}\text{Ga}_{22.3}$  single crystal. Dotted lines connecting symbol serve purely as guides for the eyes. The arrows depict the sample heating/cooling cycle. Black vertical line represents the temperature of MT.

Similar results were obtained for the  $\text{Ni}_{50}\text{Mn}_{28.1}\text{Ga}_{21.9}$  measured with the D9 instrument, **Fig. 80**. The similar behaviour was expected, since the composition is close to that of the previously discussed alloy. Here, we managed to cool the sample down to 2 K. The measurement again indicated stabilisation of the modulation vector with  $q = 0.415(1)$  at 2 K.

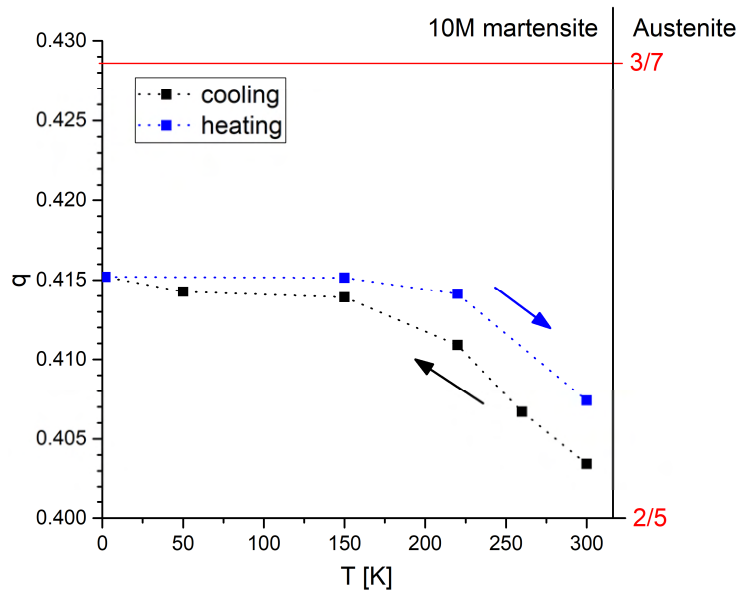


**Fig. 80:** Magnitude of the modulation vector  $q$  as a function of temperature during cooling (black) and heating (blue) determined for the  $\text{Ni}_{50}\text{Mn}_{28.1}\text{Ga}_{21.9}$  single crystal. Dotted lines connecting symbol serve purely as guides for the eyes. The arrows depict the sample heating/cooling cycles. Black vertical line represents the temperature of MT.

Another single crystal of  $\text{Ni}_{50}\text{Mn}_{25}\text{Ga}_{21}\text{Fe}_4$  exhibited *incommensurate* modulation with  $q = 0.421(1)$  at 300 K.  $q$  slightly decreased to  $0.420(1)$  upon heating to 315 K (although the change is within the error, the slight change in the modulation satellites positions was detected). Unfortunately, we were not able to reach higher temperatures due to the instrumental limitations. During cooling, the  $q$  increased, reaching  $q = 0.428(1) \sim 3/7$  just before the intermartensitic transformation to 14M modulated martensite, **Fig. 81**.

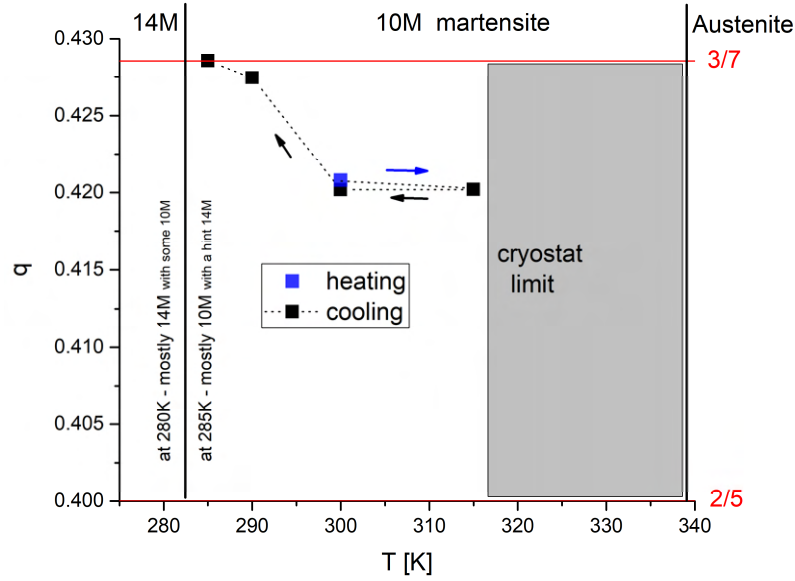


**Fig. 81:** Magnitude of the modulation vector  $q$  as a function of temperature during cooling (black) and heating (blue) determined for the  $\text{Ni}_{50}\text{Mn}_{25}\text{Ga}_{21}\text{Fe}_4$  single crystal. Dotted lines connecting symbol serve purely as guides for the eyes. The arrows depict the sample heating/cooling cycles. Vertical lines represent the MT and IMT.

#### 4.6.6 Summary of the modulation studies

- We confirmed unambiguously that the modulation continuously changes within the 10M modulated martensite in the  $q \in (2/5 - 3/7)$  interval. We have found a specific composition for which the magnitude of the modulation vector covers this entire interval. This means that the modulation in our 10M martensite can indeed be commensurate ( $q = 2/5$ ), incommensurate ( $q$  irrational) or, following nomenclature of Righi et al. [71], even pseudo-commensurate ( $q = 3/7$ ).
- We have discovered the hysteretic behaviour of the commensurate-incommensurate transition.
- Using neutron diffraction, we confirmed that the modulation evolution is a true bulk effect.
- We believe to be the first who provided thorough study of the evolution of the modulation vector within 10M modulated martensite using single crystal samples, especially in such fine steps in temperature. Thanks to the single-crystal measurements, we were able to observe previously unreported satellites. We studied samples in the state relevant to the applications of the MIR effect.
- Based on own measurements on alloys of various compositions and based on our thorough literature study, we present the hypothesis, that described changes in the modulation vector within the 10M modulated martensite are common for a wide range of Ni-Mn-Ga(-Fe) compositions, probably even for all those that undergo the Austenite  $\rightarrow$  10M  $\rightarrow$  14M sequence on cooling. We have found an interesting metastable state with  $q \sim 0.416$  in our alloys, even in those where no intermartensitic transformation to 14M occurs (sample stays in 10M martensite down to the lowest temperatures).

The above mentioned results were published in [107,109]. I also presented these results at the relevant international scientific conferences, such as JEMS 2019 (Joint European Magnetic Symposia, Uppsala, Sweden), IUCr 2021 (25th Congress of the International Union of Crystallography, Prague, Czech Republic) and ICOMAT 2022 (16th International Conference on Martensitic Transformation, virtual, South Korea).

## 5 Conclusions and outlook

The focus of my thesis is the characterisation of the Ni-Mn-Ga-based Heusler alloys exhibiting the MT and consequently the MSM effects, especially the MIR. The main conclusions are:

*i)* The structure of the new samples of the Cu-, Cr- and Fe-alloyed Ni<sub>2</sub>MnGa-based alloys has been identified despite their complicated form. The determined phase composition, lattice parameters and single/oligo/poly-crystalline nature served as one of crucial bases in the research of systematic trends of structure, microstructure, and physical properties of the Ni-Mn-Ga-based alloys upon alloying with different elements. Detected strong fibre texture of the Ni-Mn-Ga-Fe-Cu samples suggested their possible application potential even in the polycrystalline form.

*ii)* Crystal quality of the four single crystals obtained from the four different producers has been characterised, mainly by crystal mosaicity. The result showed that the crystal quality affects the magnitude of the twinning stress (obtained by mechanical testing) only indirectly, through its impact on the character of the twin boundaries.

*iii)* The temperature evolution of the lattice parameters of the non-modulated martensite of Ni-rich Ni-Mn-Ga single crystal down to 93 K was analysed to obtain the *c/a* ratio at 0 K. Obtained extrapolated value served as one of the proofs of the need of Coulomb repulsion parameter *U* when employing the Hubbard-model-based generalized gradient approximation for Ni-Mn-Ga.

*iv)* The XRD studies of the modulation satellites of the 14M modulated martensite of Ni<sub>50</sub>Mn<sub>25</sub>Ga<sub>20</sub>Fe<sub>5</sub> single crystal in collaboration with K. Ullakko and A. Sozinov group proved the commensurate nature of the modulation of this phase. This was also confirmed by our ND experiment performed on Ni<sub>50</sub>Mn<sub>28.8</sub>Ga<sub>22.2</sub> alloy.

*v)* Evolution of the diffraction pattern of the 10M modulated martensite near the martensitic transformation was examined. Observed merging of the reflections from the twin domains suggested nanotwinned character of the 10M modulated phase near austenite.

*vi)* Thorough studies of the evolution of the structural modulation of the 10M modulated martensite with temperature resulted in detection of the commensurate-incommensurate transition upon cooling. Transition exhibited a thermal hysteresis. The evolution of the modulation was studied in fine temperature steps and, importantly, the studies were performed on the single crystal with extremely mobile twin boundaries. Observed changes in the modulation vector were correlated with the changes in transport and elastic properties and the changes in the twinned microstructure. Here, presence of nanotwinning previously suggested by XRD was confirmed by SEM.

*vii)* Performed studies suggest that the commensurate 10M state is a metastable state of martensite that evolves through the nanotwinning to more irregular but more stable incommensurate state. Follow-up studies on additional samples of other compositions proved that this behaviour is universal to wide range of Ni-Mn-Ga(-Fe) compositions. The changes in the modulation vector are schematically illustrated in **Fig. 82**. With this, we gave the answer to the long-rooted *commensurate – incommensurate – pseudo-commensurate* ambiguity.

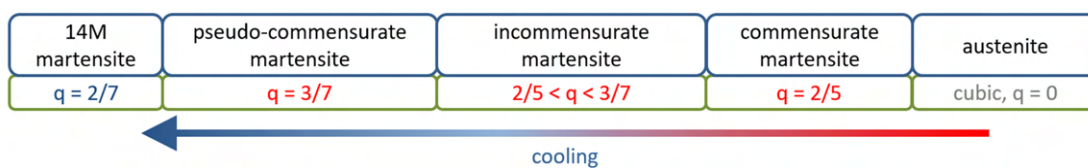


**Fig. 82:** Schematic depiction of the changes in structural modulation around the temperature region of the 10M martensite in the Ni-Mn-Ga(-Fe) alloys.

Selected results were presented on relevant scientific conferences and the majority was published in impacted scientific journals. The list of my publications relating to the doctoral thesis is presented at page 104.

The findings on evolution of the structural modulation have been discussed with the leading experts of the field of aperiodic crystallography during the 5<sup>th</sup> International School on Aperiodic Crystals (May 2022, Kutná Hora, Czech Republic). Based on that, follow-up studies on dedicated single-crystal *SuperNova* (Rigaku Oxford Diffraction) diffractometer are currently underway. For these we chose the Ni-Mn-Ga single crystal that undergoes the full sequence of transformations. The main aim of the studies is to further clarify the structural changes in the described region of continuous evolution within the 10M martensite, especially to address the high intensity of the modulation satellites of high orders. Further focus will be given on the changes in the structure and twinned microstructure upon the intermartensitic transformations and on addressing the ambiguity in the reported crystal symmetries.

Moreover, computational analysis of the unusually high intensity of the high-order satellites is currently underway in the collaboration with L. Straka. It suggests strongly anharmonic character of the modulation function, similarly to the case recently described in the incommensurately modulated  $\text{Rb}_2\text{ZnCl}_4$  [127]

# Appendix I: General introduction into structural modulation

The additional complexity of martensite originates from the *modulation* of particular martensite phases. The structure of the ideal crystals can usually be described by their translational symmetry – the crystal lattice consists of identical cells filled identically with the same particles. In some materials (such as Ni-Mn-Ga-based alloys), there might appear phases with an additional subtle long-range order – the *modulation*. In modulated crystals, the arrangement of the particles slightly differs along the different crystallographic cells (e.g., the atoms are slightly shifted from their positions) and such changes can be described by the modulation function superimposed on the original unit cell. To accompany the modulation into the description, superspace approach is usually applied. [128,129] The diffraction vector  $\mathbf{H}$  then has slightly more complicated form of

$$\mathbf{H} = h\mathbf{a}^* + k\mathbf{b}^* + l\mathbf{c}^* + m\mathbf{q}, \quad (2)$$

where  $h, k, l$ , and  $m$  are integers,  $\mathbf{a}^*, \mathbf{b}^*, \mathbf{c}^*$  reciprocal space vectors and  $\mathbf{q}$  is the modulation vector that could be written as

$$\mathbf{q} = \alpha\mathbf{a}^* + \beta\mathbf{b}^* + \gamma\mathbf{c}^*, \quad (3)$$

where  $\alpha, \beta$  and  $\gamma$  are real numbers. There might even exist more complex cases of modulation involving the superposition of multiple modulation vectors. [128,129]

The modulation is called *commensurate* when all the numbers  $\alpha, \beta$ , and  $\gamma$  are rational. In such a case, the crystal structure can be described by a new crystal lattice consisting of larger unit cells, i.e., the crystal consists of the identical sections of modulated original cells, **Fig. 83 b**).

If at least one of the numbers  $\alpha, \beta$ , and  $\gamma$  is irrational, the modulation is called *incommensurate*. In such a case, the periodicity of the modulation does not belong to the periodicities of the basic structure and the set of positions originating from the equation (2) does not form a lattice. [129] Crystal loses translational symmetry. Such structure is no longer periodic in three-dimensional space, nevertheless, it is still fully ordered, and it can still be described using the originating cell and the superimposed modulation, **Fig. 83**.

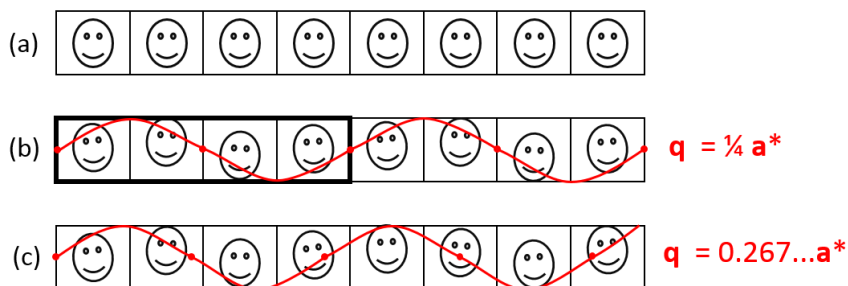


**Fig. 83:** Illustration of the structural modulation: a) Ideal crystal consisting of the identical cells. b) Commensurate structure with the hypothetical red modulation function. For clarity, the points with zero amplitude are marked with red dots. The new lattice consisting of the larger unit cell (bold frame) can be defined. c) Incommensurate structure.

Structural modulation is manifested in the diffraction pattern of the crystal by additional Bragg reflections called *modulation satellites* that surround the main reflections at distances  $\pm m\mathbf{q}$ . Satellite reflections are usually much weaker than the main reflections if the amplitude of the modulation is

small. Furthermore, the intensities of the satellites usually decrease with increasing order  $m$ . Nevertheless, several exceptions have been found. [125]

Demonstration of the simulated theoretical diffraction pattern originating from hypothetical commensurate and incommensurate modulation are shown in **Fig. 84** and **Fig. 85**, respectively. Satellite reflections of the 1<sup>st</sup> and 2<sup>nd</sup> order have been drawn. Figures demonstrate the overlap of the modulation satellites of the second order in the presented case of commensurate modulation. With increase in the magnitude of the modulation vector, satellite positions shift and the overlap is no longer present. Both cases are very similar to the cases detected in the 10M modulated martensite of Ni-Mn-Ga described in chapter 4.6.

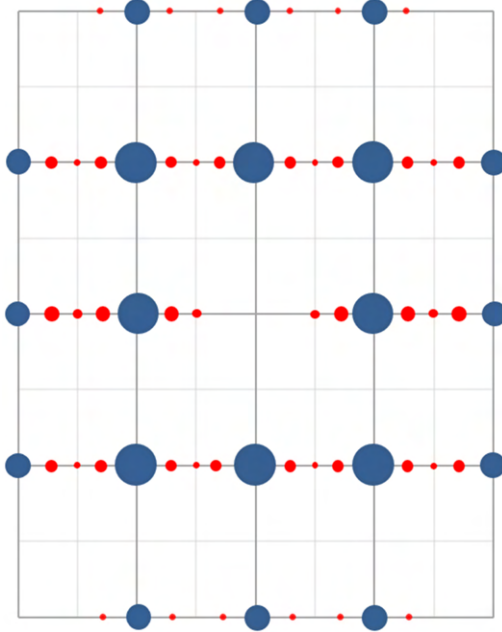


**Fig. 84:** Illustration of the diffraction pattern from the structure with commensurate modulation. Peaks from the average structure are marked blue, modulation satellites are marked red. Modulation vector  $\mathbf{q} = \frac{1}{4} \mathbf{a}^*$ .

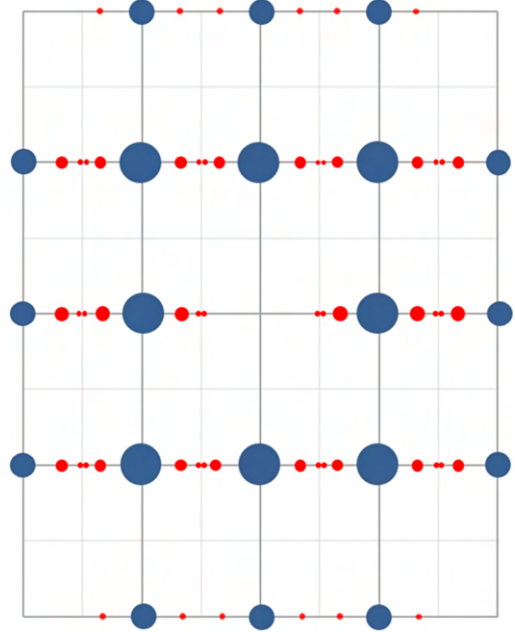


**Fig. 85:** Illustration of the diffraction pattern from the structure with incommensurate modulation. Modulation vector is  $\mathbf{q} = 0.267\dots \mathbf{a}^*$ . Note the satellite positions shift in comparison with the commensurate case.

In crystallography practice, structures with more than one independent modulation vector have been found. In such a case, equation (2) would then include multiple independent  $\mathbf{q}$  vectors. Nevertheless, to our best knowledge, only one modulation vector has been conclusively described in the Ni-Mn-Ga-based alloys so far.

Naturally, the symmetry rules valid for the crystal system must be valid for the modulation vector as well. E.g., in case of one-dimensional incommensurate modulation case it can be shown that only modulation vectors in the forms of  $(\alpha, \beta, 0)$  or  $(0, 0, \gamma)$  are admissible for our monoclinic crystal. [125]

For more information, reader is kindly referred, e.g., to reference [125].

## Appendix II: Complete list of analysed samples

no.	sample identifier	composition	sample responsible	state	phase at RT
1	220111TK	Ni <sub>50</sub> Mn <sub>25</sub> Ga <sub>20</sub> Fe <sub>5</sub>	RHC	single crystal	10M
2	austenite ingot slice 1	Ni-Mn-Ga-1.56%Fe	RHC	oligocrystal	A
3	austenite ingot slice 2	Ni-Mn-Ga-3.12%Fe	RHC	oligocrystal	A
4	austenite ingot slice 3	Ni-Mn-Ga-4.68%Fe	RHC	oligocrystal	A
5	austenite ingot slice 4	Ni-Mn-Ga-7.81%Fe	RHC	oligocrystal	A
6	austenite ingot slice 5	Ni-Mn-Ga-9.37%Fe	RHC	oligocrystal	A
7	austenite ingot slice 6	Ni-Mn-Ga-10.93%Fe	RHC	oligocrystal	A
8	2_44-6	Ni-Mn-Ga(-Fe)	RHC	oligocrystal	A
9	3_37-12	Ni-Mn-Ga(-Fe)	RHC	oligocrystal	A
10	4_31-19	Ni-Mn-Ga(-Fe)	RHC	oligocrystal	A
11	5_25-25	Ni-Mn-Ga(-Fe)	RHC	oligocrystal	A
12	6_18-31	Ni-Mn-Ga(-Fe)	RHC	oligocrystal	A
13	7_12-38	Ni-Mn-Ga(-Fe)	RHC	oligocrystal	A
14	8_12.5-37.5	Ni-Mn-Ga(-Fe)	RHC	oligocrystal	A
15	RHCO56 BI	Ni <sub>31.25</sub> Fe <sub>18.75</sub> Mn <sub>25</sub> Ga <sub>25</sub>	RHC	bicrystal	14M
16	100229 LS3	Ni-Mn-Ga-Fe	OH	single crystal	multiphase
17	Fe <sub>44</sub> Mn <sub>25</sub> Ga <sub>31</sub>	Fe <sub>44</sub> Mn <sub>25</sub> Ga <sub>31</sub>	OH	single crystal	A
18	Fe <sub>44</sub> Mn <sub>28</sub> Ga <sub>28</sub>	Fe <sub>44</sub> Mn <sub>28</sub> Ga <sub>28</sub>	OH	highly textured polycrystal	Fe <sub>3</sub> Ga, Fe <sub>2</sub> MnGa
19	FeMnGa ross c4	Fe <sub>44</sub> Mn <sub>26</sub> Ga <sub>30</sub>	OH/RHC	single crystal	A+M
20	J013A 200210	Ni-Mn-Ga 200 nm + 20 nm Cr	OH	epitaxial thin layer	A+M+Cr
21	J014A 200214	Ni-Mn-Ga 24 nm + 20 nm Cr	OH	epitaxial thin layer	A+Cr
22	J015A 200218	Ni-Mn-Ga 100 nm + 20 nm Cr	OH	epitaxial thin layer	A+Cr
23	J016A 200220	Ni-Mn-Ga 20 nm + 20 nm Cr	OH	epitaxial thin layer	A+Cr
24	J017A 200224	Ni-Mn-Ga 50 nm + 20 nm Cr	OH	epitaxial thin layer	A+Cr
25	J018A 200226	Ni-Mn-Ga 10 nm + 10 nm of Cr	OH	epitaxial thin layer	A+Cr
26	J038C 210202	Ni-Mn-Ga multilayer	OH	epitaxial thin layer	10M+14M+Cr
27	Ni <sub>43</sub> Mn <sub>19</sub> Ga <sub>28</sub> RHC2008	Ni <sub>43</sub> Mn <sub>19</sub> Ga <sub>28</sub>	RHC	oligocrystal	A
28	211014FZU	Ni <sub>50</sub> Mn <sub>25</sub> Fe <sub>20</sub> Cr <sub>5</sub>	OH	oligocrystal	NM+Cr
29	190718FZU	Ni <sub>50</sub> Mn <sub>25</sub> Ga <sub>20</sub> Cu <sub>5</sub>	OH	polycrystal	NM
30	Ni <sub>50</sub> Mn <sub>25</sub> Ga <sub>20</sub> Fe <sub>5</sub>	Ni <sub>50</sub> Mn <sub>25</sub> Ga <sub>20</sub> Fe <sub>5</sub>	OH	single crystal	14M
31	110322	Ni <sub>50</sub> Mn <sub>31</sub> Ga <sub>19</sub>	OH	single crystal	14M+NM
32	412	Ni <sub>50</sub> Mn <sub>28.4</sub> Ga <sub>21.6</sub>	OH	single crystal	10M
33	Ni <sub>2</sub> MnGa	Ni <sub>2</sub> MnGa	OH	single crystal	A
34	416	Ni <sub>50</sub> Mn <sub>28.8</sub> Ga <sub>21.2</sub>	OH	single crystal	10M
35	331	Ni <sub>50</sub> Mn <sub>28.1</sub> Ga <sub>21.9</sub>	OH	single crystal	10M
36	190528FZU	Ni <sub>50</sub> Mn <sub>32</sub> Ga <sub>18</sub>	OH	oligocrystal	14M
37	NMG NM c1	Ni <sub>53</sub> Mn <sub>24</sub> Ga <sub>23</sub>	OH/RHC	single crystal	NM
38	101207	Ni <sub>50</sub> Mn <sub>27</sub> Ga <sub>22</sub> Fe <sub>1</sub>	OH	single crystal	10M
39	526	Ni <sub>50</sub> Mn <sub>28</sub> Ga <sub>22</sub>	OH	single crystal	10M
40	622	Ni <sub>50</sub> Mn <sub>28.5</sub> Ga <sub>21.5</sub>	OH	single crystal	10M
41	100507_A	Ni <sub>50</sub> Mn <sub>28</sub> Ga <sub>22</sub>	OH	single crystal	10M
42	100507_B	Ni <sub>50</sub> Mn <sub>28</sub> Ga <sub>22</sub>	OH	single crystal	10M



no.	sample identifier	composition	sample responsible	state	phase at RT
43	100507_C	Ni <sub>50</sub> Mn <sub>28</sub> Ga <sub>22</sub>	OH	single crystal	10M
44	100610HT	Ni <sub>50</sub> Mn <sub>27.7</sub> Ga <sub>22.3</sub>	OH	single crystal	10M
45	100301	Ni <sub>50</sub> Mn <sub>25</sub> Ga <sub>21</sub> Fe <sub>4</sub>	OH	single crystal	10M
46	110301_NMprime	Ni <sub>50</sub> Mn <sub>25</sub> Ga <sub>21</sub> Fe <sub>4</sub>	OH	single crystal	10M
47	201202_NM	Ni <sub>52.8</sub> Mn <sub>25.7</sub> Ga <sub>21.5</sub>	OH	oligocrystal	10M+14M
48	NM_0303b_big_piece	Ni <sub>50.5</sub> Mn <sub>30.4</sub> Ga <sub>19.1</sub>	OH	single crystal	NM
49	NM_0303b_thin_piece	Ni <sub>50.5</sub> Mn <sub>30.4</sub> Ga <sub>19.1</sub>	OH	single crystal	NM
50	NMG S7 217	Ni <sub>46</sub> Mn <sub>24</sub> Ga <sub>22</sub> Co <sub>4</sub> Cu <sub>4</sub>	OH	single crystal	NM
51	RHC_2005_A_1	Ni <sub>50.5</sub> Mn <sub>28.3</sub> Ga <sub>21.2</sub>	RHC/OH	single crystal	14M
52	RHC_2005_A_3	Ni <sub>50.5</sub> Mn <sub>28.3</sub> Ga <sub>21.2</sub>	RHC/OH	single crystal	14M
53	RHC_2005_A_3_cut	Ni <sub>50.5</sub> Mn <sub>28.3</sub> Ga <sub>21.2</sub>	RHC/OH	single crystal	14M
54	170727FZU-BM-s03	Ni <sub>50</sub> Mn <sub>25</sub> Ga <sub>25</sub>	VK	oligocrystal	A
55	191218FZU-PC1	Ni <sub>49</sub> Mn <sub>29</sub> Ga <sub>22</sub>	VK	oligocrystal	14M(+A)
56	200110FZU-bottom	Ni <sub>49</sub> Mn <sub>29</sub> Ga <sub>22</sub>	VK	single crystal	14M
57	200110FZU-top	Ni <sub>49</sub> Mn <sub>29</sub> Ga <sub>22</sub>	VK	single crystal	multiphase
58	200811FZU-PC	Ni <sub>48.6</sub> Mn <sub>27.7</sub> Ga <sub>23.7</sub>	VK	oligocrystal	10M
59	210115FZU	Ni <sub>50</sub> Mn <sub>28.5</sub> Ga <sub>21.5</sub>	VK	single crystal	10M
60	210415FZU-PC	Ni <sub>50</sub> Mn <sub>25</sub> Ga <sub>25</sub>	VK	oligocrystal	A
61	210823FZU-PC	Ni <sub>47.2</sub> Mn <sub>24.7</sub> Ga <sub>28.1</sub>	VK	oligocrystal	A
62	210825_C2	Ni <sub>50</sub> Mn <sub>25</sub> Ga <sub>25</sub>	VK	oligocrystal	A
63	211004-2FZU	Ni <sub>45</sub> Co <sub>5</sub> Mn <sub>25</sub> Ga <sub>25</sub>	VK	oligocrystal	A(+10M)
64	211005-2FZU	Ni <sub>50</sub> Mn <sub>25</sub> Ga <sub>20</sub> Co <sub>5</sub>	VK	oligocrystal	NM
65	220223FZU_B	Ni <sub>49.9</sub> Mn <sub>24.4</sub> Ga <sub>25.7</sub>	VK	oligocrystal	A
66	220223FZU_D	Ni <sub>49.8</sub> Mn <sub>24.7</sub> Ga <sub>25.5</sub>	VK	oligocrystal	A
67	220303FZU_B	Ni <sub>49.8</sub> Mn <sub>24.2</sub> Ga <sub>26</sub>	VK	oligocrystal	A
68	220303FZU_D	Ni <sub>49.5</sub> Mn <sub>24.6</sub> Ga <sub>25.9</sub>	VK	oligocrystal	A
69	Ni <sub>45</sub> Fe <sub>5</sub> Mn <sub>25</sub> Ga <sub>25</sub>	Ni <sub>45</sub> Fe <sub>5</sub> Mn <sub>25</sub> Ga <sub>25</sub>	VK	polycrystal with large grains	A
70	180327-1FZU	Ni <sub>45</sub> Co <sub>5</sub> Mn <sub>25</sub> Ga <sub>5</sub>	VK	oligocrystal	A
71	190402FZU	Ni <sub>45</sub> Co <sub>5</sub> Mn <sub>25</sub> Ga <sub>25</sub>	VK	oligocrystal	A
72	170406FZU	Ni <sub>45</sub> Fe <sub>5</sub> Mn <sub>25</sub> Ga <sub>25</sub>	VK	oligocrystal	A
73	Ni <sub>45</sub> Mn <sub>25</sub> Ga <sub>25</sub> Co <sub>5</sub> as cast new	Ni <sub>45</sub> Mn <sub>25</sub> Ga <sub>25</sub> Co <sub>5</sub>	VK	oligocrystal	A(+10M)
74	190318FZU	Ni <sub>50</sub> Co <sub>5</sub> Mn <sub>25</sub> Ga <sub>20</sub>	VK	oligocrystal	14M+NM??
75	190404FZU	Ni <sub>50</sub> Mn <sub>20</sub> Co <sub>5</sub> Ga <sub>25</sub>	VK	oligocrystal	NM
76	170316-1FZU	Ni <sub>50</sub> Mn <sub>20</sub> Ga <sub>25</sub> Fe <sub>5</sub>	VK	oligocrystal	A
77	170316-2FZU	Ni <sub>50</sub> Mn <sub>25</sub> Ga <sub>20</sub> Fe <sub>5</sub>	VK	oligocrystal	A
78	180822-1FZU	Ni <sub>55</sub> Mn <sub>20</sub> Ga <sub>25</sub>	VK	oligocrystal	NM
79	180822-2FZU	Ni <sub>55</sub> Mn <sub>20</sub> Ga <sub>25</sub>	VK	oligocrystal	NM
80	NMG_powder_1-4	Ni <sub>45</sub> Mn <sub>25</sub> Ga <sub>25</sub> Co <sub>5</sub>	VK	powder	A+M +contamination
81	NMG_powder_5-6	Ni <sub>50</sub> Mn <sub>25</sub> Ga <sub>20</sub> Co <sub>5</sub>	VK	powder	14M+NM+A +contamination
82	RHC_2011	Ni <sub>50</sub> Mn <sub>25</sub> Ga <sub>25</sub>	VK/RHC	single crystal	A
83	190912FZU_piece	Ni <sub>49.7</sub> Mn <sub>28.4</sub> Ga <sub>21.9</sub>	DM/VK	single crystal	10M
84	190912FZU_piece_2grains	Ni <sub>49.7</sub> Mn <sub>28.4</sub> Ga <sub>21.9</sub>	DM/VK	bicrystal	10M

no.	sample identifier	composition	sample responsible	state	phase at RT
85	FIB_damage	Ni <sub>50</sub> Mn <sub>28.5</sub> Ga <sub>21.5</sub>	DM	single crystal	10M
86	KF2102B1	Ni <sub>50</sub> Mn <sub>28.5</sub> Ga <sub>21.5</sub>	DM	single crystal	10M
87	Ni <sub>50</sub> Mn <sub>28.5</sub> Ga <sub>21.5</sub> bottom	Ni <sub>50</sub> Mn <sub>28.5</sub> Ga <sub>21.5</sub>	DM	highly textured polycrystal	10M
88	Ni <sub>50</sub> Mn <sub>28.5</sub> Ga <sub>21.5</sub> top	Ni <sub>50</sub> Mn <sub>28.5</sub> Ga <sub>21.5</sub>	DM	polycrystal with large grains	10M
89	RHC 2012s3cracked foil disc	Ni <sub>50.4</sub> Mn <sub>26.2</sub> Ga <sub>23.4</sub>	DM/RHC	oligocrystal	10M
90	RHC 2010	Ni <sub>49.4</sub> Mn <sub>29.7</sub> Ga <sub>20.9</sub>	DM/RHC	oligocrystal	mostly 10M
91	RHC2012_s1d	Ni <sub>51.2</sub> Mn <sub>26.1</sub> Ga <sub>22.7</sub>	DM/RHC	polycrystal + one large grain	10M
92	RHC2012_s2d	Ni <sub>50.2</sub> Mn <sub>27.2</sub> Ga <sub>22.6</sub>	DM/RHC	single crystal	10M
93	RHC2104_T1	Ni <sub>49.5</sub> Mn <sub>26.5</sub> Ga <sub>22.7</sub> Fe <sub>1.3</sub>	DM/RHC	single crystal	10M
94	RHC2105_top disc	Ni <sub>49.5</sub> Mn <sub>23.3</sub> Ga <sub>23</sub> Fe <sub>4.2</sub>	DM/RHC	single crystal	A
95	RHC2121sc	Ni <sub>45.1</sub> Mn <sub>23.9</sub> Ga <sub>20.9</sub> Cu <sub>5.1</sub> Co <sub>4.7</sub> Fe <sub>0.3</sub>	DM/RHC	single crystal	10M
96	RHC2134_1B	Ni <sub>46</sub> Mn <sub>24.2</sub> Ga <sub>21</sub> Cu <sub>4.1</sub> Co <sub>4.2</sub> Fe <sub>0.5</sub>	DM/RHC	oligocrystal	NM
97	RHC2134_2B	Ni <sub>44.3</sub> Mn <sub>25.3</sub> Ga <sub>20.3</sub> Cu <sub>4.8</sub> Co <sub>4.7</sub> Fe <sub>0.6</sub>	DM/RHC	oligocrystal	NM
98	RHC2134_2T	Ni <sub>44.1</sub> Mn <sub>25.1</sub> Ga <sub>20.3</sub> Cu <sub>5</sub> Co <sub>4.7</sub> Fe <sub>0.8</sub>	DM/RHC	oligocrystal	NM
99	RHC2134_3T	Ni <sub>44.3</sub> Mn <sub>24.7</sub> Ga <sub>20.6</sub> Cu <sub>4.7</sub> Co <sub>4.8</sub> Fe <sub>0.9</sub>	DM/RHC	oligocrystal	NM
100	227A	Ni <sub>50</sub> Mn <sub>28</sub> Ga <sub>22</sub>	FN	single crystal	10M
101	526	Ni <sub>50</sub> Mn <sub>28</sub> Ga <sub>22</sub>	FN	single crystal	10M
102	C8	Ni <sub>50</sub> Mn <sub>25</sub> Ga <sub>23</sub> Fe <sub>1</sub> Cu <sub>1</sub>	FN	oligocrystal	A+10M+14M
103	C9	Ni <sub>50</sub> Mn <sub>25</sub> Ga <sub>22.5</sub> Fe <sub>2</sub> Cu <sub>0.5</sub>	FN	polycrystal with large grains	14M
104	ETO_big	Ni <sub>50</sub> Mn <sub>28</sub> Ga <sub>22</sub>	FN	single crystal	10M
105	ETO_small	Ni <sub>50</sub> Mn <sub>28</sub> Ga <sub>22</sub>	FN	single crystal	10M
106	Ni <sub>49</sub> Mn <sub>27</sub> Ga <sub>19.5</sub> Fe <sub>4</sub> Cu <sub>0.5</sub> as cast	Ni <sub>49</sub> Mn <sub>27</sub> Ga <sub>19.5</sub> Fe <sub>4</sub> Cu <sub>0.5</sub>	AA/FN	highly textured polycrystal	14M+NM
107	Ni <sub>49</sub> Mn <sub>27</sub> Ga <sub>19.5</sub> Fe <sub>4</sub> Cu <sub>0.5</sub> annealed	Ni <sub>49</sub> Mn <sub>27</sub> Ga <sub>19.5</sub> Fe <sub>4</sub> Cu <sub>0.5</sub>	AA/FN	highly textured polycrystal	14M+NM
108	Ni <sub>49</sub> Mn <sub>27</sub> Ga <sub>21.5</sub> Fe <sub>2</sub> Cu <sub>0.5</sub> as cast	Ni <sub>49</sub> Mn <sub>27</sub> Ga <sub>21.5</sub> Fe <sub>2</sub> Cu <sub>0.5</sub>	AA/FN	highly textured polycrystal	14M+10M
109	Ni <sub>49</sub> Mn <sub>27</sub> Ga <sub>21.5</sub> Fe <sub>2</sub> Cu <sub>0.5</sub> annealed	Ni <sub>49</sub> Mn <sub>27</sub> Ga <sub>21.5</sub> Fe <sub>2</sub> Cu <sub>0.5</sub>	AA/FN	highly textured polycrystal	14M+10M
110	Ni <sub>49</sub> Mn <sub>27</sub> Ga <sub>23.5</sub> Cu <sub>0.5</sub> as cast	Ni <sub>49</sub> Mn <sub>27</sub> Ga <sub>23.5</sub> Cu <sub>0.5</sub>	AA/FN	highly textured polycrystal	A
111	Ni <sub>49</sub> Mn <sub>27</sub> Ga <sub>23.5</sub> Cu <sub>0.5</sub> annealed	Ni <sub>49</sub> Mn <sub>27</sub> Ga <sub>23.5</sub> Cu <sub>0.5</sub>	AA/FN	highly textured polycrystal	A
112	Ni <sub>50</sub> Mn <sub>24</sub> Ga <sub>18</sub> Fe <sub>4</sub> Cu <sub>4</sub> as cast	Ni <sub>50</sub> Mn <sub>24</sub> Ga <sub>18</sub> Fe <sub>4</sub> Cu <sub>4</sub>	AA/FN	highly textured polycrystal	NM
113	Ni <sub>50</sub> Mn <sub>24</sub> Ga <sub>18</sub> Fe <sub>4</sub> Cu <sub>4</sub> annealed	Ni <sub>50</sub> Mn <sub>24</sub> Ga <sub>18</sub> Fe <sub>4</sub> Cu <sub>4</sub>	AA/FN	highly textured polycrystal	NM
114	Ni <sub>50</sub> Mn <sub>26</sub> Ga <sub>20</sub> Fe <sub>2</sub> Cu <sub>2</sub> as cast	Ni <sub>50</sub> Mn <sub>26</sub> Ga <sub>20</sub> Fe <sub>2</sub> Cu <sub>2</sub>	AA/FN	highly textured polycrystal	NM
115	Ni <sub>50</sub> Mn <sub>26</sub> Ga <sub>20</sub> Fe <sub>2</sub> Cu <sub>2</sub> annealed	Ni <sub>50</sub> Mn <sub>26</sub> Ga <sub>20</sub> Fe <sub>2</sub> Cu <sub>2</sub>	AA/FN	highly textured polycrystal	NM
116	Ni <sub>50</sub> Mn <sub>27</sub> Ga <sub>21</sub> Fe <sub>1</sub> Cu <sub>1</sub> as cast	Ni <sub>50</sub> Mn <sub>27</sub> Ga <sub>21</sub> Fe <sub>1</sub> Cu <sub>1</sub>	AA/FN	highly textured polycrystal	10M+14M+NM
117	Ni <sub>50</sub> Mn <sub>27</sub> Ga <sub>21</sub> Fe <sub>1</sub> Cu <sub>1</sub> annealed	Ni <sub>50</sub> Mn <sub>27</sub> Ga <sub>21</sub> Fe <sub>1</sub> Cu <sub>1</sub>	AA/FN	highly textured polycrystal	NM
118	RHCO4I_AI_MI	Ni <sub>50</sub> Mn <sub>28</sub> Ga <sub>22</sub>	FN/RHC	oligocrystal	10M
119	RHCO54_long_rod	Ni <sub>50</sub> Mn <sub>28</sub> Ga <sub>22</sub>	FN/RHC	single crystal	NM+additional
120	NiMnGa_austenite_long	Ni-Mn-Ga(-Fe)	OP/RHC	single crystal	A
121	NiMnGa_random_cut	Ni-Mn-Ga(-Fe)	OP/RHC	single crystal	A
122	RHC2019_NM	Ni <sub>46.9</sub> Mn <sub>28.1</sub> Ga <sub>18.8</sub> Fe <sub>3.3</sub> Cu <sub>3.1</sub>	OP/RHC	oligocrystal	NM
123	NiMnGa_rod_orientation	Ni <sub>50</sub> Mn <sub>28.5</sub> Ga <sub>21.5</sub>	OP/RHC	single crystal	10M
124	NMG_austenite_100	Ni-Mn-Ga(-Fe)	OP/RHC	single crystal	A
125	NMG_slice	Ni-Mn-Ga(-Fe)	OP/RHC	single crystal	A
126	RHC_2104	Ni <sub>49.5</sub> Mn <sub>26.5</sub> Ga <sub>22.7</sub> Fe <sub>1.3</sub>	OP/RHC	oligocrystal	10M

no.	sample identifier	composition	sample responsible	state	phase at RT
127	RHC_2105_0	Ni <sub>49.5</sub> Mn <sub>23.3</sub> Ga <sub>23</sub> Fe <sub>4.2</sub>	OP/RHC	single crystal	10M
128	RHC_2105_0_cut	Ni <sub>49.5</sub> Mn <sub>23.3</sub> Ga <sub>23</sub> Fe <sub>4.2</sub>	OP/RHC	single crystal	10M
129	RHC_2105_1	Ni <sub>49.5</sub> Mn <sub>23.3</sub> Ga <sub>23</sub> Fe <sub>4.2</sub>	OP/RHC	oligocrystal	10M+A
130	RHC_2105_2_middle	Ni <sub>49.5</sub> Mn <sub>23.3</sub> Ga <sub>23</sub> Fe <sub>4.2</sub>	OP/RHC	oligocrystal	A(+10M)
131	RHC2001	Ni <sub>50</sub> Mn <sub>28.5</sub> Ga <sub>21.5</sub>	OP/RHC	single crystal	10M
132	RHC2103_AFS	Ni <sub>49.2</sub> Mn <sub>28.7</sub> Ga <sub>21.5</sub> Fe <sub>0.6</sub>	OP/RHC	single crystal	10M
133	RHC2126SC1	Ni <sub>49.8</sub> Mn <sub>26.6</sub> Ga <sub>21.6</sub>	OP/RHC	single crystal	10M
134	091014	Ni <sub>50</sub> Mn <sub>25</sub> Ga <sub>20</sub> Fe <sub>5</sub>	LS	single crystal	10M
135	110301_S4	Ni <sub>50</sub> Mn <sub>25</sub> Ga <sub>21</sub> Fe <sub>4</sub>	LS	single crystal	10M
136	NiMnGa_10M_10507	Ni <sub>50</sub> Mn <sub>28</sub> Ga <sub>22</sub>	LS/HS	single crystal	10M
137	NiMnGa_207_2	Ni <sub>50</sub> Mn <sub>27</sub> Ga <sub>22</sub> Fe <sub>1</sub>	LS	single crystal	10M
138	NM-bod	Ni <sub>50</sub> Mn <sub>31</sub> Ga <sub>19</sub>	LS	single crystal	10M+NM

Sample responsables:

AA ... Andrew Armstrong  
RHC ... Ross H. Colman  
OH ... Oleg Heczko  
VK ... Vít Kopecký  
DM ... Denys Musiienko  
FN ... Frans Nilsén  
OP ... Oleksii Perevertov  
HS ... Hanuš Seiner  
LS ... Ladislav Straka

## References

- [1] K. Ullakko, J.K. Huang, C. Kantner, R.C.O. Handley, Large magnetic-field-induced strains in Ni<sub>2</sub>MnGa single crystals, *Appl. Phys. Lett.* 69 (1996) 1966–1968.
- [2] J.M. Stephan, E. Pagounis, M. Laufenberg, O. Paul, P. Ruther, A Novel Concept for Strain Sensing Based on the Ferromagnetic Shape Memory Alloy NiMnGa, *IEEE Sens. J.* 11 (2011) 2683–2689. <https://doi.org/10.1109/JSEN.2011.2157489>.
- [3] R.C. O’Handley, K. Ullakko, High-strain, magnetic field-controlled actuator materials, US patent US5958154A, 1997.
- [4] J. Tellinen, I. Suorsa, I. Aaltio, K. Ullakko, Basic Properties of Magnetic Shape Memory Actuators, (2002) 10–12.
- [5] A.R. Smith, D. Fologea, P. Muellner, Magnetically Driven Pump for Solid-state Microfluidic Flow Control, in: *ACTUATOR 2018; 16th Int. Conf. New Actuators*, 2018: pp. 1–2.
- [6] N.M. Bruno, C. Ciocanel, H.P. Feigenbaum, A. Waldauer, A theoretical and experimental investigation of power harvesting using the NiMnGa martensite reorientation mechanism, *Smart Mater. Struct.* 21 (2012). <https://doi.org/10.1088/0964-1726/21/9/094018>.
- [7] F. Heusler, Über Magnetische Manganlegierungen, *Verhandlungen Der Dtsch. Phys. Gesellschaft.* 12 (1903) 219.
- [8] F. Heusler, W. Starck, E. Haupt, Magnetisch-chemische Studien, *Verh. Dtsch. Phys. Ges.* 12 (1903) 220–232.
- [9] P.J. Webster, Heusler alloys, *Contemp. Phys.* 10 (1969) 559–577. <https://doi.org/10.1080/00107516908204800>.
- [10] **P. Veřtát**, Investigation of martensitic transformation in Ni-Mn-Ga and similar Heusler alloys, *Diploma Thesis*, Czech Technical University in Prague, 2017.
- [11] T. Graf, C. Felser, S.S.P. Parkin, Simple rules for the understanding of Heusler compounds, *Prog. Solid State Chem.* 39 (2011) 1–50. <https://doi.org/10.1016/j.progsolidstchem.2011.02.001>.
- [12] P. Entel, V.D. Buchelnikov, V. V. Khovailo, A.T. Zayak, W.A. Adeagbo, M.E. Gruner, H.C. Herper, E.F. Wassermann, Modelling the phase diagram of magnetic shape memory Heusler alloys, *J. Phys. D. Appl. Phys.* 39 (2006) 865–889. <https://doi.org/10.1088/0022-3727/39/5/S13>.
- [13] P. Entel, M. Siewert, M.E. Gruner, H.C. Herper, D. Comtesse, R. Arróyave, N. Singh, A. Talapatra, V. V Sokolovskiy, V.D. Buchelnikov, F. Albertini, L. Righi, V.A. Chernenko, Complex magnetic ordering as a driving mechanism of multifunctional properties of Heusler alloys from first principles, *Eur. Phys. J. B.* 86 (2013) 65. <https://doi.org/10.1140/epjb/e2012-30936-9>.
- [14] S. Ishida, M. Furugen, S. Asano, Ni excess and electronic structures of multi-functional Ni<sub>2.17</sub>Mn<sub>0.83</sub>Ga, *Int. J. Appl. Electromagn. Mech.* 12 (2001) 41–48. <https://doi.org/10.3233/JAE-2000-190>.
- [15] P. Leclair, X-ray diffraction of Heusler-like phases, (2016) 1–20. [pleclair.ua.edu/XRD/XRD-heusler-phases.pdf](http://pleclair.ua.edu/XRD/XRD-heusler-phases.pdf).
- [16] K.R.A. Ziebeck, P.J. Webster, A neutron diffraction and magnetization study of Heusler alloys containing Co and Zr, Hf, V or Nb, *J. Phys. Chem. Solids.* 35 (1974) 1–7. [https://doi.org/10.1016/0022-3697\(74\)90002-X](https://doi.org/10.1016/0022-3697(74)90002-X).
- [17] A.W. Carbonari, W. Pendl, R.N. Attili, R.N. Saxena, Magnetic hyperfine fields in the Heusler alloys Co<sub>2</sub>YZ (Y=Sc, Ti, Hf, V, Nb; Z=Al, Ga, Si, Ge, Sn), *Hyperfine Interact.* 80 (1993) 971–976. <https://doi.org/10.1007/BF00567449>.

- [18] P.J. Brown, K.U. Neumann, P.J. Webster, K.R.A. Ziebeck, The magnetization distributions in some Heusler alloys proposed as half-metallic ferromagnets, *J. Phys. Condens. Matter.* 12 (2000) 1827–1835. <https://doi.org/10.1088/0953-8984/12/8/325>.
- [19] S. Trudel, O. Gaier, J. Hamrle, B. Hillebrands, Magnetic anisotropy, exchange and damping in cobalt-based full-Heusler compounds: An experimental review, *J. Phys. D. Appl. Phys.* 43 (2010). <https://doi.org/10.1088/0022-3727/43/19/193001>.
- [20] T. Klimczuk, C.H. Wang, K. Gofryk, F. Ronning, J. Winterlik, G.H. Fecher, J.C. Griveau, E. Colineau, C. Felser, J.D. Thompson, D.J. Safarik, R.J. Cava, Superconductivity in the Heusler family of intermetallics, *Phys. Rev. B - Condens. Matter Mater. Phys.* 85 (2012) 1–8. <https://doi.org/10.1103/PhysRevB.85.174505>.
- [21] J.L. Jorda, M. Ishikawa, J. Muller, Phase Equilibria Pd-Y-Sn System, *J. Less-Common Met.* 107 (1985) 321–330.
- [22] S. Chadov, X. Qi, J. Kübler, G.H. Fecher, C. Felser, S.C. Zhang, Tunable multifunctional topological insulators in ternary Heusler compounds, *Nat. Mater.* 9 (2010) 541–545. <https://doi.org/10.1038/nmat2770>.
- [23] J. Pierre, R. V. Skolozdra, J. Tobola, S. Kaprzyk, C. Hordequin, M.A. Kouacou, I. Karla, R. Currat, E. Lelièvre-Berna, Properties on request in semi-Heusler phases, *J. Alloys Compd.* 262–263 (1997) 101–107. [https://doi.org/10.1016/S0925-8388\(97\)00337-X](https://doi.org/10.1016/S0925-8388(97)00337-X).
- [24] D.A. Porter, K.E. Easterling, M.Y. Sherif, Phase transformations in metals and alloys, third edition, 2009.
- [25] V.V. Martynov, V.V. Kokorin, The crystal structure of thermally- and stress-induced Martensites in Ni<sub>2</sub>MnGa single crystals, *J. Phys III Fr.* 2 (1992) 739–749.
- [26] O. Heczko, Magnetic shape memory effect and highly mobile twin boundaries, *Mater. Sci. Technol. (United Kingdom)*. 30 (2014) 1559–1578. <https://doi.org/10.1179/1743284714Y.0000000599>.
- [27] R. Niemann, O. Heczko, L. Schultz, S. Fähler, Metamagnetic transitions and magnetocaloric effect in epitaxial Ni-Co-Mn-In films, *Appl. Phys. Lett.* 97 (2010). <https://doi.org/10.1063/1.3517443>.
- [28] H. Bhadeshia, Martensite in steels, *Mater. Sci. Metall.* (2002) 1–12.
- [29] G. Nolze, Determination of orientation relationships between fcc / bcc lattices by the use of pole figures, *HKL User Meet.* (2004) 1–9.
- [30] E.C. Bain, N.Y. Dunkirk, The nature of martensite, *Trans. AIME.* 70 (1924) 25–47.
- [31] K. Otsuka, C.M. Wayman, Shape Memory Materials, Cambridge University Press, 1998.
- [32] H. Seiner, O. Heczko, P. Sedlák, L. Bodnárová, M. Novotný, J. Kopeček, M. Landa, Combined effect of structural softening and magneto-elastic coupling on elastic coefficients of NiMnGa austenite, *J. Alloys Compd.* 577 (2013) 131–135. <https://doi.org/10.1016/j.jallcom.2012.01.007>.
- [33] P. Zhao, L. Dai, J. Cullen, M. Wuttig, Magnetic and elastic properties of Ni<sub>49.0</sub>Mn<sub>23.5</sub>Ga<sub>27.5</sub> premartensite, *Metall. Mater. Trans. A Phys. Metall. Mater. Sci.* 38 (2007) 745–751. <https://doi.org/10.1007/s11661-007-9099-4>.
- [34] P. Entel, M.E. Gruner, A. Dannenberg, M. Siewert, S.K. Nayak, H.C. Herper, V.D. Buchelnikov, Fundamental aspects of magnetic shape memory alloys: Insights from ab initio and Monte Carlo studies, *Mater. Sci. Forum.* 635 (2010) 3–12. <https://doi.org/10.4028/www.scientific.net/MSF.635.3>.
- [35] A.N. Vasil'ev, A.D. Bozhko, V. V Khovailo, I.E. Dikshtein, V.G. Shavrov, V.D. Buchelnikov, M. Matsumoto, S. Suzuki, T. Takagi, J. Tani, Structural and magnetic phase transitions in shape-memory alloys (formula presented), *Phys. Rev. B - Condens. Matter Mater. Phys.* 59 (1999) 1113–1120. <https://doi.org/10.1103/PhysRevB.59.1113>.

- [36] K.F. Hane, T.W. Shield, Symmetry and microstructure in martensites, *Philos. Mag. A Phys. Condens. Matter, Struct. Defects Mech. Prop.* 78 (1998) 1215–1252. <https://doi.org/10.1080/01418619808239984>.
- [37] O. Heczko, N. Scheerbaum, O. Gutfleisch, Magnetic shape memory phenomena, in: J. Ping Liu, E. Fullerton, O. Gutfleisch, D.J. Sellmyer (Eds.), *Nanoscale Magn. Mater. Appl.*, Springer Science+Business Media, 2009: pp. 399–439. [https://doi.org/10.1007/978-0-387-85600-1\\_14](https://doi.org/10.1007/978-0-387-85600-1_14).
- [38] A. Sozinov, N. Lanska, A. Soroka, L. Straka, Highly mobile type II twin boundary in Ni-Mn-Ga five-layered martensite, *Appl. Phys. Lett.* 99 (2011) 124103. <https://doi.org/10.1063/1.3640489>.
- [39] L. Straka, O. Heczko, H. Seiner, N. Lanska, J. Drahokoupil, A. Soroka, S. Fähler, H. Hänninen, A. Sozinov, Highly mobile twinned interface in 10 M modulated Ni-Mn-Ga martensite: Analysis beyond the tetragonal approximation of lattice, *Acta Mater.* 59 (2011) 7450–7463. <https://doi.org/10.1016/j.actamat.2011.09.020>.
- [40] H. Seiner, M. Zelený, P. Sedlák, L. Straka, O. Heczko, Experimental Observations versus First-Principles Calculations for Ni–Mn–Ga Ferromagnetic Shape Memory Alloys: A Review, *Phys. Status Solidi - Rapid Res. Lett.* 16 (2022) 1–19. <https://doi.org/10.1002/pssr.202100632>.
- [41] R. Chulist, L. Straka, A. Sozinov, T. Lippmann, W. Skrotzki, Modulation reorientation in 10M Ni-Mn-Ga martensite, *Scr. Mater.* 68 (2013) 671–674. <https://doi.org/10.1016/j.scriptamat.2013.01.024>.
- [42] O. Heczko, L. Klimša, J. Kopeček, Direct observation of a-b twin laminate in monoclinic five-layered martensite of Ni-Mn-Ga magnetic shape memory single crystal, *Scr. Mater.* 131 (2017) 76–79. <https://doi.org/10.1016/j.scriptamat.2017.01.010>.
- [43] A. Saren, A. Sozinov, S. Kustov, K. Ullakko, Stress-induced a/b compound twins redistribution in 10M Ni-Mn-Ga martensite, *Scr. Mater.* 175 (2020) 11–15. <https://doi.org/10.1016/j.scriptamat.2019.09.001>.
- [44] H. Seiner, R. Chulist, W. Maziarz, A. Sozinov, O. Heczko, L. Straka, Non-conventional twins in five-layer modulated Ni-Mn-Ga martensite, *Scr. Mater.* 162 (2019) 497–502. <https://doi.org/10.1016/j.scriptamat.2018.12.020>.
- [45] H. Seiner, L. Straka, O. Heczko, A microstructural model of motion of macro-twin interfaces in Ni-Mn-Ga 10 M martensite, *J. Mech. Phys. Solids.* 64 (2014) 198–211. <https://doi.org/10.1016/j.jmps.2013.11.004>.
- [46] D. Kellis, A. Smith, K. Ullakko, P. Müllner, Oriented single crystals of Ni-Mn-Ga with very low switching field, *J. Cryst. Growth.* 359 (2012) 64–68. <https://doi.org/10.1016/j.jcrysgro.2012.08.014>.
- [47] A. Sozinov, N. Lanska, A. Soroka, W. Zou, 12% magnetic field-induced strain in Ni-Mn-Ga-based non-modulated martensite, *Appl. Phys. Lett.* 102 (2013) 021902. <https://doi.org/10.1063/1.4775677>.
- [48] F. Albertini, L. Morellon, P.A. Algarabel, M.R. Ibarra, L. Pareti, Z. Arnold, G. Calestani, Magnetoelastic effects and magnetic anisotropy in Ni<sub>2</sub>MnGa polycrystals, *J. Appl. Phys.* 89 (2001) 5614–5617. <https://doi.org/10.1063/1.1350630>.
- [49] N. Lanska, O. Söderberg, A. Sozinov, Y. Ge, K. Ullakko, V.K. Lindroos, Composition and temperature dependence of the crystal structure of Ni-Mn-Ga alloys, *J. Appl. Phys.* 95 (2004) 8074–8078. <https://doi.org/10.1063/1.1748860>.
- [50] A. Zheludev, S. Shapiro, P. Wochner, L. Tanner, Precursor effects and premartensitic transformation in MnGa, *Phys. Rev. B - Condens. Matter Mater. Phys.* 54 (1996) 15045–15050. <https://doi.org/10.1103/PhysRevB.54.15045>.
- [51] S. Singh, V. Petricek, P. Rajput, A.H. Hill, E. Suard, S.R. Barman, D. Pandey, High-resolution synchrotron x-ray powder diffraction study of the incommensurate modulation in the martensite phase of Ni<sub>2</sub>MnGa: Evidence for nearly 7M modulation and phason broadening, *Phys. Rev. B - Condens. Matter Mater. Phys.* 90 (2014) 1–9. <https://doi.org/10.1103/PhysRevB.90.014109>.

- [52] L. Righi, F. Albertini, A. Paoluzi, S. Fabbrici, E. Villa, G. Calestani, S. Besseghini, Incommensurate and commensurate structural modulation in martensitic phases of FSMA, *Mater. Sci. Forum.* 635 (2010) 33–41. <https://doi.org/10.4028/www.scientific.net/MSF.635.33>.
- [53] A. Sozinov, D. Musiienko, A. Saren, **P. Veřtát**, L. Straka, O. Heczko, M. Zelený, R. Chulist, K. Ullakko, Highly mobile twin boundaries in seven-layer modulated Ni–Mn–Ga–Fe martensite, *Scr. Mater.* 178 (2020) 62–66. <https://doi.org/10.1016/j.scriptamat.2019.10.042>.
- [54] K. Otsuka, T. Ohba, M. Tokonami, C.M. Wayman, New description of long period stacking order structures of martensites in  $\beta$ -phase alloys, *Scr. Metall. Mater.* 29 (1993) 1359–1364. [https://doi.org/10.1016/0956-716X\(93\)90139-J](https://doi.org/10.1016/0956-716X(93)90139-J).
- [55] M. Kreissl, K.U. Neumann, T. Stephens, K.R.A. Ziebeck, The influence of atomic order on the magnetic and structural properties of the ferromagnetic shape memory compound Ni<sub>2</sub>MnGa, *J. Phys. Condens. Matter.* 15 (2003) 3831–3839. <https://doi.org/10.1088/0953-8984/15/22/317>.
- [56] U. Gaitzsch, M. Pötschke, S. Roth, N. Mattern, B. Rellinghaus, L. Schultz, Structure formation in martensitic Ni<sub>50</sub>Mn<sub>30</sub>Ga<sub>20</sub> MSM alloy, *J. Alloys Compd.* 443 (2007) 99–104. <https://doi.org/10.1016/j.jallcom.2006.10.011>.
- [57] V. Kopecký, M. Rameš, **P. Veřtát**, R.H. Colman, O. Heczko, Full Variation of Site Substitution in Ni–Mn–Ga by Ferromagnetic Transition Metals, *Metals (Basel)*. 11 (2021) 850. <https://doi.org/10.3390/met11060850>.
- [58] M. Khan, I. Dubenko, S. Stadler, N. Ali, The structural and magnetic properties of Ni<sub>2</sub>Mn<sub>1-x</sub>M<sub>x</sub>Ga (M=Co, Cu), *J. Appl. Phys.* 97 (2005) 1–4. <https://doi.org/10.1063/1.1847131>.
- [59] J. Wang, H. Bai, C. Jiang, Y. Li, H. Xu, A highly plastic Ni<sub>50</sub>Mn<sub>25</sub>Cu<sub>18</sub>Ga<sub>7</sub> high-temperature shape memory alloy, *Mater. Sci. Eng. A.* 527 (2010) 1975–1978. <https://doi.org/10.1016/j.msea.2009.12.021>.
- [60] D.E. Soto-Parra, X. Moya, L. Manosa, A. Planes, H. Flo Es-Zuniga, F. Alvarado-Hernandez, R.A. Ochoa-Gamboa, J.A. Matutes-Aquino, D. Rios-Jara, Fe and Co selective substitution in Ni<sub>2</sub>MnGa: Effect of magnetism on relative phase stability, *Philos. Mag.* 90 (2010) 2771–2792. <https://doi.org/10.1080/14786431003745393>.
- [61] C.M. Li, H. Bin Luo, Q.M. Hu, R. Yang, B. Johansson, L. Vitos, Site preference and elastic properties of Fe-, Co-, and Cu-doped Ni<sub>2</sub>MnGa shape memory alloys from first principles, *Phys. Rev. B - Condens. Matter Mater. Phys.* 84 (2011) 024206. <https://doi.org/10.1103/PhysRevB.84.024206>.
- [62] L. Straka, A. Sozinov, J. Drahokoupil, V. Kopecký, H. Hänninen, O. Heczko, Effect of intermartensite transformation on twinning stress in Ni–Mn–Ga 10 M martensite, *J. Appl. Phys.* 114 (2013). <https://doi.org/10.1063/1.4817717>.
- [63] L. Straka, N. Lanska, K. Ullakko, A. Sozinov, Twin microstructure dependent mechanical response in Ni–Mn–Ga single crystals, *Appl. Phys. Lett.* 96 (2010) 10–13. <https://doi.org/10.1063/1.3373608>.
- [64] E. Pagounis, R. Chulist, M.J. Szczerba, M. Laufenberg, Over 7% magnetic field-induced strain in a Ni–Mn–Ga five-layered martensite, *Appl. Phys. Lett.* 105 (2014). <https://doi.org/10.1063/1.4892633>.
- [65] O. Heczko, V. Kopecký, A. Sozinov, L. Straka, Magnetic shape memory effect at 1.7 K, *Appl. Phys. Lett.* 103 (2013) 072405. <https://doi.org/10.1063/1.4817941>.
- [66] J. Pons, V.A. Chernenko, R. Santamarta, E. Cesari, Crystal structure of martensitic phases in Ni–Mn–Ga shape memory alloys, *Acta Mater.* 48 (2000) 3027–3038. [https://doi.org/10.1016/S1359-6454\(00\)00130-0](https://doi.org/10.1016/S1359-6454(00)00130-0).
- [67] O. Heczko, L. Straka, H. Seiner, Different microstructures of mobile twin boundaries in 10 M modulated Ni–Mn–Ga martensite, *Acta Mater.* 61 (2013) 622–631. <https://doi.org/10.1016/j.actamat.2012.10.007>.
- [68] R. Chulist, L. Straka, H. Seiner, A. Sozinov, N. Schell, T. Tokarski, Branching of {110} twin boundaries in five-layered Ni–Mn–Ga bent single crystals, *Mater. Des.* 171 (2019) 107703. <https://doi.org/10.1016/j.matdes.2019.107703>.

- [69] P.J. Webster, K.R.A. Ziebeck, S.L. Town, M.S. Peak, Magnetic order and phase transformation in Ni<sub>2</sub>MnGa, *Philos. Mag. B Phys. Condens. Matter; Stat. Mech. Electron. Opt. Magn. Prop.* 49 (1984) 295–310. <https://doi.org/10.1080/13642817408246515>.
- [70] L. Righi, F. Albertini, G. Calestani, L. Pareti, A. Paoluzi, C. Ritter, P.A. Algarabel, L. Morellon, M. Ricardo Ibarra, Incommensurate modulated structure of the ferromagnetic shape-memory Ni<sub>2</sub>MnGa martensite, *J. Solid State Chem.* 179 (2006) 3525–3533. <https://doi.org/10.1016/j.jssc.2006.07.005>.
- [71] L. Righi, F. Albertini, L. Pareti, A. Paoluzi, G. Calestani, Commensurate and incommensurate “5M” modulated crystal structures in Ni-Mn-Ga martensitic phases, *Acta Mater.* 55 (2007) 5237–5245. <https://doi.org/10.1016/j.actamat.2007.05.040>.
- [72] H. Kushida, K. Fukuda, T. Terai, T. Fukuda, T. Kakeshita, T. Ohba, T. Osakabe, K. Kakurai, K. Kato, Crystal structure of martensite and intermediate phases in Ni<sub>2</sub> MnGa studied by neutron diffraction, *Eur. Phys. J. Spec. Top.* 158 (2008) 87–92. <https://doi.org/10.1140/epjst/e2008-00658-2>.
- [73] T. Fukuda, H. Kushida, M. Todai, T. Kakeshita, H. Mori, Crystal structure of the martensite phase in the ferromagnetic shape memory compound Ni<sub>2</sub>MnGa studied by electron diffraction, *Scr. Mater.* 61 (2009) 473–476. <https://doi.org/10.1016/j.scriptamat.2009.04.046>.
- [74] L. Righi, Neutron Diffraction Study of the Martensitic Transformation of Ni<sub>2</sub>.07Mn<sub>0.93</sub>Ga Heusler Alloy, *Metals (Basel)*. 11 (2021) 1749. <https://doi.org/10.3390/met11111749>.
- [75] A. Çakir, M. Acet, L. Righi, F. Albertini, M. Farle, Characteristics of 5M modulated martensite in Ni-Mn-Ga magnetic shape memory alloys, *AIP Adv.* 5 (2015) 097222. <https://doi.org/10.1063/1.4932233>.
- [76] E. Pagounis, M.J. Szczerba, R. Chulist, M. Laufenberg, Large magnetic field-induced work output in a NiMnGa seven-layered modulated martensite, *Appl. Phys. Lett.* 107 (2015). <https://doi.org/10.1063/1.4933303>.
- [77] O. Söderberg, L. Straka, V. Novák, O. Heczko, S.P. Hannula, V.K. Lindroos, Tensile/compressive behaviour of non-layered tetragonal Ni<sub>52.8</sub> Mn<sub>25.7</sub>Ga<sub>21.5</sub> alloy, *Mater. Sci. Eng. A.* 386 (2004) 27–33. <https://doi.org/10.1016/j.msea.2004.07.045>.
- [78] I. Aaltio, A. Sozinov, Y. Ge, K. Ullakko, V.K. Lindroos, S.-P. Hannula, Giant Magnetostrictive Materials, in: *Ref. Modul. Mater. Sci. Mater. Eng.*, Elsevier, 2016. <https://doi.org/10.1016/B978-0-12-803581-8.01830-0>.
- [79] A.G. Khachatryan, S.M. Shapiro, S. Semenovskaya, Adaptive phase formation in martensitic transformation, *Phys. Rev. B.* 43 (1991) 10832–10843. <https://doi.org/10.1103/PhysRevB.43.10832>.
- [80] S. Kaufmann, U.K. Rößler, O. Heczko, M. Wuttig, J. Buschbeck, L. Schultz, S. Fähler, Adaptive modulations of martensites, *Phys. Rev. Lett.* 104 (2010) 145702. <https://doi.org/10.1103/PhysRevLett.104.145702>.
- [81] M. Zelený, L. Straka, A. Sozinov, O. Heczko, Ab initio prediction of stable nanotwin double layers and 4O structure in Ni<sub>2</sub>MnGa, *Phys. Rev. B.* 94 (2016) 1–6. <https://doi.org/10.1103/PhysRevB.94.224108>.
- [82] G.E. Bacon, *Neutron diffraction*, Clarendon Press, Oxford, 1975.
- [83] P. Molnar, P. Sittner, P. Lukas, S.P. Hannula, O. Heczko, Stress-induced martensite variant reorientation in magnetic shape memory Ni-Mn-Ga single crystal studied by neutron diffraction, *Smart Mater. Struct.* 17 (2008). <https://doi.org/10.1088/0964-1726/17/3/035014>.
- [84] P. Molnar, P. Sittner, V. Novak, J. Prokleska, V. Sechovsky, B. Ouladdiaf, S.P. Hanulla, O. Heczko, In situ neutron diffraction study of magnetic field induced martensite reorientation in Ni-Mn-Ga under constant stress, *J. Phys. Condens. Matter.* 20 (2008). <https://doi.org/10.1088/0953-8984/20/10/104224>.
- [85] M. Pötschke, U. Gaitzsch, S. Roth, B. Rellinghaus, L. Schultz, Preparation of melt textured Ni-Mn-Ga, *J. Magn. Magn. Mater.* 316 (2007) 383–385. <https://doi.org/10.1016/j.jmmm.2007.03.032>.



- [86] A. Wójcik, R. Chulist, P. Czaja, M. Kowalczyk, P. Zackiewicz, N. Schell, W. Maziarz, Evolution of microstructure and crystallographic texture of Ni-Mn-Ga melt-spun ribbons exhibiting 1.15% magnetic field-induced strain, *Acta Mater.* 219 (2021). <https://doi.org/10.1016/j.actamat.2021.117237>.
- [87] O. Heczko, P. Cejpek, J. Drahokoupil, V. Holý, Structure and microstructure of Ni-Mn-Ga single crystal exhibiting magnetic shape memory effect analysed by high resolution X-ray diffraction, *Acta Mater.* 115 (2016) 250–258. <https://doi.org/10.1016/j.actamat.2016.05.047>.
- [88] **P. Veřtát**, L. Straka, J. Drahokoupil, O. Heczko, Study of 10M' nanotwinned phase in the vicinity of martensitic transformation in Ni–Mn–Ga magnetic shape memory alloy, *Acta Phys. Pol. A.* 134 (2018) 859–862. <https://doi.org/10.12693/APhysPolA.134.859>.
- [89] PANalytical, X'Pert Texture 1.1a, (2005).
- [90] PANalytical, Epitaxy 4.3a, (2011).
- [91] OriginLab Corporation, OriginPro 2016, (2016). [www.OriginLab.com](http://www.OriginLab.com).
- [92] Bruker, DIFFRAC.SUITE TOPAS, <https://www.bruker.com/en/products-and-solutions/diffractometers-and-scattering-systems/x-ray-diffractometers/diffrac-suite-software/diffrac-topas.html>.
- [93] T. Degen, M. Sadki, E. Bron, U. König, G. Nénert, The HighScore suite, *Powder Diffr.* 29 (2014) S13–S18. <https://doi.org/10.1017/S0885715614000840>.
- [94] G. Bergerhoff, R. Hundt, R. Sievers, I.D. Brown, The inorganic crystal structure data base, *J. Chem. Inf. Comput. Sci.* 23 (1983) 66–69. <https://doi.org/10.1021/ci00038a003>.
- [95] S. Gates-Rector, T. Blanton, The Powder Diffraction File: a quality materials characterization database, *Powder Diffr.* 34 (2019) 352–360. <https://doi.org/10.1017/S0885715619000812>.
- [96] N. Qureshi, Rplot 1.5, (2016). <https://www.ill.eu/users/instruments/instruments-list/d10/software>.
- [97] D. Richard, M. Ferrand, G.J. Kearley, Analysis and visualisation of neutron-scattering data, *J. Neutron Res.* 4 (1996) 33–39. <https://doi.org/10.1080/10238169608200065>.
- [98] L. Fuentes-Montero, P. Čermák, J. Rodríguez-Carvajal, A. Filhol, Esmeralda Laue Suite, (2019). <https://www.lauesuite.com/>.
- [99] **P. Veřtát**, J. Drahokoupil, Fitexc – Diffraction Profile Fitting Program Run in Ms Excel, *Acta Polytech. CTU Proc.* 17 (2018) 20. <https://doi.org/10.14311/app.2018.17.0020>.
- [100] **P. Veřtát**, J. Drahokoupil, O. Heczko, The All-New FitExc: MS Excel-based Diffraction Profile Fitting Program (COVID LockDown Edition), *Mater. Struct.* 27 (2020) 103.
- [101] **P. Veřtát**, J. Drahokoupil, O. Heczko, Advanced diffraction profile fitting in FitExc Data processing, in: *Sborník Příspěvků 9. Studentské Vědecké Konf. Fyziky Pevných Látek a Mater., České vysoké učení technické v Praze, 2020*: pp. 74–77.
- [102] L. Straka, J. Drahokoupil, **P. Veřtát**, J. Kopeček, M. Zelený, H. Seiner, O. Heczko, Orthorhombic intermediate phase originating from {110} nanotwinning in Ni<sub>50.0</sub>Mn<sub>28.7</sub>Ga<sub>21.3</sub> modulated martensite, *Acta Mater.* 132 (2017) 335–344. <https://doi.org/10.1016/j.actamat.2017.04.048>.
- [103] D. Musiienko, F. Nilsén, A. Armstrong, M. Rameš, **P. Veřtát**, R.H. Colman, J. Capek, P. Müllner, O. Heczko, L. Straka, Effect of crystal quality on twinning stress in Ni-Mn-Ga magnetic shape memory alloys, *J. Mater. Res. Technol.* 14 (2021) 1934–1944. <https://doi.org/10.1016/j.jmrt.2021.07.081>.
- [104] A. Armstrong, F. Nilsén, M. Rameš, R.H. Colman, **P. Veřtát**, T. Kmječ, L. Straka, P. Müllner, O. Heczko, Systematic Trends of Transformation Temperatures and Crystal Structure of Ni–Mn–Ga–Fe–Cu Alloys, *Shape Mem. Superelasticity.* 6 (2020) 97–106. <https://doi.org/10.1007/s40830-020-00273-3>.

- [105] L. Straka, J. Drahokoupil, **P. Veřtát**, M. Zelený, J. Kopeček, A. Sozinov, O. Heczko, Low temperature a/b nanotwins in Ni<sub>50</sub>Mn<sub>25+x</sub>Ga<sub>25-x</sub> Heusler alloys, *Sci. Rep.* 8 (2018) 11943. <https://doi.org/10.1038/s41598-018-30388-8>.
- [106] M. Zelený, P. Sedlák, O. Heczko, H. Seiner, **P. Veřtát**, M. Obata, T. Kotani, T. Oda, L. Straka, Effect of electron localization in theoretical design of Ni-Mn-Ga based magnetic shape memory alloys, *Mater. Des.* 209 (2021). <https://doi.org/10.1016/j.matdes.2021.109917>.
- [107] **P. Veřtát**, L. Straka, H. Seiner, A. Sozinov, M. Klicpera, O. Fabelo, O. Heczko, Hysteretic structural changes within five-layered modulated 10M martensites of Ni-Mn-Ga(-Fe), *Acta Crystallogr. Sect. A Found. Adv.* 77 (2021) C399–C399. <https://doi.org/10.1107/S0108767321092874>.
- [108] L. Reimer, *Scanning Electron Microscopy: Physics of Image Formation and Microanalysis*, Second Edition, *Meas. Sci. Technol.* 11 (2000) 1826–1826. <https://doi.org/10.1088/0957-0233/11/12/703>.
- [109] **P. Veřtát**, H. Seiner, L. Straka, M. Klicpera, A. Sozinov, O. Fabelo, O. Heczko, Hysteretic structural changes within five-layered modulated 10M martensite of Ni-Mn-Ga(-Fe), *J. Phys. Condens. Matter.* 33 (2021) 265404. <https://doi.org/10.1088/1361-648x/abfb8f>.
- [110] **P. Veřtát**, J. Drahokoupil, O. Perevertov, O. Heczko, Phase transition in a multiferroic Ni-Mn-Ga single crystal, *Phase Transitions.* 89 (2016) 752–760. <https://doi.org/10.1080/01411594.2016.1199803>.
- [111] M. Klicpera, O.R. Fabelo Rosa, O. Heczko, L. Straka, **P. Veřtát**, Intermartensitic transformations and search for the ground state in Ni-Mn-Ga single crystals exhibiting the magnetic shape memory effect, (2018). <https://doi.org/10.5291/ILL-DATA.5-41-950>.
- [112] M. Klicpera, O.R. Fabelo Rosa, **P. Veřtát**, O. Heczko, L. Straka, Investigation of commensurate-incommensurate structure modulation transitions in Ni-Mn-Ga-Fe martensite, (2019). <https://doi.org/10.5291/ILL-DATA.5-15-626>.
- [113] V.K. Pecharsky, P.Y. Zavalij, *Fundamentals of powder diffraction and structural characterization of materials*, 2005. <https://doi.org/10.1007/978-0-387-09579-0>.
- [114] H.M. Rietveld, Line profiles of neutron powder-diffraction peaks for structure refinement, *Acta Crystallogr.* 22 (1967) 151–152. <https://doi.org/10.1107/s0365110x67000234>.
- [115] H.M. Rietveld, A profile refinement method for nuclear and magnetic structures, *J. Appl. Crystallogr.* 2 (1969) 65–71. <https://doi.org/10.1107/S0021889869006558>.
- [116] P. Vlčák, J. Drahokoupil, **P. Veřtát**, J. Šepitka, J. Duchoň, Hardness response to the stability of a Ti(+N) solid solution in an annealed TiN/Ti(+N)/Ti mixture layer formed by nitrogen ion implantation into titanium, *J. Alloys Compd.* 746 (2018) 490–495. <https://doi.org/10.1016/j.jallcom.2018.02.301>.
- [117] **P. Veřtát**, J. Drahokoupil, P. Vlčák, Surface Characterization of Titanium Alloys for Nitrogen Ion Implantation, *Acta Polytech. CTU Proc.* 9 (2017) 39. <https://doi.org/10.14311/app.2017.9.0039>.
- [118] J. Pinc, J. Čapek, J. Kubásek, F. Průša, V. Hybášek, **P. Veřtát**, I. Sedlářová, D. Vojtěch, Characterization of a Zn-Ca<sub>5</sub>(PO<sub>4</sub>)<sub>3</sub>(OH) composite with a high content of the hydroxyapatite particles prepared by the spark plasma sintering process, *Metals (Basel).* 10 (2020). <https://doi.org/10.3390/met10030372>.
- [119] J. Pinc, M. Španko, L. Lacina, J. Kubásek, P. Ashcheulov, **P. Veřtát**, A. Školáková, O. Kvítek, D. Vojtěch, J. Čapek, Influence of the pre-exposure of a Zn-0.8Mg-0.2Sr absorbable alloy in bovine serum albumin containing media on its surface changes and their impact on the cytocompatibility of the material, *Mater. Today Commun.* 28 (2021) 102556. <https://doi.org/10.1016/j.mtcomm.2021.102556>.
- [120] J. Pinc, A. Školáková, **P. Veřtát**, J. Čapek, Z. Žofková, L. Rieszová, S. Habr, D. Vojtěch, Microstructural Characterization and Optimization of the ZnMg<sub>0.8</sub>(CaO)<sub>0.26</sub> Alloy Processed by Ball Milling and Subsequent Extrusion, *Manuf. Technol.* 20 (2020) 484–491. <https://doi.org/10.21062/mft.2020.085>.

- [121] J. Pinc, J. Čapek, J. Kubásek, **P. Veřtát**, K. Hosová, Microstructure and mechanical properties of the potentially biodegradable ternary system Zn-Mg<sub>0.8</sub>-Ca<sub>0.2</sub>, *Procedia Struct. Integr.* 23 (2019) 21–26. <https://doi.org/10.1016/j.prostr.2020.01.057>.
- [122] NIST/SEMATECH e-Handbook of Statistical Methods, (2012). <https://doi.org/10.18434/M32189>.
- [123] Y.U. Wang, Diffraction theory of nanotwin superlattices with low symmetry phase, *Phys. Rev. B - Condens. Matter Mater. Phys.* 74 (2006) 1–4. <https://doi.org/10.1103/PhysRevB.74.104109>.
- [124] Y.U. Wang, Diffraction theory of nanotwin superlattices with low symmetry phase: Application to rhombohedral nanotwins and monoclinic MA and MB phases, *Phys. Rev. B - Condens. Matter Mater. Phys.* 76 (2007) 1–11. <https://doi.org/10.1103/PhysRevB.76.024108>.
- [125] S. Van Smaalen, *IUCr Monographs On Crystallography - 21 - Incommensurate Crystallography*, Oxford Univ. Press Inc., New York. (2007) 283.
- [126] J.C. Marmeggi, G.H. Lander, S. van Smaalen, T. Brückel, C.M.E. Zeyen, Neutron-diffraction study of the charge-density wave in  $\alpha$ -uranium, *Phys. Rev. B.* 42 (1990) 9365–9376. <https://doi.org/10.1103/PhysRevB.42.9365>.
- [127] S.R. Kotla, A.M. Schaller, T. Rekiş, S. Ramakrishnan, J.-K. Bao, L. Noohinejad, S. van Smaalen, G. de Laitre, M. de Boissieu, Temperature-dependent structural studies of incommensurately modulated Rb<sub>2</sub>ZnCl<sub>4</sub>, *Acta Crystallogr. Sect. A Found. Adv.* 77 (2021) C450–C450. <https://doi.org/10.1107/s0108767321092369>.
- [128] P.M. De Wolff, T. Janssen, A. Janner, The superspace groups for incommensurate crystal structures with a one-dimensional modulation, *Acta Crystallogr. Sect. A.* 37 (1981) 625–636. <https://doi.org/10.1107/S0567739481001447>.
- [129] T. Janssen, A. Janner, A. Looijenga-Vos, P.M. de Wolff, Incommensurate and commensurate modulated structures, in: *Int. Tables Crystallogr.*, 2006: pp. 907–955. <https://doi.org/10.1107/97809553602060000624>.

# List of author's works related to the doctoral thesis

Presented list contains author's works related to the doctoral thesis published in the indexed journals during the years of his doctoral studies. List is sorted by the year of publication in descending order.

- [i] P. Veřtát, H. Seiner, L. Straka, M. Klicpera, A. Sozinov, O. Fabelo, O. Heczko, Hysteretic structural changes within five-layered modulated 10M martensite of Ni-Mn-Ga(-Fe), *J. Phys. Condens. Matter.* 33 (2021) 265404. <https://doi.org/10.1088/1361-648x/abfb8f>. [FNSPE affiliation] [IF 2.3] [7 citations]
- [ii] V. Kopecký, M. Rameš, P. Veřtát, R.H. Colman, O. Heczko, Full Variation of Site Substitution in Ni-Mn-Ga by Ferromagnetic Transition Metals, *Metals (Basel)*. 11 (2021) 850. <https://doi.org/10.3390/met11060850>. [FNSPE affiliation] [IF 2.4] [9 citations]
- [iii] D. Musiienko, F. Nilsén, A. Armstrong, M. Rameš, P. Veřtát, R.H. Colman, J. Čapek, P. Müllner, O. Heczko, L. Straka, Effect of crystal quality on twinning stress in Ni-Mn-Ga magnetic shape memory alloys, *J. Mater. Res. Technol.* 14 (2021) 1934–1944. <https://doi.org/10.1016/j.jmrt.2021.07.081>. [IF 5.0] [10 citations]
- [iv] P. Veřtát, L. Straka, H. Seiner, A. Sozinov, M. Klicpera, O. Fabelo, O. Heczko, Hysteretic structural changes within five-layered modulated 10M martensites of Ni-Mn-Ga(-Fe), *Acta Crystallogr. Sect. A Found. Adv.* 77 (2021) C399–C399. <https://doi.org/10.1107/S0108767321092874>. (conference abstract) [FNSPE affiliation] [IF 2.3] [0 citations]
- [v] O. Heczko, P. Veřtát, M. Klicpera, O. Fabelo, L. Straka, Intermartensitic transformation between modulated structures in Heusler Ni-Mn-Ga(-Fe) single crystals, *Acta Crystallogr. Sect. A Found. Adv.* 77 (2021) C274–C274. <https://doi.org/10.1107/s0108767321094083>. (conference abstract) [FNSPE affiliation] [IF 2.3] [0 citations]
- [vi] M. Zelený, P. Sedlák, O. Heczko, H. Seiner, P. Veřtát, M. Obata, T. Kotani, T. Oda, L. Straka, Effect of electron localization in theoretical design of Ni-Mn-Ga based magnetic shape memory alloys, *Mater. Des.* 209 (2021). <https://doi.org/10.1016/j.matdes.2021.109917>. [IF 9.4] [5 citations]
- [vii] A. Sozinov, D. Musiienko, A. Saren, P. Veřtát, L. Straka, O. Heczko, M. Zelený, R. Chulist, K. Ullakko, Highly mobile twin boundaries in seven-layer modulated Ni-Mn-Ga-Fe martensite, *Scr. Mater.* 178 (2020) 62–66. <https://doi.org/10.1016/j.scriptamat.2019.10.042>. [IF 5.6] [12 citations]
- [viii] A. Armstrong, F. Nilsén, M. Rameš, R.H. Colman, P. Veřtát, T. Kmječ, L. Straka, P. Müllner, O. Heczko, Systematic Trends of Transformation Temperatures and Crystal Structure of Ni-Mn-Ga-Fe-Cu Alloys, *Shape Mem. Superelasticity.* 6 (2020) 97–106. <https://doi.org/10.1007/s40830-020-00273-3>. [7 citations]
- [ix] P. Veřtát, L. Straka, J. Drahokoupil, O. Heczko, Study of 10M' nanotwinned phase in the vicinity of martensitic transformation in Ni-Mn-Ga magnetic shape memory alloy, *Acta Phys. Pol. A.* 134 (2018) 859–862. <https://doi.org/10.12693/APhysPolA.134.859>. [FNSPE affiliation] [IF 0.6] [2 citations]
- [x] L. Straka, J. Drahokoupil, P. Veřtát, M. Zelený, J. Kopeček, A. Sozinov, O. Heczko, Low temperature a/b nanotwins in Ni<sub>50</sub>Mn<sub>25+x</sub>Ga<sub>25-x</sub> Heusler alloys, *Sci. Rep.* 8 (2018) 11943. <https://doi.org/10.1038/s41598-018-30388-8>. [IF 5.0] [9 citations]
- [xi] P. Veřtát, J. Drahokoupil, Fitexc – Diffraction Profile Fitting Program Run in MS Excel, *Acta Polytech. CTU Proc.* 17 (2018) 20. <https://doi.org/10.14311/app.2018.17.0020>. [FNSPE affiliation] [1 citation]
- [xii] L. Straka, J. Drahokoupil, P. Veřtát, J. Kopeček, M. Zelený, H. Seiner, O. Heczko, Orthorhombic intermediate phase originating from {110} nanotwinning in Ni<sub>50.0</sub>Mn<sub>28.7</sub>Ga<sub>21.3</sub> modulated martensite, *Acta Mater.* 132 (2017) 335–344. <https://doi.org/10.1016/j.actamat.2017.04.048>. [IF 9.2] [13 citations]

## List of author's works unrelated to the thesis

Presented list contains remaining author's publications in indexed journals, including those related to the topic of the doctoral thesis but published earlier and publications unrelated to the doctoral thesis. List is sorted by the year of publication in descending order.

- [i] M.M. Solovan, A.I. Mostovyi, H.P. Parkhomenko, M. Kaikanov, N. Schopp, E.A. Asare, T. Kovaliuk, P. Veřtát, K.S. Ulyanytsky, D. V. Korbutyak, V. V. Brus, A High-Detectivity, Fast-Response, and Radiation-Resistant TiN/CdZnTe Heterojunction Photodiode, *Adv. Opt. Mater.* (2022) 2202028. <https://doi.org/10.1002/adom.202202028>. [IF 10.0] [0 citations]
- [ii] Y. Ge, M. Vronka, P. Veřtát, M. Karlik, S.P. Hannula, O. Heczko, Deformation twinning with different twin-boundary mobility in 2H martensite in Cu–Ni–Al shape memory alloy, *Acta Mater.* 226 (2022). <https://doi.org/10.1016/j.actamat.2021.117598>. [IF 9.2] [1 citations]
- [iii] J. Pinc, M. Španko, L. Lacina, J. Kubásek, P. Ashcheulov, P. Veřtát, A. Školáková, O. Kvítek, D. Vojtěch, J. Čapek, Influence of the pre-exposure of a Zn-0.8Mg-0.2Sr absorbable alloy in bovine serum albumin containing media on its surface changes and their impact on the cytocompatibility of the material, *Mater. Today Commun.* 28 (2021) 102556. <https://doi.org/10.1016/j.mtcomm.2021.102556>. [IF 3.4] [2 citations]
- [iv] J. Pinc, A. Školáková, P. Veřtát, J. Duchoň, J. Kubásek, P. Lejček, D. Vojtěch, J. Čapek, Microstructure evolution and mechanical performance of ternary Zn-0.8Mg-0.2Sr (wt. %) alloy processed by equal-channel angular pressing, *Mater. Sci. Eng. A.* 824 (2021). <https://doi.org/10.1016/j.msea.2021.141809>. [IF 6.0] [4 citations]
- [v] K. Hosová, J. Pinc, A. Školáková, V. Bartůněk, P. Veřtát, T. Školáková, F. Průša, D. Vojtěch, J. Čapek, Influence of ceramic particles character on resulted properties of zinc-hydroxyapatite/monetite composites, *Metals (Basel)*. 11 (2021) 1–16. <https://doi.org/10.3390/met11030499>. [IF 2.4] [3 citations]
- [vi] M. Lebeda, P. Vlčák, P. Veřtát, J. Drahokoupil, Ab-initio study of surface energies and structural influence of vacancies in titanium nitride nanolayer, *NANOCON Conf. Proc. - Int. Conf. Nanomater.* 2021-October (2021) 214–220. <https://doi.org/10.37904/nanocon.2020.3706>. [0 citations]
- [vii] J. Čapek, J. Pinc, Š. Msallamová, E. Jablonská, P. Veřtát, J. Kubásek, D. Vojtěch, Thermal Plasma Spraying as a New Approach for Preparation of Zinc Biodegradable Scaffolds: A Complex Material Characterization, *J. Therm. Spray Technol.* 28 (2019) 826–841. <https://doi.org/10.1007/s11666-019-00849-1>. [IF 2.9] [8 citations]
- [viii] J. Pinc, J. Čapek, J. Kubásek, P. Veřtát, K. Hosová, Microstructure and mechanical properties of the potentially biodegradable ternary system Zn-Mg0.8-Ca0.2, *Procedia Struct. Integr.* 23 (2019) 21–26. <https://doi.org/10.1016/j.prostr.2020.01.057>. [5 citations]
- [ix] O. Heczko, M. Vronka, P. Veřtát, M. Rameš, K. Onderková, V. Kopecký, P. Krátká, Y. Ge, Mechanical Stabilization of Martensite in Cu–Ni–Al Single Crystal and Unconventional Way to Detect It, *Shape Mem. Superelasticity.* 4 (2018) 77–84. <https://doi.org/10.1007/s40830-018-0164-1>. [3 citations]
- [x] P. Vlčák, J. Drahokoupil, P. Veřtát, J. Šepitka, J. Duchoň, Hardness response to the stability of a Ti(+N) solid solution in an annealed TiN/Ti(+N)/Ti mixture layer formed by nitrogen ion implantation into titanium, *J. Alloys Compd.* 746 (2018) 490–495. <https://doi.org/10.1016/j.jallcom.2018.02.301>. [IF 6.4] [14 citations]
- [xi] P. Veřtát, J. Drahokoupil, P. Vlčák, Surface Characterization of Titanium Alloys for Nitrogen Ion Implantation, *Acta Polytech. CTU Proc.* 9 (2017) 39. <https://doi.org/10.14311/app.2017.9.0039>. [0 citations]
- [xii] P. Veřtát, J. Drahokoupil, O. Perevertov, O. Heczko, Phase transition in a multiferroic Ni-Mn-Ga single crystal, *Phase Transitions.* 89 (2016) 752–760. <https://doi.org/10.1080/01411594.2016.1199803>. [IF 1.5] [2 citations]

[xiii] O. Heczko, P. Veřtát, M. Vronka, V. Kopecký, O. Perevertov, Ni–Mn–Ga Single Crystal Exhibiting Multiple Magnetic Shape Memory Effects, *Shape Mem. Superelasticity*. 2 (2016) 272–280. <https://doi.org/10.1007/s40830-016-0077-9>. [10 citations]